

Wright State University

CORE Scholar

[Browse all Theses and Dissertations](#)

[Theses and Dissertations](#)

2018

Design of a Novel Tissue Culture System to Subject Aortic Tissue to Multidirectional Bicuspid Aortic Valve Wall Shear Stress

Janet Liu

Wright State University

Follow this and additional works at: https://corescholar.libraries.wright.edu/etd_all



Part of the [Mechanical Engineering Commons](#)

Repository Citation

Liu, Janet, "Design of a Novel Tissue Culture System to Subject Aortic Tissue to Multidirectional Bicuspid Aortic Valve Wall Shear Stress" (2018). *Browse all Theses and Dissertations*. 1941.
https://corescholar.libraries.wright.edu/etd_all/1941

This Thesis is brought to you for free and open access by the Theses and Dissertations at CORE Scholar. It has been accepted for inclusion in Browse all Theses and Dissertations by an authorized administrator of CORE Scholar. For more information, please contact library-corescholar@wright.edu.

DESIGN OF A NOVEL TISSUE CULTURE SYSTEM TO SUBJECT AORTIC TISSUE TO MULTIDIRECTIONAL BICUSPID AORTIC VALVE WALL SHEAR STRESS

A Thesis Submitted in Partial Fulfillment
of the Requirements for the Degree of
Master of Science in Mechanical Engineering

By

JANET LIU
B.S., Wright State University, 2014

2018
Wright State University

COPYRIGHT BY

JANET LIU

2018

WRIGHT STATE UNIVERSITY
GRADUATE SCHOOL

April 20, 2018

I HEREBY RECOMMEND THAT THE THESIS PREPARED UNDER MY
SUPERVISION Janet Liu ENTITLED Design of a Novel Tissue Culture System to Subject
Aortic Tissue to Multidirectional Bicuspid Aortic Valve Wall Shear Stress BE
ACCEPTED IN PARTIAL FULLFILLMENT OF THE REQUIRMENT FOR DEGREE
OF Master of Science of Mechanical Engineering.

Philippe Sucosky, Ph.D., F.A.H.A.
Thesis Director

Joseph C. Slater, Ph.D., P.E.
Chair, Department of Mechanical and
Materials Engineering

Committee on final examination:

Jaime E. Ramirez-Vick, Ph.D.

Zifeng Yang, Ph.D.

Barry Milligan, Ph.D.
Interim Dean of the Graduate School

ABSTRACT

Liu, Janet. M.S.M.E., Department of Mechanical & Materials Engineering, Wright State University. 2018. Design of a Novel Tissue Culture System to Subject Aortic Tissue to Multidirectional Bicuspid Aortic Valve Wall Shear Stress

Blood vessels experience complex hemodynamics marked by three-dimensionality and pulsatility. Arterial endothelial cells interact with the characteristics of the fluid wall shear stress (WSS) to maintain homeostasis or promote disease states. In particular, the bicuspid aortic valve (BAV), a congenital heart valve anatomy consisting of two leaflets instead of three, is associated with aortic complications presumably promoted by hemodynamic abnormalities. While devices have been used to test this hypothesis, their capabilities are limited to the generation of time-varying WSS magnitude in one direction. However, the increased flow helicity generated by BAVs in the aorta is expected to result in increased WSS multidirectionality. Therefore, the objectives of this thesis were to characterize the magnitude and directionality of the regional WSS in a BAV aorta, and to design a bioreactor capable of replicating these characteristics in vitro. This device will provide new insights into the mechanobiology of BAV aortopathy and other flow-mediated cardiovascular diseases.

NOMENCLATURE

Symbols

h_0	Height of the gap between the cone and plate
$h(r)$	Height between the cone and plate as moving toward the bioreactor wall
$\hat{\mathbf{k}}$	Longitudinal unit vector
$\hat{\mathbf{n}}$	Normal unit vector of the target surface
r	Distance from the center of the cone to the center of tissue
R	Distance from the center of the cone to the bioreactor wall
R_c	Radius of the cone
Re	Reynolds number, $\frac{R_c^2 \alpha^2 \omega_c}{12\nu}$
T	Time period
$T_{\text{angled face}}$	Torque on the angled side of the cone
T_{cone}	Cone acceleration torque
$T_{\text{cone side}}$	Torque on the cone side
$T_{\text{Tissue mount}}$	Torque on the tissue mount
α	Cone angle
β	Angular deviation of the computed wall shear stress vector on the tissue from the ideal flow (tangential) direction

$\hat{\theta}$	Circumferential unit vector
μ	Dynamic viscosity
ν	Kinematic viscosity
ρ	Working fluid density
$\underline{\tau}$	Instantaneous wall shear stress vector
τ_{circ}	Circumferential component of wall shear stress
τ_{long}	Longitudinal component of wall shear stress
τ_{total}	Total wall shear stress
φ	Angle between the longitudinal unit vector and the instantaneous wall shear stress vector
ω_c	Cone angular velocity
ω_{tissue}	Tissue angular velocity

Abbreviations

AA	Ascending aorta
AV	Aortic valve
BAV	Bicuspid aortic valve
CAD	Computer aided design
CFD	Computational fluid dynamics
CMR	Cardiac magnetic resonance
COSI	Circumferential oscillatory index
ECM	Extracellular matrix

FSI	Fluid-structure interaction
LOSI	Longitudinal oscillatory index
LR	Left-right coronary leaflet fusion
NL	Non-left coronary leaflet fusion
NRMSD	Normalized root-mean-squared deviation
MMPs	Matrix metalloproteinases
OSI	Oscillatory shear index
PC-MRI	Phase-contrast magnetic resonance imaging
PIV	Particle image velocimetry
RN	Right-non coronary leaflet fusion
RMST	Root mean squared total
TAV	Tricuspid aortic valve
TGF- β	Transforming growth factor-beta
TIMPs	Tissue inhibitor of metalloproteinases
transWSS	Transverse wall shear stress
TSM	Temporal shear magnitude
VSMC	Vascular smooth muscle cell
WSS	Wall shear stress

CONTENTS

FIGURES	xi
TABLES	xv
ACKNOWLEDGEMENT	xvi
CHAPTER 1: INTRODUCTION	1
1.1 The Aorta	1
1.2 The Normal Aortic Valve	3
1.3 The Bicuspid Aortic Valve	4
1.4 BAV Aortopathy	5
1.4.1 Ascending Aortic Dilation	6
1.4.2 Aortic Dilation Pathobiology	7
1.5 Aortic Dilation Diagnosis and Treatment	9
1.6 BAV Hemodynamics	10
1.6.1 <i>In Vivo</i> Studies	10
1.6.2 <i>In Vitro</i> Studies	12
1.6.3 Computational Studies	13
1.7 Etiologies of BAV Aortopathy	15
1.7.1 Genetic and Hemodynamic Etiologies.....	15
1.7.2 Supporting Evidence of the BAV Hemodynamic Theory	16
CHAPTER 2: SPECIFIC AIMS	18
Specific Aim 1: To quantify the multidirectional characteristics of BAV aorta WSS in regions prone to dilation	20
Specific Aim 2: To design a cone-and-plate bioreactor replicating the temporal changes in WSS magnitude and directionality of BAV aortic tissue	20
Specific Aim 3: To determine the bioreactor operating conditions	21
CHAPTER 3: SPECIFIC AIM 1	22
3.1 Rationale	22
3.2 Methods	22

3.2.1	TAV/BAV Aorta Fluid-Structure Interaction (FSI) Models.....	22
3.2.2	Longitudinal and Circumferential WSS Extraction	24
3.2.3	WSS Characterization.....	25
3.2.4	WSS Angular Variations.....	27
3.3	Results.....	28
3.3.1	WSS Orientation and Angular Variations.....	28
3.3.2	WSS Magnitude Characteristics	32
3.3.3	WSS Directionality Characteristics	36
CHAPTER 4: SPECIFIC AIM 2		41
4.1	Rationale	41
4.2	Design Principle.....	42
4.2.1	Components Description.....	42
4.2.2	Fluid Mechanics of the Cone-and-Plate Device.....	43
4.3	Design Solution.....	45
4.3.1	Overview	45
4.3.2	Cone Assembly	47
4.3.3	Tissue Mount Assembly.....	49
4.3.4	Bioreactor Case Assembly	51
4.3.5	Perfusion System	52
4.3.6	Driving System	53
4.4	Summary	54
CHAPTER 5: SPECIFIC AIM 3		55
5.1	Rationale	55
5.2	Methods	55
5.2.1	Computational Fluid Dynamics (CFD) Models.....	56
5.2.2	Determination of the Operating Conditions.....	62
5.2.3	Torque Calculations for Motor Selections	69
5.3	Results.....	70
5.3.1	Mesh Dependency Test.....	70
5.3.2	Finalized Dimensions.....	72
5.3.3	Optimized WSS Waveform	74
CHAPTER 6: SUMMARY.....		78
CHAPTER 7: DISCUSSION.....		79
7.1	Novelty of the Study	79
7.2	WSS Characteristics in TAV/ BAVs Proximal AA.....	80

7.3	WSS Angular Deviation from the Circumferential Direction Computed on Tissue.....	83
7.4	Limitations of the Study.....	83
7.5	Clinical Implication	84
7.6	Future Work	84
APPENDIX A: Time-varying WSS Vector in the Convexity of Proximal AA for All Valve-aorta Models.....		86
APPENDIX B: CAD Drawings of Each Bioreactor Part		88
REFERENCES.....		99

FIGURES

Figure 1. Different sections of the aorta: 1.) ascending aorta; 2.) aortic arch; 3.) thoracic aorta; 4.) abdominal aorta	2
Figure 2. Cross-sectional view of the aortic wall. The aortic wall consists of three layers: 1.) tunica intima; 2.) tunica media; 3.) tunica adventitia	2
Figure 3. Heart anatomy	3
Figure 4. Heart valve function: the aortic valve closes during diastole and opens during systole	4
Figure 5. Short-axis view of the tricuspid aortic valve (TAV)	4
Figure 6. BAVs exist in three types: A.) type-0 (no raphe), type-I (one raphe) and type-II (two raphes); Type-I BAVs are further categorized into three morphotypes: B.) LR-BAV, RN-BAV and NL-BAV	5
Figure 7. Aortic dilation patterns in A.) TAV; and B.) BAV aortas.....	6
Figure 8. BAV morphotypes and their corresponding aortic dilation phenotype. The circled numbers indicate the number of cases shift from one phenotype to the other found in follow-up examination.....	7
Figure 9. Reduction aortoplasty. A.) The enlarged, excessive aortic tissue in oval shape is excised from the convexity of the AA, and B.) the opening is sutured to close.....	9
Figure 10. Dacron Graft. A synthetic polyester tube which is used for replacing and repairing blood vessels.....	10

Figure 11. Comparisons of the flow patterns in A.) healthy volunteer; B.) aorta size control; C.) LR-BAV AA; D.) RN-BAV AA. The flow pattern in the healthy volunteer follows streamline. In contrast, the flow patterns are helical, and the jet impinged at the right-posterior aortic wall regions in the LR-BAV and RN-BAV, respectively.	12
Figure 12. Hemodynamic theory of BAV AA dilation.....	15
Figure 13. Valve-aorta FSI models. A.) TAV; B.) LR-BAV; C.) RN-BAV; D.) NL-BAV	24
Figure 14. WSS extraction A.) at the convexity and concavity; B.) in longitudinal and circumferential directions.	25
Figure 15. WSS magnitude vs. orientation in proximal convexity and concavity of A.) TAV, B.) LR-BAV, C.) RN-BAV and D.) NL-BAV aorta models	30
Figure 16. Angular distribution of normalized mean WSS magnitude at the proximal convexity of the A.) TAV; B.) LR-BAV; C.) RN-BAV and D.) NL-BAV aortas. The orange dash line represents the 50% threshold.	31
Figure 17. Summary of the number of sectors satisfying each criterion at the convexity of AA for all valve-aorta models.....	32
Figure 18. Total, longitudinal and circumferential TSM at the convexity and concavity of the proximal AA	36
Figure 19. Longitudinal and circumferential OSI at the convexity and concavity of the proximal AA	38
Figure 20. Ratio of transWSS and total TSM in the convexity and concavity of the proximal AA for all models.	40
Figure 21. Cone-and-plate bioreactor.	42

Figure 22. Culture system schematic	45
Figure 23. Assembly components. A.) Cone assembly; B.) Tissue mount assembly; C.) Bioreactor case assembly	46
Figure 24. Cone assembly in cross-sectional view. Showing A.) components and their corresponding locations; B.) cone in closer view	47
Figure 25. Tissue mount in A.) Overview; B.) Cross-sectional view; C.) Top view	50
Figure 26. Tissue mount assembly in cross-sectional view	50
Figure 27. Bioreactor case assembly in A.) overview; B.) cross-sectional view.....	52
Figure 28. Bioreactor schematic ($h = 200 \mu\text{m}$ and $\alpha = 0.5^\circ$).....	57
Figure 29. Boundary condition at each section.....	59
Figure 30. Comparison between the target WSS and the computed WSS output in magnitude. The computed WSS deviates from the target at the peak.	62
Figure 31. Operating condition strategy flowchart. Blue lines represent the general process, red lines represent the waveform optimization process for WSS magnitude and yellow lines represent WSS angular variation correcting process.....	64
Figure 32. Comparison between the initial WSS magnitude input and the scaled WSS magnitude input	65
Figure 33. Definition of the tangential direction, angular deviation and computed WSS vector.....	66
Figure 34. Error in WSS angle at each time point over the entire cardiac cycle.	67
Figure 35. Comparison between the target and computed WSS angular variations.....	67
Figure 36. Comparison of WSS angular deviations between two cases: 1.) with tissue rotation and 2.) without tissue rotation.	68

Figure 37. Percent differences between current and successive mesh setup in WSS magnitude on the tissue surface for each model.	71
Figure 38. Percent differences between current and successive mesh setup in torque on the tissue for each model.....	71
Figure 39. Comparisons between target, the initial and the optimized (post-correction) WSS magnitude	75
Figure 40. Comparisons between target, initial, scaled and optimized (post-correction) WSS angle waveform	75

TABLES

Table 1. Angle distribution in the convexity of the AA of all models.....	31
Table 2. Width of WSS angle range for WSS magnitudes exceeding 50% of the maximum WSS at the proximal convexity for all models	31
Table 3. Total TSM (Pa) at convexity and concavity of all valve-aorta models	33
Table 4. Longitudinal TSM (Pa) at convexity and concavity of all valve-aorta models ..	34
Table 5. Circumferential TSM (Pa) at convexity and concavity of all valve-aorta models	35
Table 6. Longitudinal OSI at convexity and concavity of all valve-aorta models	38
Table 7. Circumferential OSI at convexity and concavity of all valve-aorta models.....	38
Table 8. transWSS and transWSS/total TSM ratio in the convexity and concavity of all valve-aorta models.	39
Table 9. Model numbers with their corresponding descriptions and dimensions.....	58
Table 10. The calculated cone angular velocity for each model for mesh dependency test	60
Table 11. The calculated NRMSD and R^2 values in WSS angular deviations when simulation performed 1.) with tissue rotation and 2.) without tissue rotation	69
Table 12. Mesh properties (n=6) for each bioreactor models	72
Table 13. The calculated NRMSD and R^2 values in WSS magnitude for each model....	73
Table 14. The calculated NRMSD and R^2 values in WSS angular variations for each model.....	74
Table 15. Motor specifications requirement for cone and tissue mount rotations.....	76

ACKNOWLEDGEMENT

I would like to express my sincere appreciation to my advisor Dr. Philippe Sucusky for his tremendous support, guidance and patience throughout my graduate study. I would also like to thank my colleagues: Samantha Atkins, Johana Barrientos, Ashish Madan and Jason Shar, who had always been super supportive and provided help, advice and joy throughout my graduate journey. My thanks also go to Kurtis Cornelius, Mathew Graham, Tremayne Leonard and Abram Yorde from the Fall 2017 senior design team, who assisted me with bioreactor design. Last, but not the least, I would like to thank my family for always providing me with spiritual supports.

CHAPTER 1:

INTRODUCTION

1.1 The Aorta

The aorta, the largest artery in the body, originates from the left ventricle of the heart. Its main function is to transport oxygenated blood to the body. Oxygenated blood comes from the pulmonary vein, enters the heart via the left atrium and then fills the left ventricle prior to ejection. When the heart contracts, the blood is ejected through the aortic valve to the aorta and the systemic circulation. The aorta can be divided into four sections: the ascending aorta, the aortic arch, the thoracic aorta and the abdominal aorta (Figure 1 [1]). While factors such as gender, age and body size affect the size of ascending aorta, the average diameter of a normal human ascending aorta is 33 mm (31.4 mm in females, 37.4 mm in males [2])

The aortic wall is composed of three layers (Figure 2). Each layer serves different functions and has different characteristics. The inner layer is the tunica intima and is the interface between blood flow and the aortic wall. It continuously experiences the viscous fluid shear stress exerted by the blood flow. It consists of a thin layer made up of endothelial cells, subendothelial connective tissue and an internal elastic lamina. The middle layer is the tunica media, which is responsible for the contractile ability of the artery. It consists of multiple layers of smooth muscle cells embedded in their

extracellular matrix (ECM). Finally, the outer layer is the tunica adventitia, which consists of connective tissue and nerves.

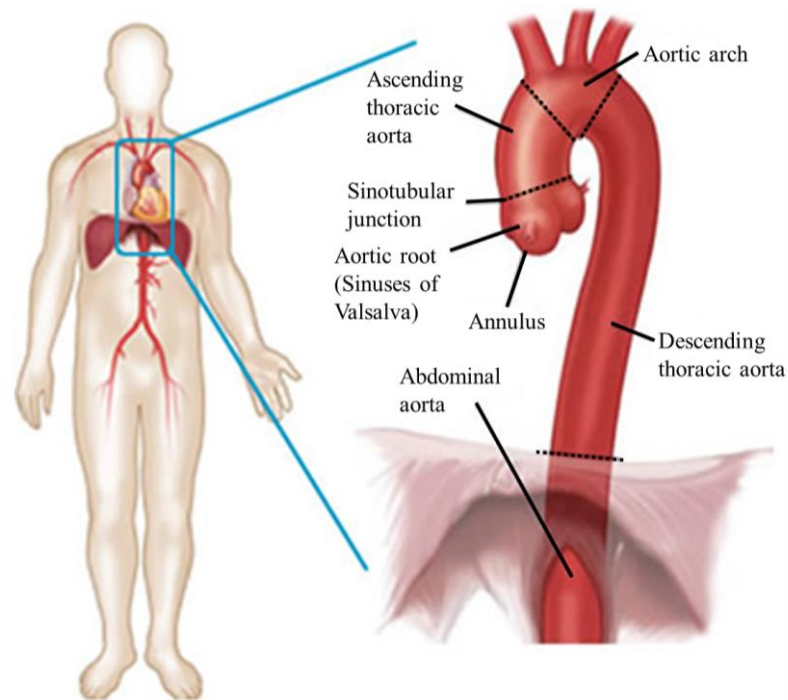


Figure 1. Different sections of the aorta: 1.) ascending aorta; 2.) aortic arch; 3.) thoracic aorta; 4.) abdominal aorta

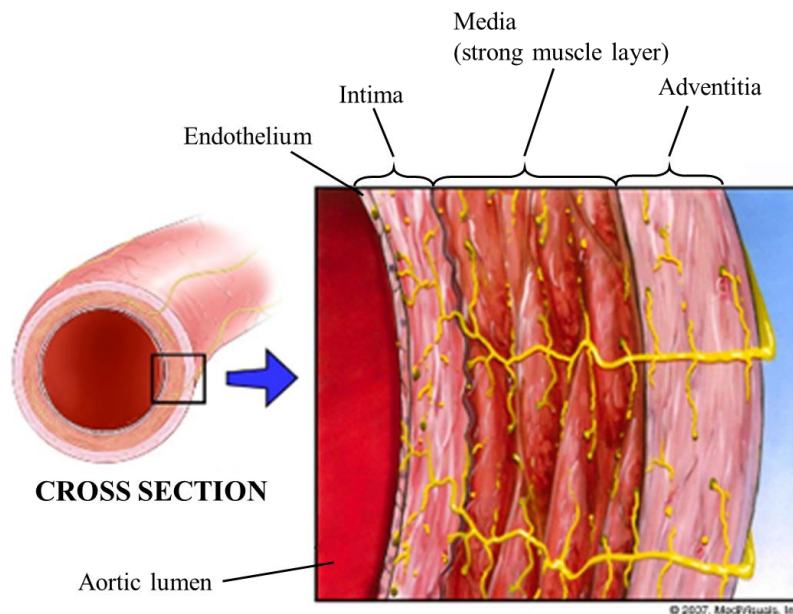


Figure 2. Cross-sectional view of the aortic wall. The aortic wall consists of three layers: 1.) tunica intima; 2.) tunica media; 3.) tunica adventitia

1.2 The Normal Aortic Valve

The human heart contains four valves for achieving unidirectional blood flow. The aortic valve (AV) is located between the left ventricle and the aorta (Figure 3). The main function of the AV is to achieve unidirectional blood flow from the left ventricle to the aorta during systole and to prevent backflow during diastole (Figure 4). The AV is also known as aortic semilunar valve or tricuspid aortic valve (TAV) since the normal AV consists of three pocket-like semilunar cusps. The cusps, also known as leaflets, are referred to as the left-coronary, the right-coronary and the non-coronary leaflets, according to their respective position relative to the coronary arteries (Figure 5).

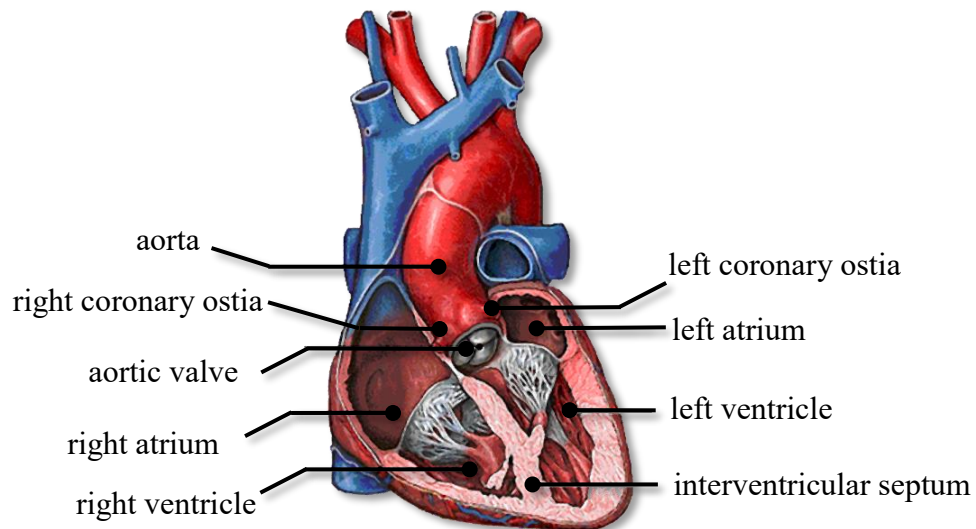


Figure 3. Heart anatomy

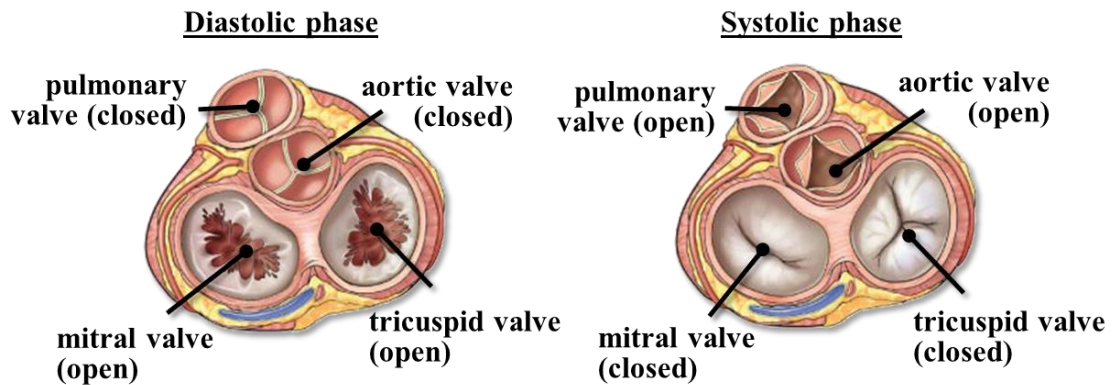


Figure 4. Heart valve function: the aortic valve closes during diastole and opens during systole

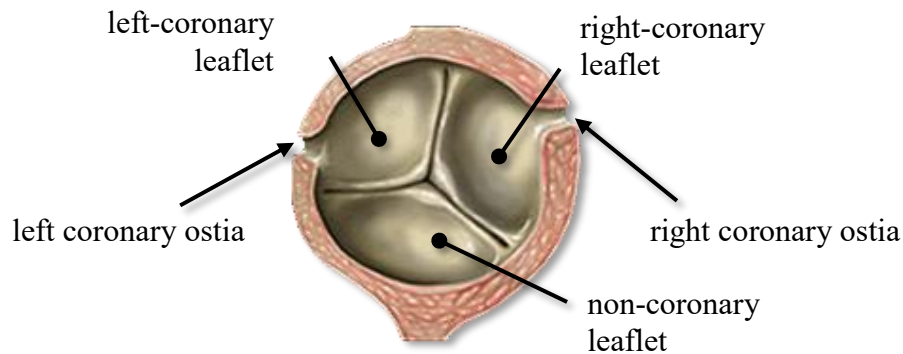


Figure 5. Short-axis view of the tricuspid aortic valve (TAV)

1.3 The Bicuspid Aortic Valve

The bicuspid aortic valve (BAV) is one of the most common congenital heart defect in which two aortic valve leaflets remain fused during embryonic development. This defect exists in 1-2% of the general population [3], [4]. Depending on the number of fusion sites (raphe) present between the leaflets, BAVs are categorized into three types. Type-0, type-I and type-II BAVs characterize BAVs with no raphe, one raphe and two

raphes, respectively (Figure 6-A). The type-I BAV is the most common (88% of the BAV patients) [5] and can be further categorized into three morphotypes based on the position of the leaflet fusion: left- and right-coronary leaflet fusion (LR-BAV), right- and non-coronary leaflet fusion (RN-BAV), and non- and left-coronary leaflet fusion (NL-BAV). The LR-BAV is the most prevalent morphotype and accounts for 71% of type-I BAVs, while the RN- and NL-BAV occur in 15% and 3% of type-I BAV cases, respectively (Figure 6-B) [6]–[14].

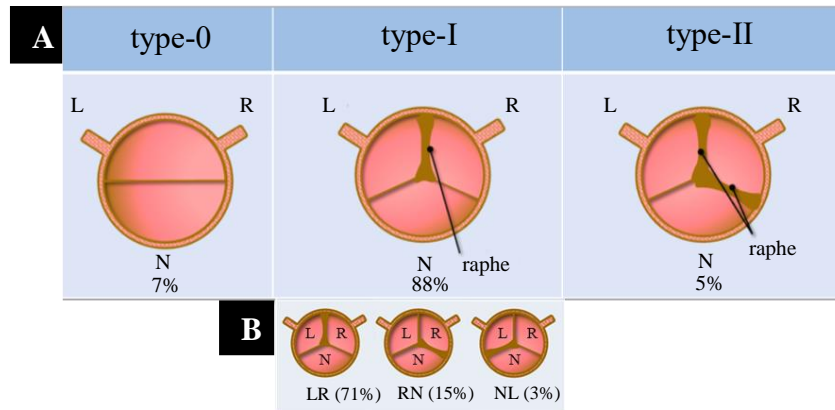


Figure 6. BAVs exist in three types: A.) type-0 (no raphe), type-I (one raphe) and type-II (two raphes); Type-I BAVs are further categorized into three morphotypes: B.) LR-BAV, RN-BAV and NL-BAV

1.4 BAV Aortopathy

Previous research suggests that BAV is associated with secondary aortopathy, such as aortic dilation [15], aortic aneurysm [16] and aortic dissection [17]. Aortic dilation, the precursor of aortic aneurysm, results from vascular smooth muscle cell (VSMC) apoptosis, elastic fiber degeneration and abnormal ECM remodeling [18].

1.4.1 Ascending Aortic Dilation

Aortic dilation is an abnormal enlargement of the aorta. Although both TAV and BAV patients can develop ascending aortic dilation, BAV patients are at higher risk of developing the disease [17], [19], [20] and the dilation patterns are quite different. When aortic dilation develops in the AA of TAV patients, it is usually symmetric. In contrast, asymmetric dilation patterns are usually observed in BAV AAs (Figure 7)[21]. The incidence of aortic dilation in TAV patients with hypertension and BAV patients is 12% and 35-68%, respectively [17], [19], [20]. Furthermore, BAV patients experience more rapid dilation progression rate (0.2-1.9 mm/yr) than TAV patients (0.07-0.2 mm/yr) [22].

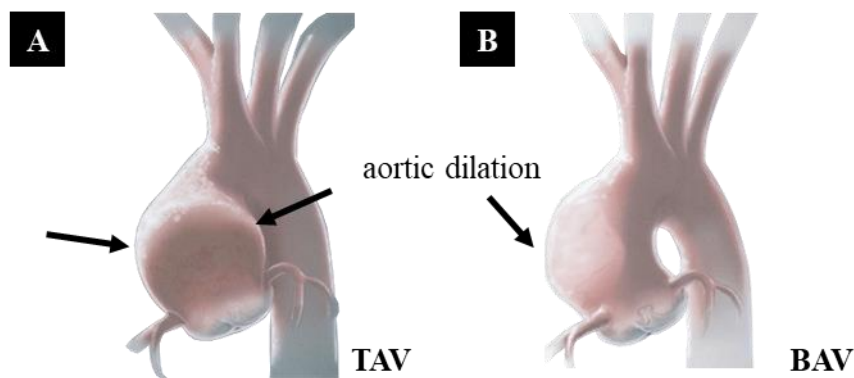


Figure 7. Aortic dilation patterns in A.) TAV; and B.) BAV aortas

AA dilation has been further categorized into three phenotypes based on the location of the dilation on the AA: aortic root (type-1), tubular portion of the AA (type-2), and the entire AA and the transverse aortic arch (type-3) [23]. Previous studies aimed at investigating the relationship between BAV morphotypes and dilation phenotypes through echocardiography and cardiac magnetic resonance (CMR) have indicated that LR-BAV patients are prone to develop type-1 dilation (18 out of 92 LR-BAV patients) and that type-1 dilation is exclusively observed in LR-BAV patients. In contrast, RN-

BAV patients are more likely to develop type-2 and type-3 dilation (24 out of 41 RN-BAV patients) (Figure 8) [24], [25].

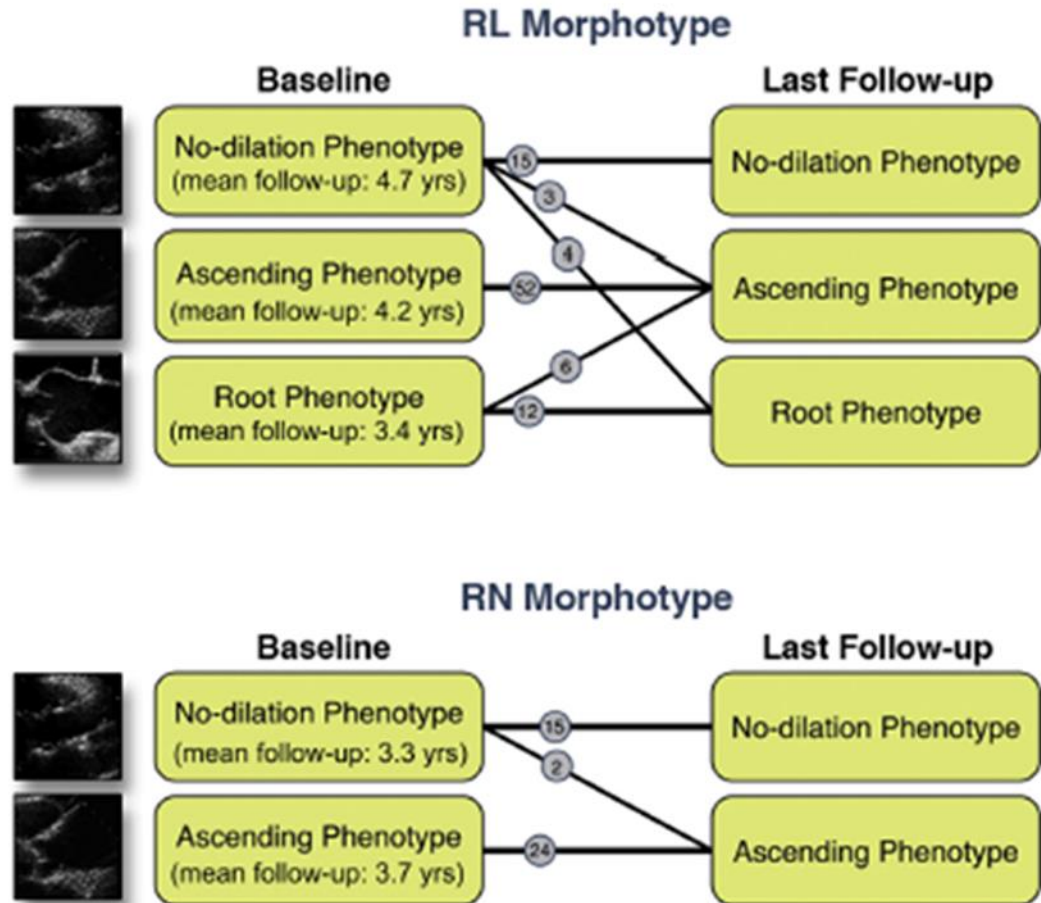


Figure 8. BAV morphotypes and their corresponding aortic dilation phenotype. The circled numbers indicate the number of cases shift from one phenotype to the other found in follow-up examination.

1.4.2 Aortic Dilation Pathobiology

VSMCs Apoptosis and Deficiency of Fibrillin-1

Previous biochemical studies have quantified the rate of VSMC apoptosis and the levels of fibrillin-1, collagen and elastin in the aortic media of both TAV and BAV patients. BAVs have been associated with a higher rate of VSMCs apoptosis than TAVs,

especially in the convexity of the aorta [26]. Furthermore, the levels of type-I/III collagen measured in the convexity of BAV aortas where the dilation is prone to occur are lower than in TAV aortas. Greater elastic fragmentation and less VSMCs have been observed in the convexity as compared with the concavity of BAV aortas [27].

VSMCs are the major components of the tunica media and play an important role in maintaining the structural integrity of the aorta. The two primary functions of the VSMCs are 1.) to regulate the contraction of the vessel when mechanical stimuli are sensed, and 2.) to synthesize ECM, which includes collagen, elastin, laminin, proteoglycan, fibrillin, fibronectin and tenascin [28], [29].

Fibrillin-1, a glycoprotein, is the main component responsible for the structural integrity of the aortic wall. Fibrillin-1 is required to bind VSMCs to the elastin/collagen matrix. VSMC apoptosis occurs when the media is deficient in fibrillin-1, which causes VSMCs to dissociate from the elastin/collagen matrix, resulting ultimately in a loss of vessel structural integrity [4], [30].

Elastic Fiber Degeneration and ECM Remodeling

Matrix metalloproteinases (MMPs) are a type of enzymes that digest matrix proteins and are synthesized by the cellular components of the vessel wall and inflammatory cells. Previous studies have suggested that BAV aortic dilation may be related to the high activity of MMPs, especially MMP-9. The release of MMP-9 can be activated either when the levels of tissue inhibitor of metalloproteinases (TIMPs) are decreased [31], [32] or when the transforming growth factor-beta (TGF- β) cascade is triggered [33]. On the other hand, MMP-9 are two of the downstream targets of the TGF-

β pathway. Once the TGF- β cascade is triggered, MMP-9 activity is increased, leading in turn to degradation of type IV collagen, elastin and fibrillar collagens, and causing ECM remodeling, which eventually leads to aortic dilation [4], [34].

1.5 Aortic Dilation Diagnosis and Treatment

The average diameter of a normal human AA is 33 mm. AA aneurysm is usually diagnosed either when the diameter of the dilated aorta is equal to or greater than 1.5 times the normal average diameter, or when the diameter exceeds 5 cm [35].

Depending on the severity of the aneurysm, surgery might be recommended. There are two methods to treat ascending aorta aneurysm. The first method is reduction aortoplasty, in which the dilated aorta is cut open, a section of the aortic wall is trimmed off and the aorta is closed by suturing [36] (Figure 9 [6]–[14]). The second method is the Dacron graft method and consists of replacing the dilated site of the aorta with a tube-shaped Dacron graft made of synthetic material (Figure 10).

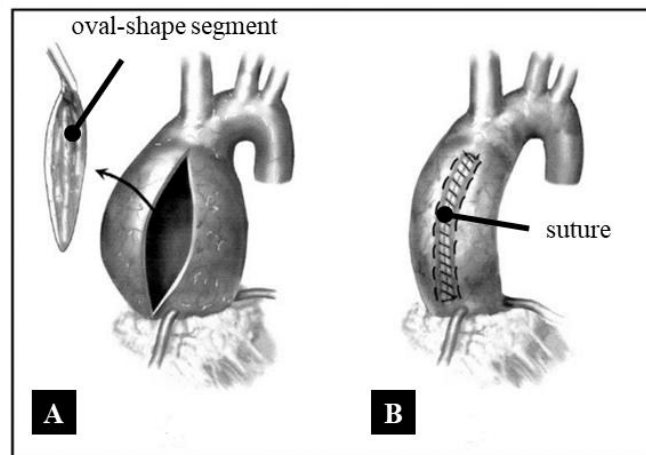


Figure 9. Reduction aortoplasty. A.) The enlarged, excessive aortic tissue in oval shape is excised from the convexity of the AA, and B.) the opening is sutured to close.

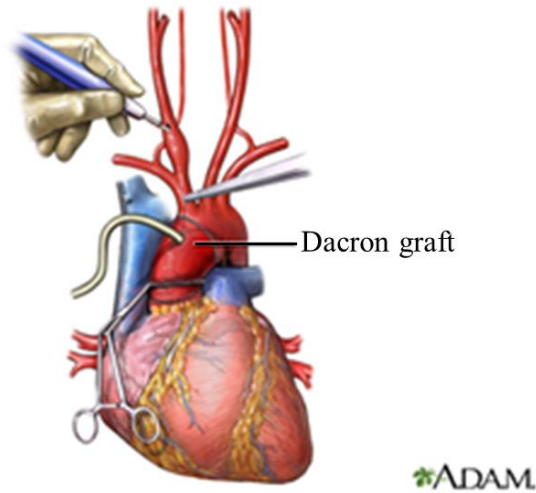


Figure 10. Dacron Graft. A synthetic polyester tube which is used for replacing and repairing blood vessels.

1.6 BAV Hemodynamics

Multiple studies have investigated the flow field in BAV AAs and its potential role in aortopathy through *in vivo* [13], [37]–[41], *in vitro* [8], [42], and computational [43], [44] techniques.

1.6.1 *In Vivo* Studies

Barker et al. performed clinical measurements using phase-contrast magnetic resonance imaging (PC-MRI) to compare the regional WSS in TAV and BAV aortas [13], [37]. The studies revealed that BAVs are associated with increased circumferential WSS, and that LR-BAVs result in flow impingement on the right-anterior AA. Retrograde, asymmetric flow patterns were also observed in BAV aortas.

Other studies conducted by Hope and colleagues aimed at investigating the flow patterns and WSS abnormalities in BAV AAs via 4D PC-MRI [40], [41]. The studies

reported that BAVs cause eccentric, helical flow patterns at peak systole in the AA, with asymmetrically elevated WSS. The results also evidenced that, although type-I BAVs cause helical flow in the AA, the flow patterns and the location of flow impingement on the AA wall are strongly dependent on the BAV morphotype. The LR-BAV generates right-handed helical flow in the AA and causes the flow to impinge on the right-anterior portion of the AA. In contrast, the RN-BAV generates left-handed helical flow and results in flow impingement at the left-posterior portion of the AA. Similar results were found in studies performed by Bissell et al. [39] and Mahadevia et al [38].

Bissell et al. attempted to identify the relationship between flow abnormalities and aortic dilation via CMR analysis over a large sample size (95 BAV patients and 47 healthy volunteers). The results demonstrated that BAVs are linked to abnormal, higher right-handed helical flow, higher systolic WSS and larger AAs as compared to the normal TAV. It was also demonstrated that the abnormal flow in BAV patients occurs before the development of aortic dilation, suggesting that the abnormal flow might induce aortopathy [11].

Using 4D MRI, Mahadevia et al. demonstrated that BAVs cause eccentric outflow jet patterns in the AA, which result in increased regional WSS. The locations of jet impingement were the right-anterior wall in LR-BAV patients and the right-posterior wall in RN-BAV patients (Figure 11)[38].

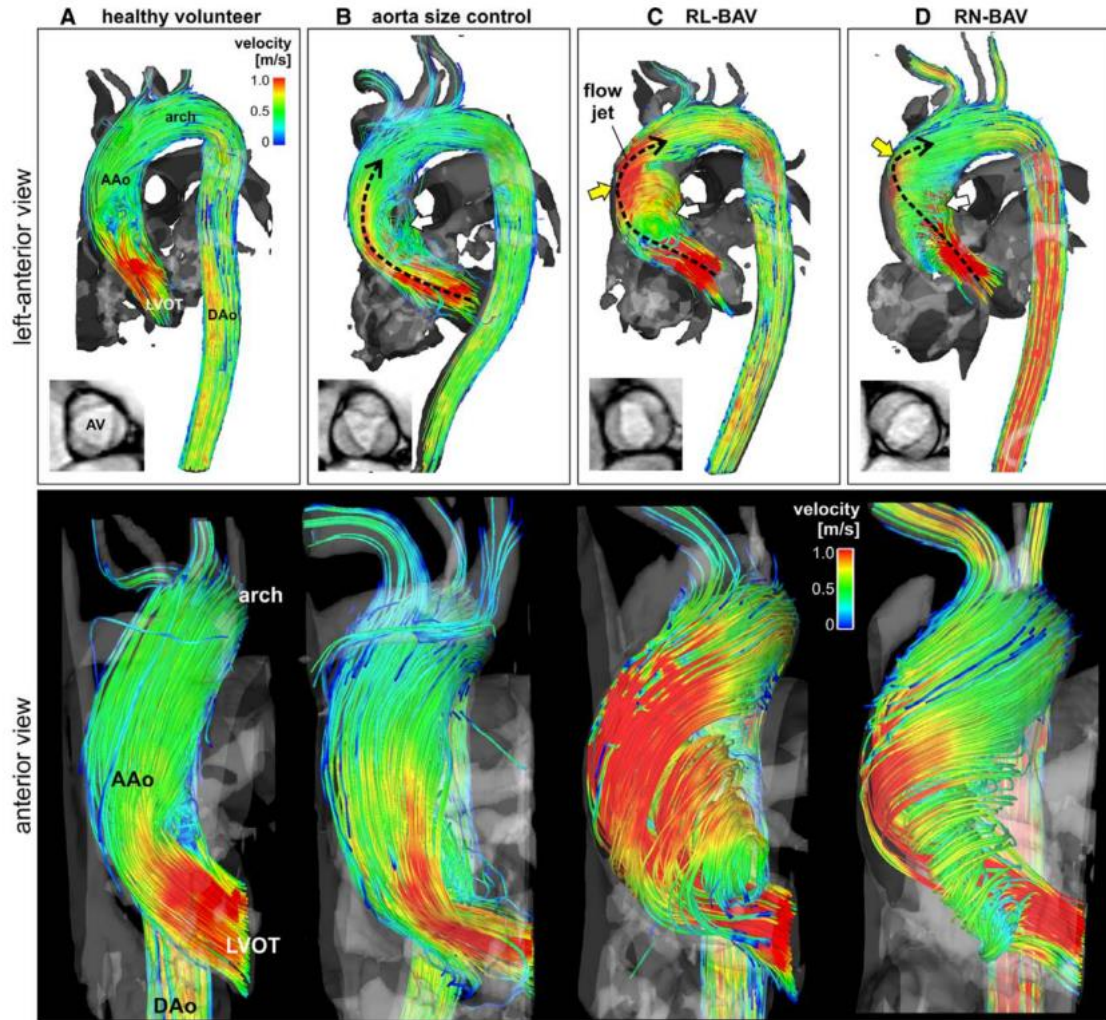


Figure 11. Comparisons of the flow patterns in A.) healthy volunteer; B.) aorta size control; C.) LR-BAV AA; D.) RN-BAV AA. The flow pattern in the healthy volunteer follows streamline. In contrast, the flow patterns are helical, and the jet impinged at the right-posterior aortic wall regions in the LR-BAV and RN-BAV, respectively.

1.6.2 *In Vitro* Studies

Particle image velocimetry (PIV) has been used to characterize quantitatively and qualitatively the flow field in TAVs and BAVs. By performing this in vitro analysis, Saikrishnan et al. attempted to measure and characterize the flow environment generated

by TAVs and LR-BAVs. They first aimed at studying the impact of jet eccentricity by varying the level of stenosis on the BAV [9]. Other factors, such as jet angle, jet velocity and aortic dilation, which may also exist in BAV patients, were taken into account in a follow-up study [45]. The results demonstrated that BAVs generate increased systolic jet velocity and flow impingement on the convexity of the AA wall, which results in a strong vortex in the non-fused leaflet sinus. Moreover, increase in the level of turbulence and WSS was also observed in BAVs relative to TAVs.

Other studies investigating the BAV flow characteristics through PIV experiments were conducted by Seaman et. al. [8] and McNally et al. [42]. Seaman et. al. aimed at quantifying the energy loss through the valve. The experiment was performed under steady peak-systolic flow with normal and calcified TAVs and LR-BAVs. The results revealed that BAVs are associated with higher energy loss relative to TAVs and result in an elliptical orifice, which causes the jet to skew toward the non-coronary leaflet [8].

McNally and colleagues aimed at distinguishing the flow characteristics caused by each type-I BAV morphotype (i.e., LR-BAV, RN-BAV and NL-BAV) under native pulsatile flow. Both LR-BAVs and NL-BAVs resulted in increased peak-systolic orifice jet velocity and WSS overloads on the AA convexity relative to TAVs [42].

1.6.3 Computational Studies

Computational fluid dynamics (CFD) and fluid-structure interaction (FSI) modeling have been widely used for the hemodynamics characterization of blood vessels at higher spatial and temporal resolutions than conventional imaging techniques such as Doppler echocardiography and PC-MRI [46]–[48].

Previous *in vivo* study has revealed that the degree of jet skewness is proportional to the AA diameter and the severity of aortic dilation [49]. Faggiano et al. aimed at linking these findings to BAV flow characteristics during systole through computational analysis [14]. CFD aorta models were constructed based on PC-MRI images of TAV and BAV patients with varying valve orifice area and degree of aortic dilation. The results demonstrated that the narrower orifice is, the more skewed the orifice jet would be. Asymmetric jet was only observed in BAV cases, and all of them were reported with high flow helicity and high systolic WSS magnitude in the AA.

Instead of studying flow characteristics in BAV aortas with pre-existing dilation, Cao and colleagues designed TAV and type-I BAV aorta FSI models to quantify the influence of the valve structure on the downstream hemodynamic environment in a normal non-dilated AA. The results demonstrated that type-I BAV morphotypes cause WSS overload on the AA convexity at peak systole, and WSS unidirectionality was higher in the convexity of the proximal AA in all BAVs. The fact that BAVs cause asymmetric helical flow and systolic WSS overload on the convexity of the AA was confirmed [43].

Kimura et al. performed a patient-specific CFD analysis aimed at analyzing the flow patterns and WSS distributions in TAV/BAV aortas [38]. The study revealed that although the flow patterns in BAV patients differed greatly, abnormal helical flow was present in the AA and transverse arch of all BAV patients. Furthermore, right-handed helical flow was present in 91% of BAV aortas. Elevated WSS on the convexity of BAV AAs and asymmetric flow in the BAV AAs were also detected. Notably, 3 out of the 4 LR-BAV patients and 1 out of the 2 RN-BAV patients exhibited flow impingement and

elevated WSS on the right anterior wall and right posterior wall, respectively [44]. This confirmed the flow characteristics reported by Mahadevia et al [18].

1.7 Etiologies of BAV Aortopathy

1.7.1 Genetic and Hemodynamic Etiologies

Two etiologies have been proposed to explain the link between BAV and aortopathy. One suggests that BAV secondary aortopathy is genetic, while the other suggests that it can also be due to abnormalities in the hemodynamic environment. The abnormal blood flow and WSS generated by BAVs could trigger critical biological processes (e.g., ECM remodeling, VSMC apoptosis, fibrillin-1 depletion [18], [21], [27]) leading ultimately to aortic dilation (Figure 12 [50]). Other studies have suggested the existence of correlations between those hemodynamic abnormalities, the asymmetric patterns of the aortic dilation on the convexity of the ascending aortic wall, and aortic medial degradation [51].

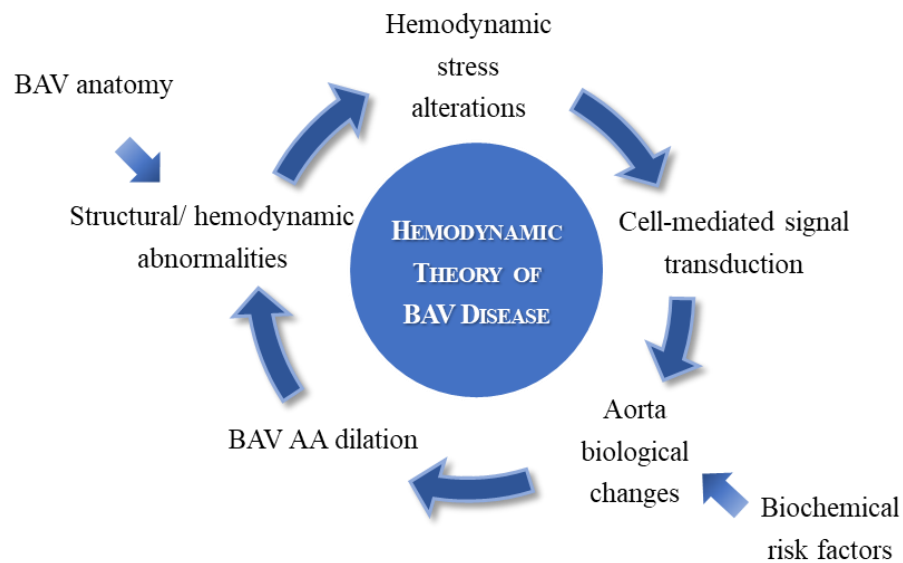


Figure 12. Hemodynamic theory of BAV AA dilation

1.7.2 Supporting Evidence of the BAV Hemodynamic Theory

As mentioned earlier, aortic dilation is a result of a series of biochemical processes involving VSMC apoptosis, elastic fiber degeneration and abnormal ECM remodeling [52]. These biological events are regulated by the expression and activity of certain proteins and enzymes (i.e., fibrillin-1, TGF- β , MMP-2, MMP-9, TIMPs, etc.). Biological analyses have been performed to investigate the levels/activities of these components in TAV and BAV aortas. Fedak et al. and Boyum et al. analyzed TAV and BAV aortic tissue samples using immunohistochemistry, fluorescence microscopy and gelatinase zymography. The results revealed that BAV aortas exhibit decreased levels of fibrillin-1 expression and increased MMP-2/9 activity relative to TAV aortas [53], [27].

To determine the role played by those proteins and enzymes in aortic dilation, Cotrufo et al. [54] and Della Corte et al. [13], [37]–[41] performed comparative biological analyses on the convexity and concavity of TAV and BAV aortas. Decreased levels of type-I and type-III collagens and increased level of type-IV collagen were observed in dilated BAV aortas relative to TAV aortas. Those changes were more significant in the convexity of BAV aortas than in the concavity. Also, increased VSMC apoptosis was detected in the convexity of BAV aortas. These studies concluded that BAV aortas exhibit asymmetric ECM expression and increased VSMC apoptosis in the AA convexity, which correlate with the asymmetric flow patterns evidenced by *in vivo* [8], [42], *in vitro* [43], [44], and computational studies [21].

To demonstrate that abnormal WSS exerted on the convexity of the AA triggers biological events and leads to aortic dilation, *ex vivo* biological experiments have been conducted to investigate the acute biological response of porcine aortic tissue subjected to

TAV and BAV WSS. These studies revealed increased MMP-2 and 9 levels following tissue conditioning to WSS from the convexity of the BAV AA [55]. In contrast, there was no significant difference in MMP-2 level when subjecting porcine aortic tissue to the WSS from the TAV/BAV AA concavity [56].

Collectively, these studies provide preliminary supporting evidence for the role played by hemodynamics in BAV aortic dilation.

CHAPTER 2:

SPECIFIC AIMS

The BAV is a congenital valvular defect resulting from the fusion between two leaflets [43]. While *in vivo*, *in vitro* and computational studies have evidenced that BAV can cause helical flow patterns and abnormal WSS in the AA [57], previous flow characterizations have focused on the quantification of the total or longitudinal WSS in terms of magnitude and pulsatility [57]–[59]. The demonstrated increased helicity of BAV flow is expected to generate a significant circumferential WSS component, whose characteristics to date remain largely unknown. In addition, aortic cells respond to hemodynamic stress abnormalities by activating critical biological processes, which may lead to aortopathy. The elucidation of the cause-and-effect relationships between BAV flow and aorta biology requires a device capable of subjecting native aortic tissue to its local hemodynamic stress environment.

Different fluid shear stress bioreactors, such as the parallel plate flow chamber, microfluidic devices and the cone-and-plate bioreactor, have been designed and used to expose tissue samples to desired fluid shear stress environment [58]. Although those bioreactors are capable of subjecting tissue samples to desired WSS magnitude, their ability to replicate the actual native hemodynamic environment faces some limitations. The native hemodynamic environment often involves time-dependent pulsatile WSS magnitude and directionality. The parallel flow chamber can only produce shear stress at

a constant magnitude. In fact, the fluid volume required to fill the bioreactor is typically large, creating challenges in generating a pulsatile WSS due to the high fluid inertia [59], [60].

Microfluidic devices have also been used to expose cells to desired WSS magnitude. Such devices usually consist of a pump and cell culture chambers filled with fluid. Pumps are used to push the fluid into/out of the chamber. The flow generated in the chamber is Poiseuille flow, which results in uniform shear stress distribution on the bottom surface of the chamber. However, such devices are usually designed with small dimensions (e.g., 24-100 μm in depth and 200 μm in width) since their purpose is to subject a cell monolayer to fluid shear stress [61], [62], limiting their application to the conditioning of tissue.

The cone-and-plate bioreactor consists of an inverted rotating cone and a stationary plate in which tissue samples are mounted. Culture medium fills the gap between the cone and plate. When the cone rotates, fluid flow and uniform shear stress are generated on top of the plate and tissue. Such device is capable of generating temporal variations in WSS magnitude. However, the WSS generated is along the circumferential cone direction, which prevents the replication of a multidirectional WSS [5]. Hence, a new bioreactor is required to replicate the changes in magnitude and directionality of the local WSS on native aortic tissue.

Therefore, **the objectives of this thesis were to quantify the multidirectional characteristics of the WSS caused by BAVs in the AA and to design a device capable of subjecting native aortic tissue to native BAV WSS magnitude and directionality.** The quantification of WSS multidirectionality is described in Specific Aim 1, the design

of the bioreactor is described in Specific Aim 2 and the determination of the device operating conditions is described in Specific Aim 3.

Specific Aim 1: To quantify the multidirectional characteristics of BAV aorta WSS in regions prone to dilation

Local WSS waveforms were obtained from valve-aorta FSI models published by our group [21], [63]. The local WSS was characterized over two circular regions (7 mm in diameter) located in the proximal section of the AA convexity and concavity. The instantaneous WSS vector was extracted and decomposed into its longitudinal and circumferential components. WSS multidirectionality was then quantified in terms of temporal shear magnitude (TSM) and oscillatory shear index (OSI) in both directions, and transverse WSS (transWSS). TSM and OSI are two frequently used indices for quantifying the time-averaged magnitude and the oscillation nature of shear stress. TransWSS is a new index for evaluating the multidirectionality of the flow by calculating the instantaneous WSS components perpendicular to the direction of the mean WSS.

Specific Aim 2: To design a cone-and-plate bioreactor replicating the temporal changes in WSS magnitude and directionality of BAV aortic tissue

The design was adapted from the cone-and-plate viscometer principle to subject aortic tissue to desired time-varying WSS magnitude and direction. The device was designed to accommodate four circular tissue samples. WSS magnitude was adjusted by rotating an inverted cone above the culture medium, resulting in a fluid flow of culture medium above the tissue specimens, and a WSS directly proportional to the cone

velocity. Temporal changes in WSS directionality on each sample were achieved by rotating the mounts supporting the tissue specimens. Computer-aided design (CAD) drawings for each part of the physical model were created.

Specific Aim 3: To determine the bioreactor operating conditions

This aim consisted of determining: 1.) the optimal dimensions of the bioreactor, 2.) appropriate operating conditions, and 3.) the torque requirements for servo motor selection. For the first task, CFD simulations were performed to assess the impact of tissue location and cone radius on the validity of the equation relating cone velocity and WSS. The predicted WSS magnitude and directionality were compared to the target WSS extracted from the convexity of the LR-BAV AA (Specific Aim 1) over a range of cone radii and tissue positions, and optimal bioreactor dimensions were determined based on the correlation coefficient between the target and predicted WSS. The second task implemented an iterative optimization method to determine the bioreactor operating conditions (cone angular velocity waveform, tissue angular velocity waveform) resulting in the desired WSS environment. Lastly for task 3, torque requirements were calculated for the cone and tissue rotations based on the optimized WSS waveform.

CHAPTER 3:

SPECIFIC AIM 1

3.1 Rationale

BAVs cause helical flow patterns and elevated WSS in the AA. Previous studies have typically focused on characterizing BAV WSS abnormalities in terms of magnitude and pulsatility abnormalities in global or longitudinal WSS [57]–[59]. Since the circumferential WSS is a significant component in helical flows, substantial abnormalities in circumferential WSS are also expected in BAV AAs. The quantification of this component was thus required to provide the full characterization of WSS abnormalities in BAV AAs.

3.2 Methods

3.2.1 TAV/BAV Aorta Fluid-Structure Interaction (FSI) Models

The FSI models used in this thesis were published previously by our lab. The models consisted of four aortic valve geometries (TAV, LR-BAV, RN-BAV and NL-BAV) connected to an idealized aorta reconstructed from a series of computed tomography images of a human aorta [64]. The aorta geometry included the AA and the aortic arch along with the entrance regions of the brachiocephalic (BCA), left common carotid (LCCA), and left subclavian (LSA) arteries. The four valves consisted of one

TAV geometry with three identical leaflets, and the three type-I BAV geometries with the raphe placed along the common free edge of the fused leaflets (Figure 13) [43], [65]. The compliance of the valve leaflets and the aortic wall was modeled using a three-parameter Mooney-Rivlin model and a linear elastic model, respectively, calibrated with respect to published tensile test data on valvular and aortic tissue [43]. Blood was modeled as an incompressible, homogeneous and Newtonian fluid (density: 1050 kg/m^3 ; dynamic viscosity: $0.0035 \text{ Pa}\cdot\text{s}$). Fully coupled, two-way FSI simulations were performed in ANSYS 18.0 Fluent, Mechanical ADPL and System Coupling (ANSYS Inc) using the arbitrary Lagrangian-Eulerian (ALE) approach. The governing equations consisted of the momentum and continuity equations for the fluid domain, the momentum equation for the structural domain, and three coupling conditions enforcing continuity of displacements, velocities and tractions at the fluid-structure interface. All models were subjected to the same physiologic transvalvular pressure waveform (0/12 mmHg, 2:1 diastolic/systolic ratio). The simulations predicted a cardiac output of 4.5 L/min for the TAV aorta, and 4.0 L/min for the BAV aorta models, respectively [66], [67], which fall within the range reported by published clinical studies [57].

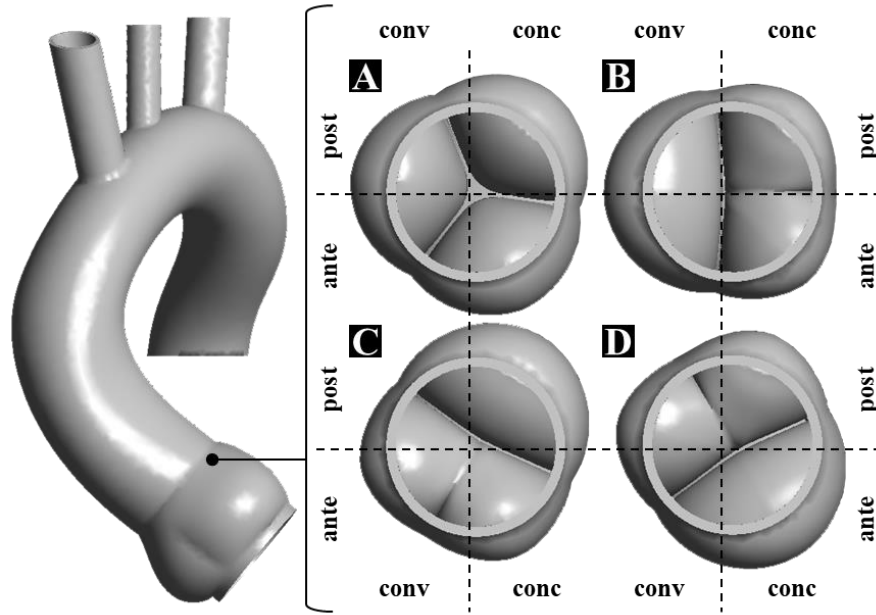


Figure 13. Valve-aorta FSI models. A.) TAV; B.) LR-BAV; C.) RN-BAV; D.) NL-BAV

3.2.2 Longitudinal and Circumferential WSS Extraction

The WSS characterization was conducted in two circular target regions (7-mm diameter) located in the convexity and concavity of the proximal AA section (Figure 14-A). The surface-averaged WSS was extracted at each time step over one cardiac cycle. The vector was then decomposed into its instantaneous longitudinal and circumferential components, τ_{long} and τ_{circ} , respectively, following the procedure outlined below.

The longitudinal direction was identified as the normal unit vector $\hat{\mathbf{k}}$ to the cross section of the aorta intersecting the two target regions (Figure 14-B). For each interrogation region, the unit vector in the circumferential direction $\hat{\boldsymbol{\theta}}$ was obtained as the cross product between the outward unit normal vector $\hat{\mathbf{n}}$ to the target region and the

longitudinal unit vector:

$$\hat{\underline{\theta}} = \hat{\underline{n}} \times \hat{\underline{k}} \quad (1)$$

As a result of this calculation, the circumferential direction always pointed in the clockwise direction along the aortic wall, regardless of the location of the interrogation region. Lastly, the local longitudinal and circumferential WSS components were obtained by calculating the dot product between the local WSS vector and the respective unit vector in each direction:

$$\tau_{long} = \underline{\tau} \cdot \hat{\underline{k}} \quad (2)$$

and

$$\tau_{circ} = \underline{\tau} \cdot \hat{\underline{\theta}} \quad (3)$$

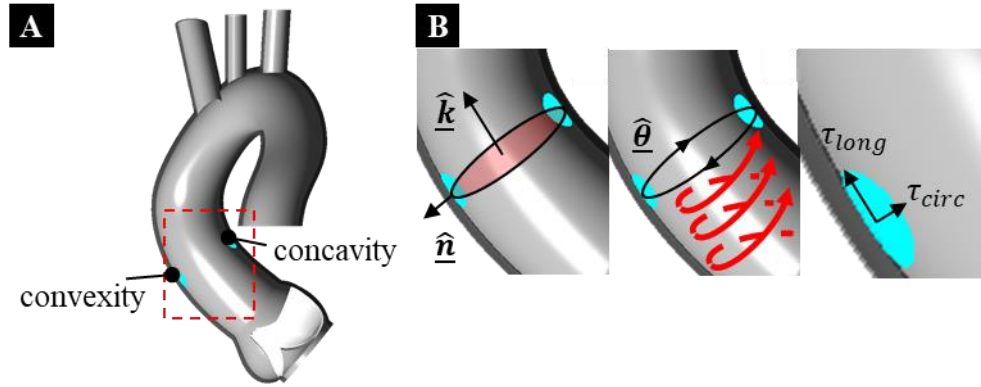


Figure 14. WSS extraction A.) at the convexity and concavity; B.) in longitudinal and circumferential directions.

3.2.3 WSS Characterization

The temporal changes in magnitude and direction of the local WSS vector $\underline{\tau}$ were assessed qualitatively by plotting the trace of the tip of the vector on a polar plot. The

average magnitude of the total, longitudinal and circumferential WSS over one cardiac cycle was quantified in terms of its respective TSM defined as

$$TSM = \frac{1}{T} \int_0^T |\tau_i| dt \quad (4)$$

where $\tau_i = [\tau_{total}, \tau_{long}, \tau_{circ}]$ and T is the cardiac period. The change in directionality of the WSS vector and the oscillatory nature of each component were quantified in terms of the OSI [68] defined as

$$OSI = \frac{1}{2} \left(1 - \frac{\left| \int_0^T \tau_i dt \right|}{\int_0^T |\tau_i| dt} \right) \quad (5)$$

The multidirectional characteristics of the flow were also assessed in terms of the transverse WSS (transWSS), which indicates the degree of deflection of the WSS vector from its average direction over the cardiac cycle [69], and is defined as

$$transWSS = \frac{1}{T} \int_0^T \left| \underline{\tau} \cdot \left(\hat{\mathbf{n}} \times \frac{\int_0^T \underline{\tau} dt}{\left| \int_0^T \underline{\tau} dt \right|} \right) \right| dt \quad (6)$$

The value of the transWSS ranges from 0 to the total TSM. If the WSS vector oscillates along the direction of the mean WSS vector over the entire cardiac cycle, then the flow is unidirectional and transWSS is close to 0. If a large portion of the instantaneous WSS vectors deviates from the mean WSS vector and contributes more toward the direction perpendicular to the mean vector, the flow is relatively multidirectional. The closer the transWSS value to its total TSM, the more multidirectional the flow is.

3.2.4 WSS Angular Variations

WSS overload has been reported at the convexity of the AA from previous studies. To assess the directionality of the elevated WSS, the temporal variations of WSS orientation at the convexity over the entire cardiac cycle were evaluated by calculating the angle (φ) between the longitudinal axis and the WSS vector at each time point. To calculate φ , the instantaneous WSS vector was first projected to the longitudinal axis by performing inner product on these two vectors (Equation 7). Then, the angle at each time step was obtained by taking the inverse cosine function (Equation 8).

$$\cos \varphi = \frac{\hat{\mathbf{k}} \cdot \underline{\boldsymbol{\tau}}}{|\underline{\boldsymbol{\tau}}|} \quad (7)$$

$$\varphi = \cos^{-1} \left(\frac{\hat{\mathbf{k}} \cdot \underline{\boldsymbol{\tau}}}{|\underline{\boldsymbol{\tau}}|} \right) \quad (8)$$

Angular variation was captured in full 360° range on the interrogation region over the entire cardiac cycle, essentially quantifying the instantaneous WSS change in direction at one specific location. This waveform was then equally segmented into 36 sectors along a unit circle, with instantaneous WSS sorted into the corresponding sectors based on its angle orientation. The average WSS magnitude was then calculated for each segment, and set as its dominant value.

To adequately quantify the change in direction associated with significant WSS magnitudes, a criterion was established for all morphotypes. The maximum value was selected amongst all geometries, and WSS quantity was normalized to it. WSS was considered significant when the value exceeds 50% of the maximum WSS magnitude

found among all the morphotypes. Polar histograms were created and used to identify the angle distribution of the abnormal WSS magnitude (i.e., when the WSS magnitude is 50% larger than the maximum WSS among all morphotypes). The more quantities of sectors exceed this 50% criterion are obtained means the larger range of angles the WSS orientation covers.

3.3 Results

3.3.1 WSS Orientation and Angular Variations

The time history of the WSS vectors predicted in the convexity and concavity of the proximal AA for the four valves are provided as videos in Appendix A and as polar plots in Figure 15. While the results suggest that all valves subject the proximal aortic wall to substantial changes in WSS directionality, TAV and BAV WSS differ in their range of rotation and overall magnitude.

To examine the angle distribution without considering the WSS magnitude, the TAV resulted in a wider range of WSS angles in the convexity than the BAVs (see Table 1). The TAV WSS vectors in the convexity and concavity were oriented at an average angle of 286° and 55° , respectively, relative to the longitudinal direction over the cardiac cycle. In the BAV aortas, the increased flow helicity tended to align the WSS vectors along the circumferential direction (convexity WSS average angle: 255° ; concavity WSS average angle: 185°).

However, when taking the WSS magnitude into consideration (Figure 16), the majority of the sectors in TAV polar plot fell within 50% of the maximum WSS magnitude criterion among all morphotypes. Since TAV represented the normal

physiologic case, sectors with WSS magnitude exceeded this 50% criterion is considered as significant overload. All BAVs exhibited elevated WSS magnitude in the proximal AA convexity, and those levels were experienced over a wide range of angles (Figure 17).

The range of the angles for each model is listed in Table 2.

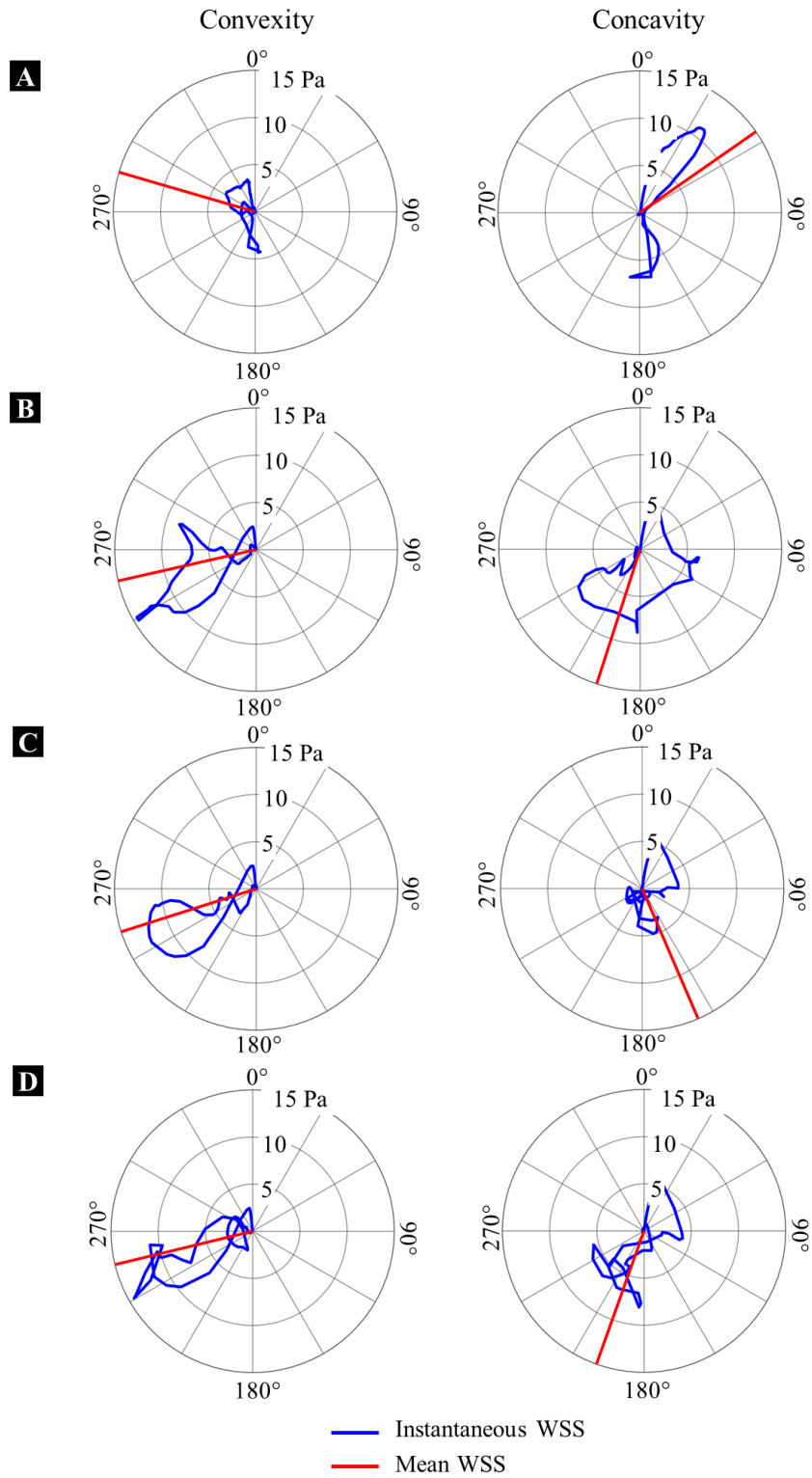


Figure 15. WSS magnitude vs. orientation in proximal convexity and concavity of A.) TAV, B.) LR-BAV, C.) RN-BAV and D.) NL-BAV aorta models

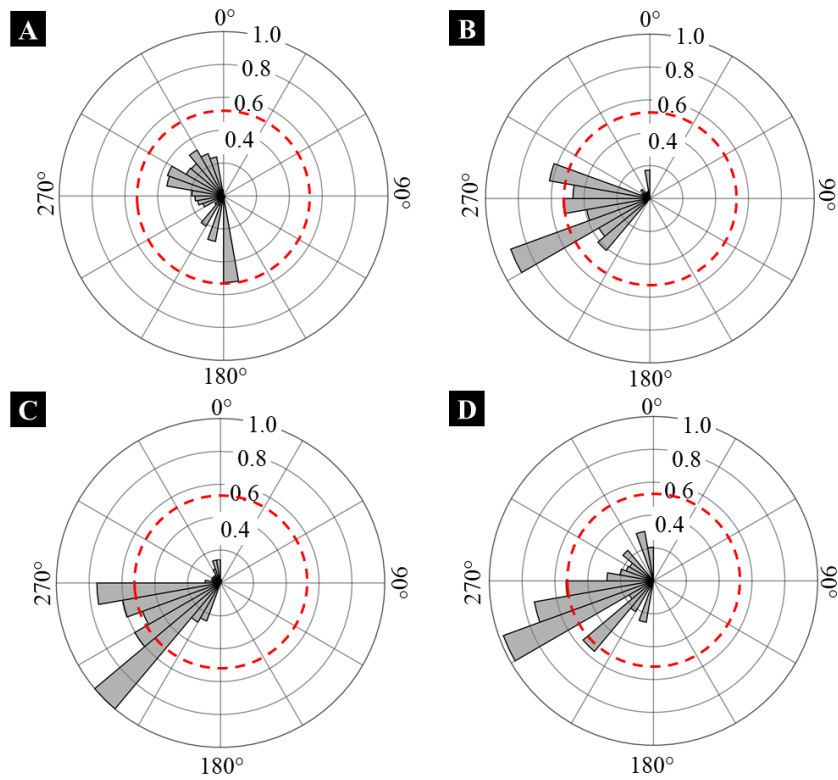


Figure 16. Angular distribution of normalized mean WSS magnitude at the proximal convexity of the A.) TAV; B.) LR-BAV; C.) RN-BAV and D.) NL-BAV aortas. The orange dash line represents the 50% threshold.

Table 1. Angle distribution in the convexity of the AA of all models

	TAV	LR-BAV	RN-BAV	NL-BAV
Range of Angles	180°	130°	150°	160°

Table 2. Width of WSS angle range for WSS magnitudes exceeding 50% of the maximum WSS at the proximal convexity for all models

	TAV	LR-BAV	RN-BAV	NL-BAV
Range of Angles	10°	30°	50°	40°

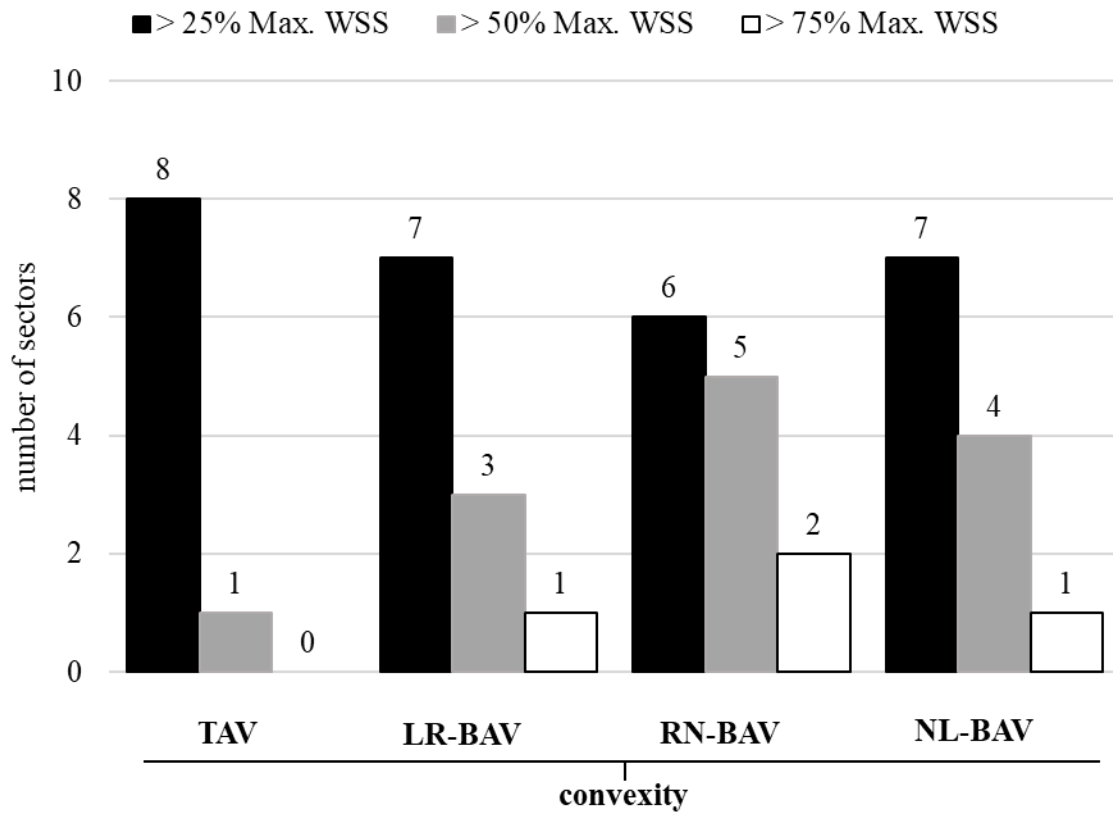


Figure 17. Summary of the number of sectors satisfying each criterion at the convexity of AA for all valve-aorta models

3.3.2 WSS Magnitude Characteristics

WSS characteristics were quantified in the proximal AA convexity and concavity of TAV and BAV AAs. Both the longitudinal and circumferential WSS components were examined to assess the multidirectionality of the local WSS environment.

Total TSM

The raw data of the total TSM were summarized in Table 3. The total TSM was higher on the proximal AA convexity downstream of a BAV than downstream of a TAV,

regardless of the BAV morphotype (Figure 18). The models predicted overall WSS magnitude overloads in all BAV AAs (LR-BAV; 134.4% increase, RN-BAV; 105.1% increase, and NL-BAV; 95.6% increase with respect to the TAV). In contrast, total TSM calculations in the proximal concavity revealed an overall decrease in WSS magnitude (LR-BAV; 23.4% decrease, RN-BAV; 52.9% decrease, and NL-BAV; 32.4% decrease with respect to the TAV).

An apparent trend observed was that the WSS overload on the convexity was higher than that in the concavity for all BAV morphotypes. Although the LR-BAV generated the highest values at both locations, the overload observed in the convexity was substantially larger (37.8% increase) than in the concavity. The convexity of the RN-BAV aorta experienced the most dramatic change in magnitude among all morphotypes (96.0% increase vs. concavity).

Table 3. Total TSM (Pa) at convexity and concavity of all valve-aorta models

	Convexity	Concavity
TAV	1.44	3.20
LR-BAV	3.38	2.45
RN-BAV	2.96	1.51
NL-BAV	2.82	2.16

Longitudinal TSM

The raw data of the longitudinal TSM were summarized in Table 4. Similar to the trend observed with the total TSM, the BAVs subjected the aortic wall to overloads in

longitudinal WSS in the proximal AA convexity (LR-BAV; 53.3% increase, RN-BAV; 38.3% increase, and NL-BAV; 31.5% increase with respect to the TAV). Longitudinal TSM predictions made in the concavity exhibited the same trend as the total TSM, marked by an overall decrease in TSM (LR-BAV: 37.6% decrease, RN-BAV: 57.5% decrease, and NL-BAV: 34.8% decrease with respect to the TAV). However, a different pattern emerged in the concavity where BAVs generated higher longitudinal TSM than in the convexity (LR-BAV; 11.4% increase, RN-BAV; 17.3% decrease, and NL-BAV; 27.3% increase with respect to the convexity).

Table 4. Longitudinal TSM (Pa) at convexity and concavity of all valve-aorta models

	Convexity	Concavity
TAV	0.96	2.67
LR-BAV	1.48	1.67
RN-BAV	1.33	1.14
NL-BAV	1.27	1.74

Circumferential TSM

The raw data of the circumferential TSM were summarized in Table 5. All BAV morphotypes generated significant overloads in circumferential TSM on convexity of the AA (LR-BAV: 242.4% increase, RN-BAV: 194.0% increase, and NL-BAV; 180.7% increase with respect to the TAV). Furthermore, the circumferential TSM values are larger than the longitudinal TSM shown in Figure 18, suggesting that the circumferential WSS is the dominant component in the convexity of all BAV AAs.

As compared to the proximal convexity, the concavity of BAV AAs exhibited an overall decrease in circumferential TSM (LR-BAV: 47.9% decrease, RN-BAV: 70.3% decrease, NL-BAV: 57.4% decrease vs. convexity). To compare the circumferential TSM and the longitudinal TSM in the concavity of AA for all models, the longitudinal TSM is higher than circumferential TSM for all models. That is, the flow is dominated by the longitudinal component in the concavity for all valve-aorta models. The only exception is with the LR-BAV morphotype for which both stress components are essentially similar (longitudinal TSM: 1.67 Pa; circumferential TSM: 1.48 Pa), suggesting the strong multidirectionality of the WSS environment generated by this morphotype.

Table 5. Circumferential TSM (Pa) at convexity and concavity of all valve-aorta models

	Convexity	Concavity
TAV	0.83	1.59
LR-BAV	2.85	1.49
RN-BAV	2.45	0.73
NL-BAV	2.34	0.99

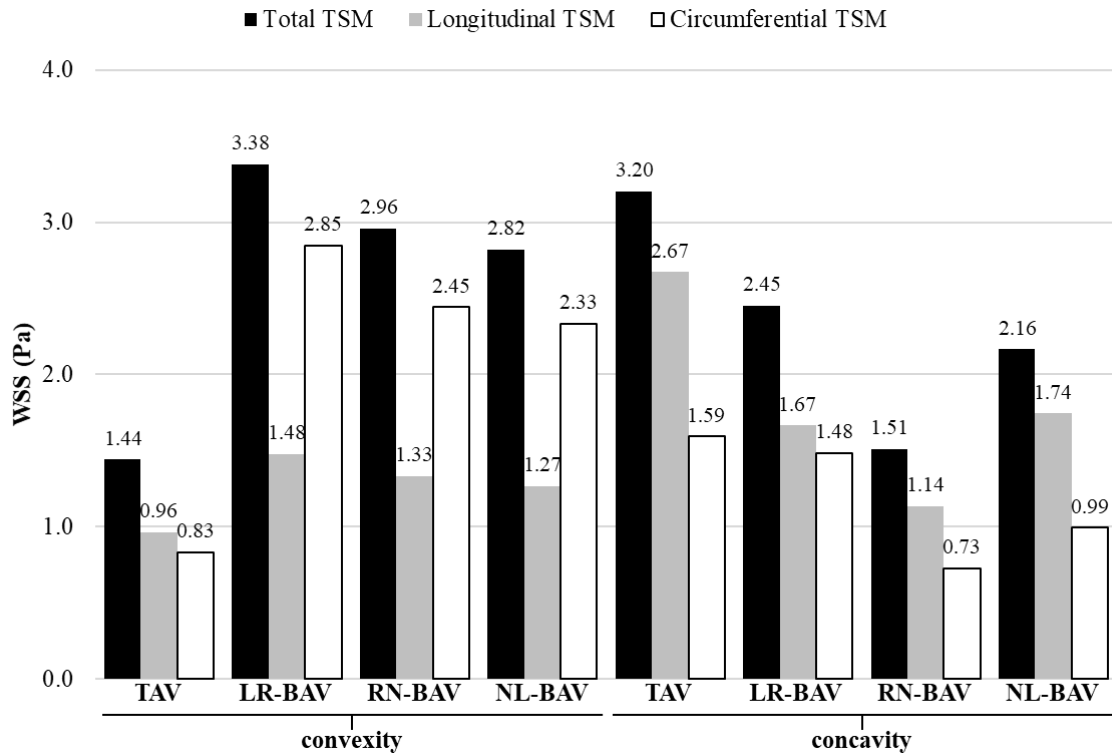


Figure 18. Total, longitudinal and circumferential TSM at the convexity and concavity of the proximal AA

3.3.3 WSS Directionality Characteristics

The WSS directionality was characterized in terms of OSI and transWSS. was quantified in the longitudinal and circumferential directions, in both the proximal AA convexity and concavity for all valves. The OSI in the longitudinal and circumferential directions were abbreviated as LOSI and COSI, respectively. The results are summarized in Figure 19.

Longitudinal OSI

In the proximal AA, all models generated WSS oscillation in the longitudinal direction (Table 6). This is likely due to the successive forward and backward flows generated during systole and diastole, respectively. Furthermore, the largest LOSI was observed in the TAV AA. To be more specific, the LR-BAV, RN-BAV and NL-BAV resulted in a 0.10-point, 0.17-point and 0.10-point decrease in LOSI in the convexity, respectively, relative to the TAV. Among all BAV morphotypes, the RN-BAV predicted the highest LOSI in the concavity.

The comparison of the OSI predictions in the convexity and concavity of BAV AAs reveals that both the LR- and NL-BAV subjected the convexity to higher LOSI than the concavity (LR-BAV: 0.04-point increase; NL-BAV: 0.06-point increase vs. concavity). This trend was opposite with the RN-BAV, which subjected the wall convexity to lower LOSI than the concavity (0.12-point decrease).

Circumferential OSI

COSI values extracted in the AA convexity of all models were close/equal to zero (Table 7), suggesting the absence of back-and-forth oscillation of the circumferential WSS component. In contrast, while all BAVs generated oscillatory WSS in both longitudinal and circumferential directions in the proximal AA concavity ($\text{LOSI} > 0.22$, $\text{COSI} > 0.32$), the TAV only generated oscillations in longitudinal WSS ($\text{LOSI} = 0.30$, $\text{COSI} = 0.02$).

Table 6. Longitudinal OSI at convexity and concavity of all valve-aorta models

	Convexity	Concavity
TAV	0.38	0.30
LR-BAV	0.28	0.24
RN-BAV	0.21	0.33
NL-BAV	0.28	0.22

Table 7. Circumferential OSI at convexity and concavity of all valve-aorta models

	Convexity	Concavity
TAV	0.02	0.02
LR-BAV	0.00	0.40
RN-BAV	0.00	0.40
NL-BAV	0.00	0.32

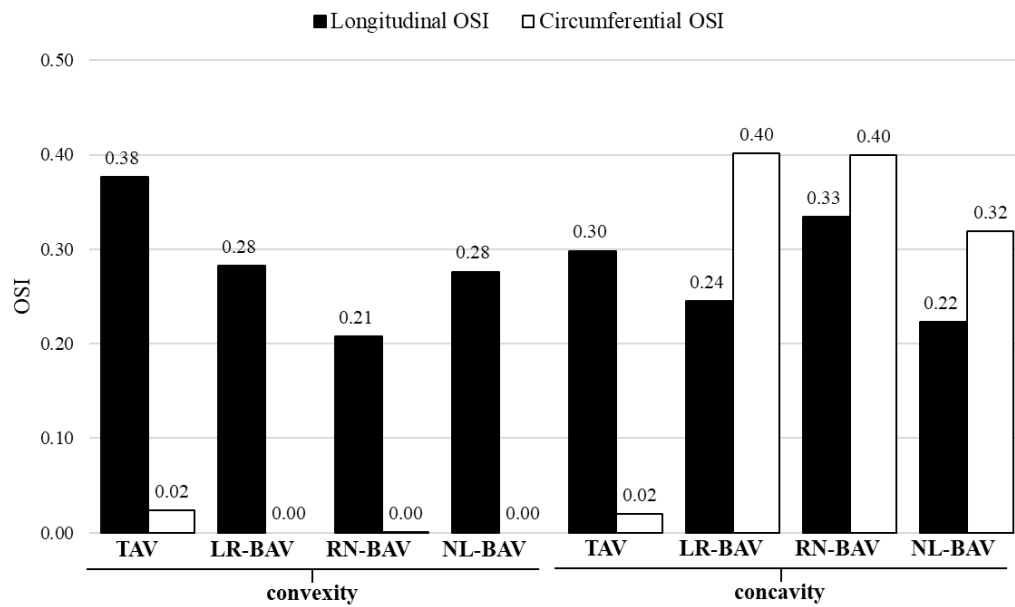


Figure 19. Longitudinal and circumferential OSI at the convexity and concavity of the proximal AA

Transverse WSS

The raw data of the transWSS and its ratio to the total TSM in the proximal AA for all models are reported in Table 8. The higher the ratio, the greater the flow multidirectionality. In the convexity of the proximal AA, all BAVs generated relatively low WSS directionality (transWSS/total TSM ratio < 37.6%) relative to the TAV (transWSS/total TSM ratio = 61.1%). In contrast, all models resulted in relatively high WSS directionality in the concavity (transWSS/total TSM ratio > 70.9%).

Table 8. transWSS and transWSS/total TSM ratio in the convexity and concavity of all valve-aorta models.

	Convexity		Concavity	
	transWSS (Pa)	Ratio	transWSS (Pa)	Ratio
TAV	0.88	61.1%	2.27	70.9%
LR-BAV	1.27	37.6%	1.76	71.8%
RN-BAV	0.84	28.4%	1.18	78.1%
NL-BAV	0.93	33.0%	1.84	85.2%

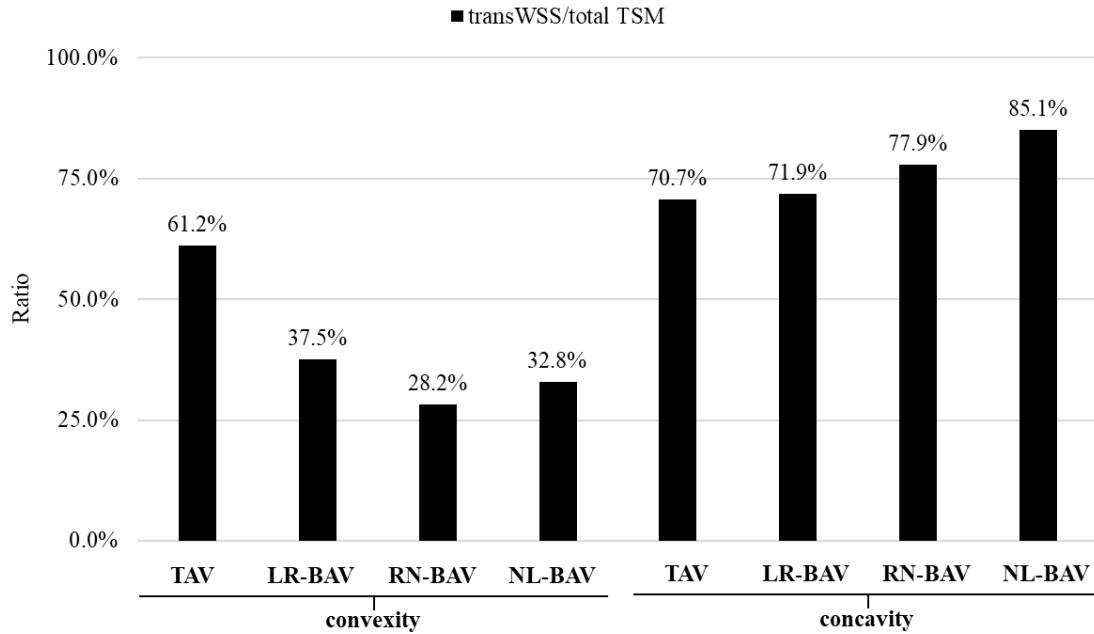


Figure 20. Ratio of transWSS and total TSM in the convexity and concavity of the proximal AA for all models.

3.4 Summary

WSS overloads were observed in the proximal convexity of all BAV AAs, with the LR-BAV generating the most substantial increase. While both longitudinal and circumferential TSM were increased in BAV AAs, the circumferential WSS component dominates over the longitudinal component.

The multidirectionality of the WSS in the convexity was analyzed through characterization of the angular distribution of the sectors. All BAV AAs exhibited wider WSS angular ranges and larger WSS levels relative to the TAV AA. Asymmetric WSS directionality patterns were observed in which high transWSS was observed in the convexity of the TAV AA and the concavity of all models, while relatively lower transWSS was obtained in the convexity of all BAV AAs.

CHAPTER 4:

SPECIFIC AIM 2

4.1 Rationale

Previous *in vivo* studies [13], [21], [38], [40], [41], [70], [71] have suggested that the WSS overload caused by BAVs on the aortic wall may contribute to aortic dilation. However, those studies only focused on the longitudinal WSS component, discarding the multidirectional nature of BAV WSS and the potential role played by the circumferential WSS component. As a result, bioreactors used in BAV aortopathy studies have consisted of cone-and-plate systems subjecting aortic tissue to longitudinal BAV AA WSS. The elucidation of the cause-and-effect relationship between BAV WSS and tissue biology requires a device capable of replicating the time-varying magnitude and directionality of the native WSS. To address this need, this aim describes the design of a novel device capable of subjecting multiple tissue samples to time-varying WSS magnitude and directionality, while maintaining tissue viability through nutrient and oxygen supply.

4.2 Design Principle

4.2.1 Components Description

The design principle is based on a cone-and-plate bioreactor, which consists of an inverted cone rotating above a stationary plate and driving a fluid flow in the gap between the cone and the plate, where ω_c is the cone angular velocity, R_c is the radius of the cone, ρ is the fluid density, μ is the dynamic viscosity, α is the cone angle, h_0 is the gap and $h(r)$ is the height between the cone and plate at the radial location r (Figure 21). As a result, a WSS is exerted on the plate.

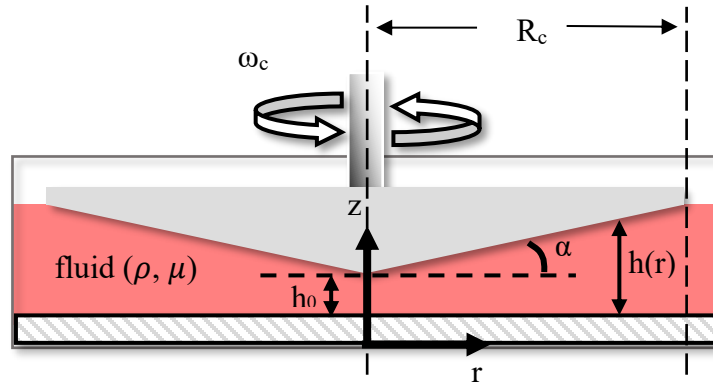


Figure 21. Cone-and-plate bioreactor.

The Reynolds number for this cone-and-plate bioreactor is defined as,

$$\text{Re} = \frac{R_c^2 \alpha^2 \omega_c}{12\nu} \quad (9)$$

where ν is the kinematic viscosity [72].

Previous study has demonstrated that to produce an axisymmetric, laminar and tangential flow, the Reynolds number has to be less than 1. If the Reynolds number falls within a range from 1 to 4, secondary flow effects will be present, and as the value goes beyond 4, the flow is fully turbulent [73].

4.2.2 Fluid Mechanics of the Cone-and-Plate Device

The relation between the cone angular velocity and the resultant WSS on the plate can be determined by solving the Navier-Stokes and continuity equations. The Navier-Stokes and continuity equations were simplified based on five assumptions: i.) steady flow ($\frac{\partial}{\partial t} = 0$), ii.) purely circumferential flow ($v_r = 0$ and $v_z = 0$), iii.) rotational symmetric flow ($\frac{\partial v}{\partial \theta} = 0$), iv.) no body force ($g = 0$) and v.) no imposed pressure gradient in the tangential direction ($\frac{\partial p}{\partial \theta} = 0$). In addition, under the assumption of a very small cone angle α , the height of the fluid gap can be formulated as

$$h(r) = h_0 + r \tan \alpha = h_0 + r\alpha \quad (10)$$

Based on the assumptions, the Navier-Stokes equations reduce to:

$$\text{N-S/r:} \quad \rho \left(\frac{v_\theta^2}{r} \right) = \frac{\partial p}{\partial r} \quad (11)$$

$$\text{N-S/}\theta\text{:} \quad 0 = \mu \left[\frac{\partial}{\partial r} \left(\frac{1}{r} \frac{\partial}{\partial r} (r v_\theta) \right) + \frac{\partial^2 v_\theta}{\partial z^2} \right] \quad (12)$$

$$\text{N-S/}z\text{:} \quad 0 = \frac{-\partial p}{\partial z} \quad (13)$$

By introducing the following scaled variables,

$$r^* = \frac{r}{R}; \quad z^* = \frac{z}{h_0}; \quad v_\theta^* = \frac{v_\theta}{R\omega},$$

the N-S/ θ equation can then be rewritten:

$$0 = \left[\frac{\partial}{\partial r^*} \left(\frac{1}{r^*} \frac{\partial}{\partial r^*} (r^* v_\theta^*) \right) + \frac{R^2}{h_0^2} \frac{\partial^2 v_\theta^*}{\partial z^{*2}} \right] \quad (14)$$

Under the assumption of a very small gap between the cone apex and the plate (i.e.,

$h_0 \ll R$), $\left(\frac{R}{h_0}\right)^2 \gg 1$ and $\frac{\partial^2 v_\theta}{\partial z^2}$ is the dominant term of the equation. The scaled Navier-

Stokes equation simplifies to

$$\frac{\partial^2 v_\theta}{\partial z^2} = 0 \quad (15)$$

This equation can be integrated twice to obtain the tangential velocity equation:

$$v_\theta = C_1 z + C_2 \quad (16)$$

From the no-slip conditions at the plate, $v_\theta(z=0) = 0$, and at cone, $v_\theta(z=h(r)) = r\omega_c$,

the constants of integration are determined as $C_2 = 0$ and $C_1 = \frac{r\omega_{cone}}{h_0 + r\alpha}$, respectively.

Equation 16 then can be re-written as

$$v_\theta = \frac{r\omega_c}{h_0 + r\alpha} z \quad (17)$$

The shear stress along the θ -direction is defined as $\tau_{\theta z} = \mu \frac{\partial v_\theta}{\partial z}$, where μ is the dynamic

viscosity of the fluid. Using Equation 17, it results that

$$\tau_{\theta z} = \mu \frac{r\omega_c}{h_0 + r\alpha} \quad (18)$$

In the limit of a small gap between the cone apex and the plate (i.e., $h_0 \rightarrow 0$),

theoretically, the WSS magnitude generated by the cone rotation is directly proportional to the prescribed cone angular velocity, and the relation between $\tau_{\theta z}$ and ω_c reduces to

$$\tau_{\theta z} = \frac{\mu}{\alpha} \omega_c \quad (19)$$

This equation demonstrates the existence of a uniform tangential WSS on the

surface of the plate when certain conditions are met (i.e., small cone angle, cone apex extremely close to the bottom plate, large cone radius relative to the height of the fluid gap, and low Reynolds number to ensure circumferential flow). However, practically, the distance between the cone apex and the bottom plate is finite and the WSS becomes spatially-dependent on the bottom plate (see Equation 18). Therefore, the design of the bioreactor needs to account for the radial dependence of the WSS [49].

4.3 Design Solution

4.3.1 Overview

As demonstrated in Specific Aim 1, the WSS characteristics in TAV and BAV AAs not only differ in magnitude but also in directionality (i.e., increased WSS with wider angular variations were observed in BAV AAs). Besides, both WSS magnitude and directionality change as a function of time. Given that the cone rotation can only produce a tangential WSS on the plate surface, a change in WSS directionality can only be

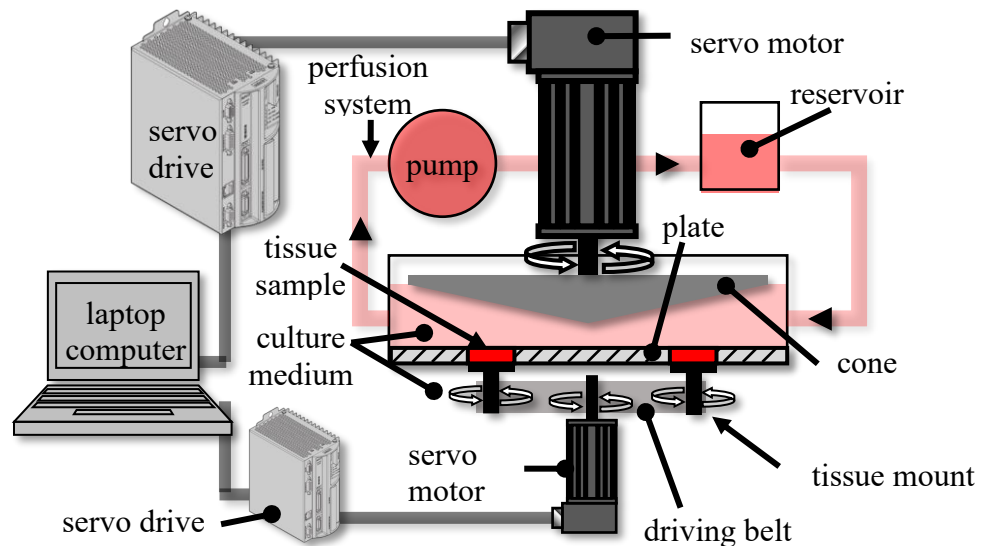


Figure 22. Culture system schematic

achieved by altering the orientation of the tissue specimens mounted on the plate. The original cone-and-plate bioreactor design was therefore adapted to implement rotating tissue mounts driven by a programmable servo motor. Four tissue mounts were equi-angularly placed on the bottom plate to minimize the possible flow disturbances caused by one sample on the sample immediately downstream, while providing a sufficient number of samples to generate statistically meaningful biological results. Perfusion pumps were used to circulate culture medium through the system (Figure 22).

The entire system is composed of four major modules and a driving system. The modules include the cone assembly, the tissue mount assembly, the bioreactor case assembly and the perfusion system (Figure 23). The driving system include servo/ motors. The function and design of each part is described in the following sections and the definition of each part is attached in Appendix B.

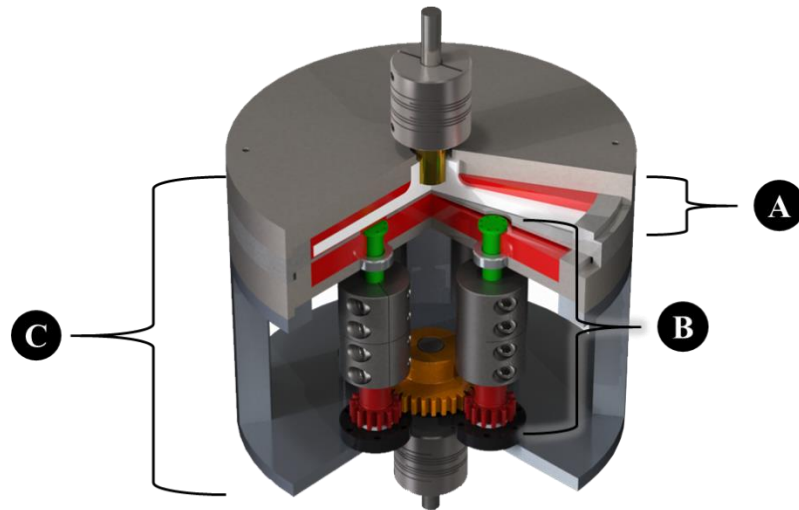


Figure 23. Assembly components. A.) Cone assembly; B.) Tissue mount assembly; C.) Bioreactor case assembly

4.3.2 Cone Assembly

The cone assembly is responsible for achieving the desired time-dependent WSS magnitude. To achieve any desired WSS magnitude, Equation 12 is used, and the corresponding angular velocity will then be prescribed for the cone motion. In theory, the computed WSS output from the calculated cone angular velocity should match the target WSS.

The cone assembly consists of an inverted cone, a top driving shaft, a top flange and a bottom plate container (Figure 24). The dimensions of the cone and the plate were determined in the Specific Aim 3 through CFD analysis. The cone has an 80 mm diameter and a 179.5° cone angle, and is made of Delrin. The material of the cone was chosen based on the previous cone-and-plate bioreactor design [74]. In order to generate a WSS distribution on the plate as uniformly as possible, it is required to ensure the cone angle is 0.5° from the bottom plate when machining the part.

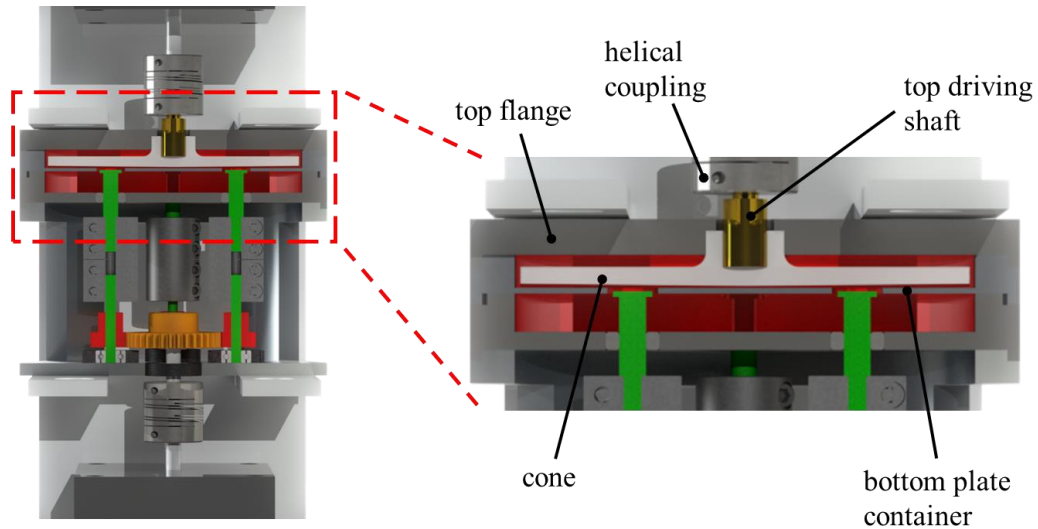


Figure 24. Cone assembly in cross-sectional view. Showing A.) components and their corresponding locations; B.) cone in closer view

The top driving shaft is a rotatory step-down shaft made of aluminum (5.00 mm diameter, 12.0 mm length; 4.76 mm step diameter, 5.00 mm step length). The step-down end of the shaft is connected to the motor shaft through a helical coupling (61005K191, McMaster-Carr, Aurora, OH), and the other end of the shaft is connected to the cone.

The top flange is placed above the cone. The top flange has a 98 mm outer diameter, 93.5 mm inner diameter and 8.35 mm thickness, and is made of biocompatible stainless steel. It is beneficial to use biocompatible stainless steel, because: 1.) it allows direct contact of the culture medium without causing any chemical reaction; 2.) autoclave can be performed to ensure the part is sterile and thus prevent contamination problems.

The plate and the side wall are integrated into one piece, and becomes a bottom plate container. The bottom plate container is placed inferior to the cone with a vertical distance of 200 μm from the cone apex to the plate. Raised surfaces were created on both the top and bottom of the container in order to fit with the edges of the top flange and the working fluid reservoir (introduced in section 4.2.4), respectively. The raised surface at the top connects to the top flange, and it has a 93.5 mm outer diameter, a 82.0 mm inner diameter and a 2.00 mm thickness. The side wall of the container has a 98.0 mm outer diameter, a 93.5 mm inner diameter and a 5.88 mm height. The raised surface at the bottom connects to the working fluid reservoir, and it has a 98.0 mm outer diameter and a 93.5 mm inner diameter and a 2.00 mm thickness. Four circular openings (9.00 mm diameter) were created 20 mm away from the plate center, and every 90° along the circumferential direction on the plate surface (82 mm diameter). These four circular openings are where the tissue samples will be located. The entire bottom plate container is also made of biocompatible stainless because of the same reasons described previously.

4.3.3 Tissue Mount Assembly

The tissue mount assembly is responsible for achieving the desired WSS directionality. The WSS generated by the cone rotation is always unidirectional. To expose the tissue to WSS in different directions, the tissue mounts are rotated as desired, which will then render relative orientation to the WSS.

The tissue mount assembly consists of four tissue mounts, four small driving shafts, one large driving shaft, four small driving gears, one large driving gear and five ball bearings. The tissue mount is a rotatable structure which was integrated from a circular platform and a rotatory step-down shaft, and is made of biocompatible stainless steel.

The circular platform is 7 mm in diameter and has eight pinholes align along the edge. The diameter of the platform was determined according to the previous design, in which the tissue samples were 7 mm in diameter. The tissue samples extracted from the aortic wall will be fixed on the circular platform by suturing the edge of the tissue through the pinholes. The step-down shaft (4.76 mm diameter, 14.0 mm length; 3.18 mm step diameter, 11.0 mm step length) is connected to the bottom shaft through helical coupling (6208K425, McMaster-Carr, Aurora, OH). The vertical height of the tissue mount was designed to be adjustable, in order to adapt the thickness of the tissue sample (Figure 25).

The small driving shaft is an aluminum cylinder (3.18 mm diameter, 28.0 mm length) with a small driving gear (57655K33, McMaster-Carr, Aurora, OH) attached to it. They are then installed onto a ball bearing (60355K501, McMaster-Carr, Aurora, OH) fixed at the bottom of the supporting cylinder (introduced in section 4.2.4).

The large driving shaft is a rotatory step-down shaft (6.35 mm diameter, 11 mm length;

4.76 mm step diameter, 40 mm step length) with a large driving gear installed on the top. It is attached to the supporting cylinder with a ball bearing (60355K501, McMaster-Carr, Aurora, OH), and connected to the bottom motor shaft through a helical coupling (61005K191, McMaster-Carr, Aurora, OH). The large driving gear received the rotatory force received from the motor shaft and transports it to the small driving gears. The small driving gears then trigger the rotation of the tissue mounts (Figure 26).

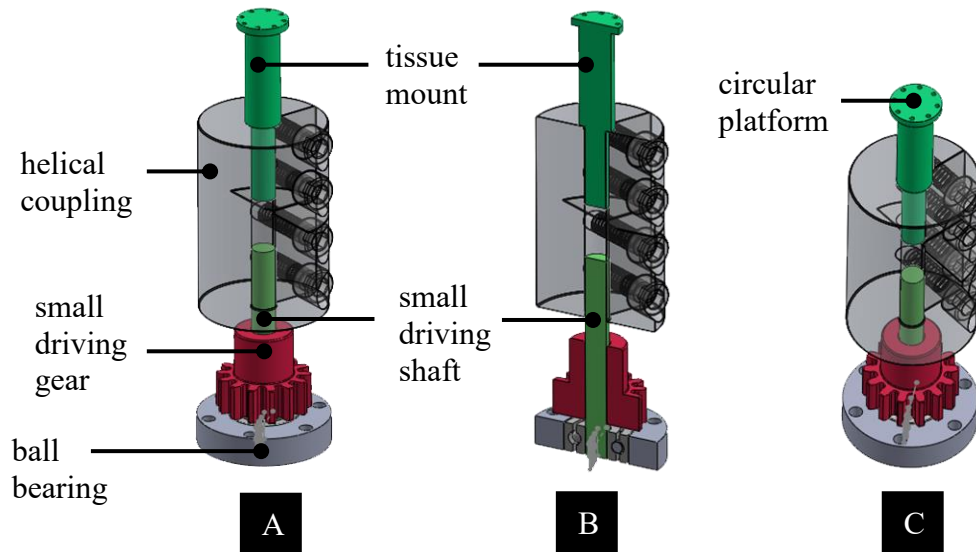


Figure 25. Tissue mount in A.) Overview; B.) Cross-sectional view; C.) Top view

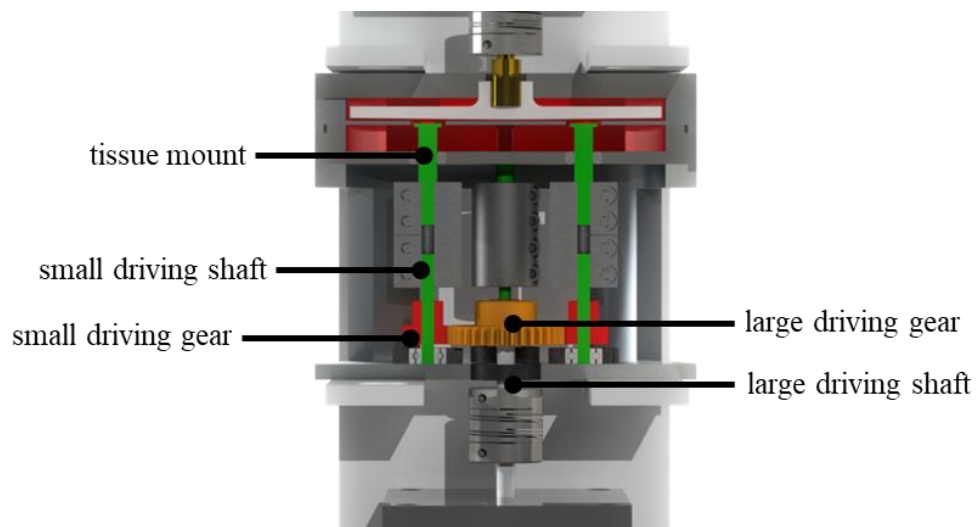


Figure 26. Tissue mount assembly in cross-sectional view

4.3.4 Bioreactor Case Assembly

A working fluid reservoir is placed inferior to the plate, and separates the gearings underneath from the fluid stored inside the reservoir. The structure is similar to the bottom plate container. The raised surface at the top connects to the bottom plate container, and the raised surface at the bottom connects to the supporting cylinder. Seals (13125K67, McMaster-Carr, Aurora, OH) are applied at the interface between the tissue mounts and the holes on the bottom of the working fluid reservoir to prevent the leaking of the fluid.

The working fluid reservoir combined with the top flange and the bottom plate container to form a closed space, which will be filled with culture medium (Dulbecco's Modified Eagle's Medium-high glucose, Sigma-Aldrich Co., St. Louis, MO; dynamic viscosity: $0.00095 \text{ kg}\cdot\text{m}^{-1}\text{s}^{-1}$).

A hollow-carved supporting cylinder is placed inferior to the working fluid reservoir to support the cone and tissue assemblies. As mentioned in the previous section, the small driving shafts and the corresponding ball bearings from the tissue mount assembly are fixed at the bottom of the supporting cylinder. The supporting cylinder has a 98.0 mm diameter, and 53.1 mm height, and is made of aluminum. The hollow-carved feature was designed for easy access to the tissue mount assembly (Figure 27).

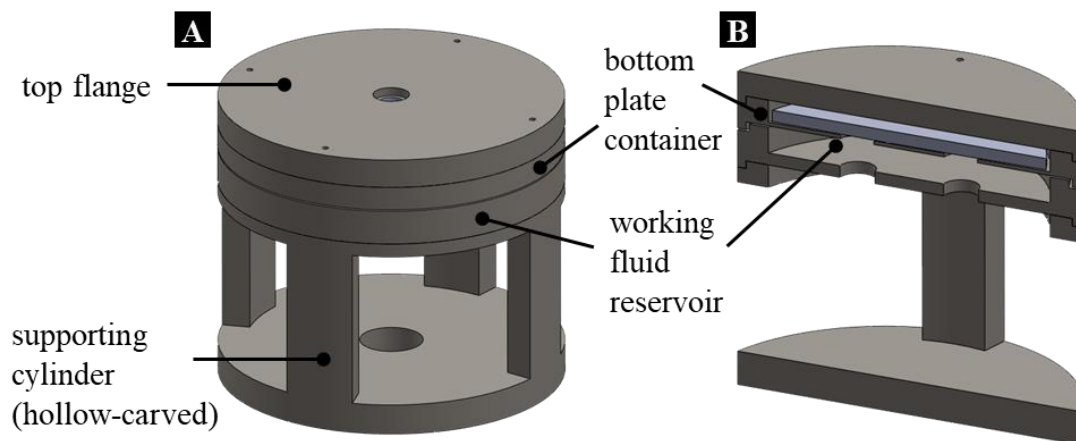


Figure 27. Bioreactor case assembly in A.) overview; B.) cross-sectional view

4.3.5 Perfusion System

Perfusion Pumps

Two perfusion pumps are required to circulate the culture medium through the culture system. One is responsible of transporting the culture medium from the external reservoir into the bioreactor, and the other is responsible of returning the excessive fluid back to the external reservoir for next round of circulation.

The total volume of the culture medium required to fill the bioreactor was calculated. The main requirement of the flow rates is that the pumps should be able to replenish the total volume of culture medium in the bioreactor every hour. Therefore, pumps with flow rates close to or higher than 0.87 mL/ min was required. Based on the minimum required flow rate, SP200 OEM Fixed-Flow Peristaltic Pump (APT Instruments, Rochester, IL) with a flow rate at 0.92 mL/min was selected.

External Culture Medium Reservoir

In order to supply the tissue samples in the bioreactor with fresh culture medium for 24 hours, the required amount of the fresh culture medium is 1247 mL. An external reservoir was designed in order to store the fresh culture medium before transported into the bioreactor. The external reservoir is a rectangular box with a fluid capacity of 1311 mL (101.6 mm length, 101.6 mm width and 127.0 mm height). The fluid capacity was designed to be 10% larger than the required fluid volume. Since the reservoir will directly contact with the culture medium, it is made of biocompatible stainless steel.

4.3.6 Driving System

Two servo/ motors were required to prescribe cone and tissue mount rotations. The motors are chosen from Parker-Hannifin Corporation, Cleveland, OH. Details about the determination of the operating conditions and the justification for selecting the motors are discussed in Specific Aim 3. Briefly, model number PM-FALR5AM8 was chosen for controlling the rotations of the cone and the tissue mounts.

Since this system consists of two servo/ motors and it is required that they operate at the exact same time steps, Parker Automation Controller (PAC) are added into the system to ensure the motors receive the signals and rotate simultaneously. PAC is a signal-integrated device. It combines the signals from two separate servos, and ensure the motors received the signals without any time difference.

4.4 Summary

A fluid shear stress bioreactor was designed based on the principle of the cone-and-plate viscometer, and modification was made at the bottom plate in which the tissue sample will be fixed on the free-rotated tissue mount. The desired WSS magnitude and directionality were then achieved by the cone and tissue rotation. The CAD drawings for each component in the culture system were generated, and model of the perfusion pumps were selected based on the required flow rate.

CHAPTER 5:

SPECIFIC AIM 3

5.1 Rationale

As mentioned in Specific Aim 2, a fluid shear stress bioreactor has been designed based on the principle of cone-and-plate viscometer to subject tissue sample to its native WSS environment. In this previous design, the cone is the only component that has motion. In order to replicate the WSS directionality, rotating tissue mounts were adapted into the current design, and thus changed the model operating environment. Therefore, it is required to study if changing the dimensions of the bioreactor will better satisfy Equation 18. The operating conditions for this new bioreactor also needed to be determined, and the proper servo/ motors were selected based on the suggested operating conditions.

5.2 Methods

The first objective of the CFD analysis was to determine the optimal dimensions of the bioreactor. The flow disturbances caused by the wall and tissue rotation effects were minimized with the optimal dimensions. The second objective was to determine the appropriate operating conditions through an iterative waveform optimization process. The third objective was to select the proper servo/ motors based on the operating conditions.

5.2.1 Computational Fluid Dynamics (CFD) Models

Bioreactor CFD models were created and mesh dependency tests were performed. These models were then used in Section 5.2.2 and 5.2.3 for determining the optimal dimensions and the operating conditions, respectively, for the bioreactor.

Bioreactor Geometry

To study how changing the dimensions of the bioreactor will have influences on the results, five bioreactors with different dimensions were considered, and the corresponding fluid domains in three-dimensions (3D) were created in SolidWorks and imported into ANSYS CFX. Owing to the symmetry, only a quarter of the bioreactor (i.e., a 90° slice) was created and used for the CFD simulation. This was beneficial for saving the computation time. Since there were no fluid-structure interactions involved and the focus was on the resultant WSS on the tissue surface, only the fluid domain was modeled in this CFD analysis. The fluid domain is the culture medium (Dulbecco's Modified Eagle's Medium-high glucose, Sigma-Aldrich Co., St. Louis, MO). The density and the dynamic viscosity are 1040 kg/m^3 and $0.00095 \text{ kg.m}^{-1}\text{s}^{-1}$, respectively.

Two scenarios were considered when determining the dimensions. The first scenario took only the radius of the bioreactor (R_c) (i.e., the distance from the cone apex to the lateral wall of the bioreactor) into account, and tissue was kept at the original location. In the second scenario, both the radius of the bioreactor and the tissue location (r) were manipulated. A total of five models were studied. Model 1 has a radius of 41 mm, and the distance from the plate center to the tissue center is 20 mm. Model 1 was considered as the original model, since the dimensions have been validated previously as

a good option for generating uniform WSS. Model 2 and 3 were defined as when both the radius and the tissue location increased by 20 percent and 50 percent, respectively. Finally, Model 4 and 5 were when only the radius was increased by 50 percent and 100 percent while maintaining the tissue at same location as in the original model. The other parameters, such as the angle of the cone (α), and the gap between the cone apex and the plate (h), were kept as the same through all models. The schematic of the bioreactor is as shown in Figure 28, and the summary of the dimensions of each model is as listed in Table 9.

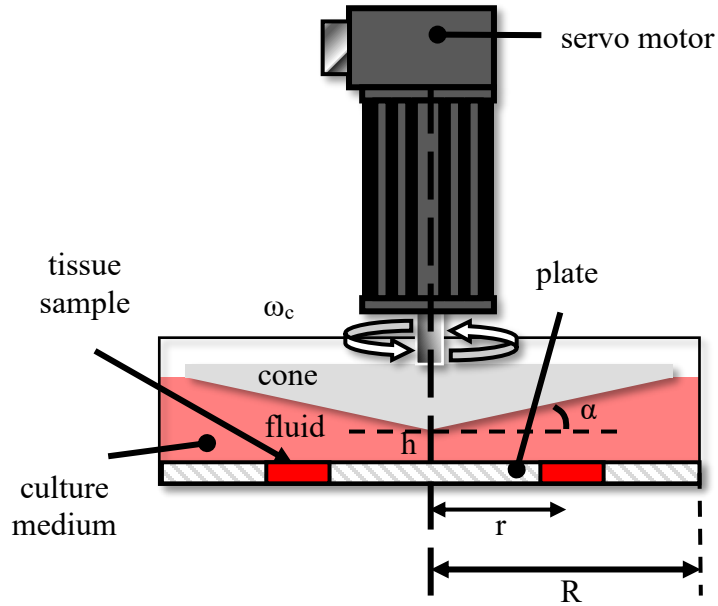


Figure 28. Bioreactor schematic ($h = 200 \mu\text{m}$ and $\alpha = 0.5^\circ$)

Table 9. Model numbers with their corresponding descriptions and dimensions

Model No.	Description	R (mm)	r (mm)
1	Original	41	20
2	20%	49.2	24
3	50%	61.5	30
4	50%, original tissue location	61.5	20
5	100%, original tissue location	82	20

Boundary Conditions

The entire geometry was divided into seven sections, which include the bottom plate, the lateral surface, the free surface, the cone surface, the tissue surface, and two symmetry sections (Figure 29). The bottom plate was a stationary no-slip wall condition, and it was where the tissue samples are placed. The lateral surface was the side wall of the bioreactor; therefore, it was assigned a stationary no-slip wall condition as well. The free surface is a 1-mm gap between the edge of the cone and the bioreactor wall, and a condition of zero shear was imposed. Both the cone surface and the tissue surface were assigned a no-slip rotating wall condition. However, when performing the mesh dependency test, the tissue surface was not prescribed with any motion. In other words, the tissue surface was just a no-slip stationary wall in the mesh dependency test. Finally, the symmetry sections were assigned a rotational periodicity boundary condition for the symmetric geometry.

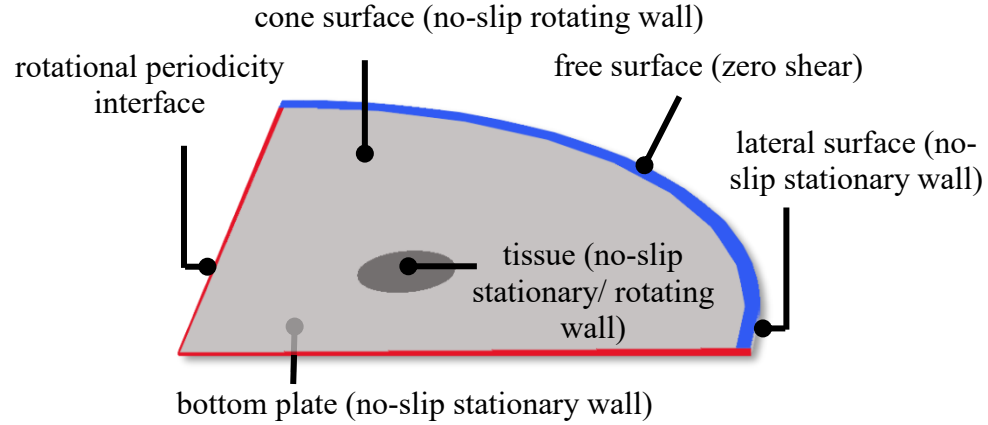


Figure 29. Boundary condition at each section

Mesh Dependency Test

Mesh dependency test was performed on each model. A constant WSS magnitude at 5 Pa was considered as the target. Since the cone angular velocity required for generating the target WSS depends on the radius of the tissue location, the corresponding speed was calculated for each model by using Equation 18, and is listed in Table 10.

Since the geometry is thin and curved, the “Proximity and Curvature” was selected for the size function, and the relevance center was set as “fine”. Inflation was applied at the tissue surface. The mesh was composed of tetrahedral elements and made finer in each round by increasing the number of cells across the gap from 3 to 8.

After the mesh was generated, a series of simulations were performed under steady state. The tissue surface was kept stationary, while the cone surface is rotating at a constant angular velocity corresponding to the value of target WSS. Once the simulation was completed, the computation time, the total WSS and the torque on the tissue were obtained in CFD-post, and recorded for each round. The percent differences then calculated and compared between successive mesh refinement. The mesh size was

determined based on the required computation time of the simulation and the accuracy of the results. The most propriate mesh size was the one costed acceptable amount of computation time while providing accurate and converged results (i.e., when the results show less than 5% change as compared with the previous round).

Table 10. The calculated cone angular velocity for each model for mesh dependency test

Model No.	Description	Cone Angular Velocity (Rad/s)
1	Original	98.6
2	20%	89.8
3	50%	81.0
4	50%, original tissue location	98.6
5	100%, original tissue location	98.6

5.2.2 Determination of Bioreactor Dimensions

The addition of the rotating tissue changes the operating environment. Thus, it was required to study whether changing the dimensions of the bioreactor will better satisfied Equation 18. To perform the analysis, the CFD models created in Section 5.2.1, and the target WSS waveforms obtained from the LR-BAV aorta FSI model in Specific Aim 1 were used.

To determine the optimal dimensions of the bioreactor, the bioreactor CFD models created in the previous section were switched from steady flow to transient flow. The boundary conditions for most sections of the geometry were kept as the same as described in the Section 5.2.1. Only slight changes were made on the cone surface and

tissue surface, in which both sections were assigned a no-slip rotating wall condition.

Since the cone rotation is responsible for achieving target WSS magnitude, Equation 18 was used in order to convert the target WSS to its corresponding cone angular velocity function. This cone angular velocity function was then prescribed to the cone surface in the CFD model.

Inner product was taken on the longitudinal vector ($\hat{\mathbf{k}}$) and the WSS vector ($\underline{\boldsymbol{\tau}}$) to obtain the angular variation as a function of time (Equation 7). After the angular variation as a function of time was obtained by taking inverse cosine (Equation 8), the tissue angular velocity function (ω_{tissue}) was then calculated by taking the derivative of the angular variation function (Equation 20). This function was then prescribed to the tissue surface in the CFD model. The simulations were performed for two cardiac cycles with a step size of 0.0025 s., and the data were extracted from the last cardiac cycle.

$$\omega_{tissue}(t) = \frac{d\phi}{dt} \quad (20)$$

Normalized Root-Mean-Squared Deviation Calculation

The WSS obtained from each model was then compared with the target WSS by calculating the normalized root-mean-squared deviation (NRMSD) as shown in Equation 21. The smaller value of the NRMSD means the output WSS matches the target WSS more as compared with the other models, and the model with smaller NRMSD was selected.

$$NRMSD = \frac{\sqrt{\sum (WSS_{computed} - WSS_{target})^2}}{MaxWSS_{target} - MinWSS_{target}} \quad (21)$$

5.2.2 Determination of the Operating Conditions

The determination was carried out on the model selected from the previous section. The purpose of this determination was to show that the bioreactor can generate a WSS output that matches the target WSS in terms of both magnitude and orientation.

As mention previously, the WSS magnitude generated on top of the tissue surface is directly proportional to the cone angular velocity under ideal conditions. However, the CFD analysis showed that the computed WSS on the tissue surface did not perfectly match to the target WSS magnitude (Figure 30). The reasons for this discrepancy include the fact that the bioreactor geometry was not ideal, and the flow disturbance caused by the high rotating speed of the cone and the tissue rotation. In order to achieve the target waveform, a waveform optimization method was proposed as described below.

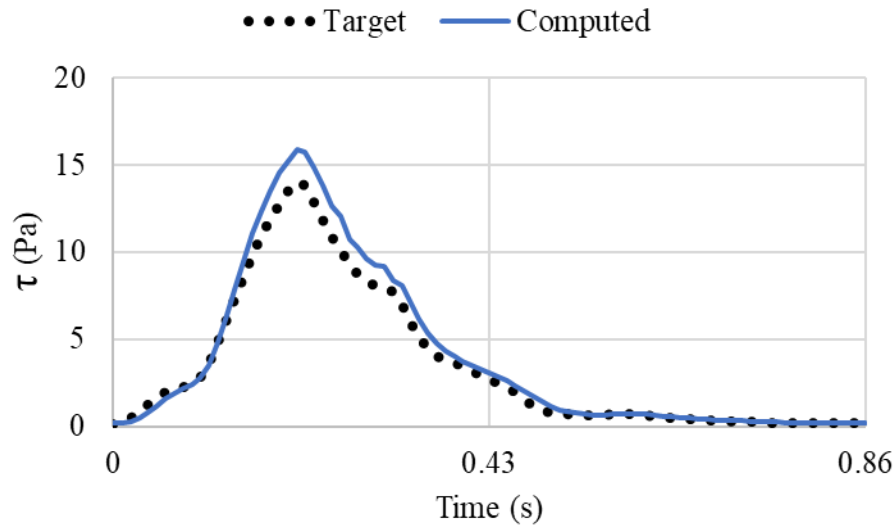


Figure 30. Comparison between the target WSS and the computed WSS output in magnitude. The computed WSS deviates from the target at the peak.

Strategy Outline

Figure 31 is the summary flowchart showing how the operating conditions were determined. Generally, any target WSS magnitude is converted to its corresponding angular velocity through Equation 18 (block 1-3). This corresponding angular velocity is applied to the cone surface in the CFD model, and simulation is performed (block 4). The computed $\tau(t)$ is then compared to the target, and the goal is to obtain a computed $\tau(t)$ which has a R^2 value with the target at least higher than 0.95 and yields a WSS output with % error lower than 5.0%. If the criteria are achieved, the WSS input is immediately validated (block 5). However, if they are not, then a waveform optimization process is required. WSS input is scaled, converted to its corresponding angular velocity, and prescribed to the cone rotation (block 6). This process is repeated until the computed $\tau(t)$ passes the criteria. Once the optimized WSS magnitude waveform is determined, the WSS angular variation on the tissue is then verified based on the optimized WSS magnitude waveform. Same criteria are applied. Details on how the waveform optimization process for the WSS magnitude was performed are discussed in the following section.

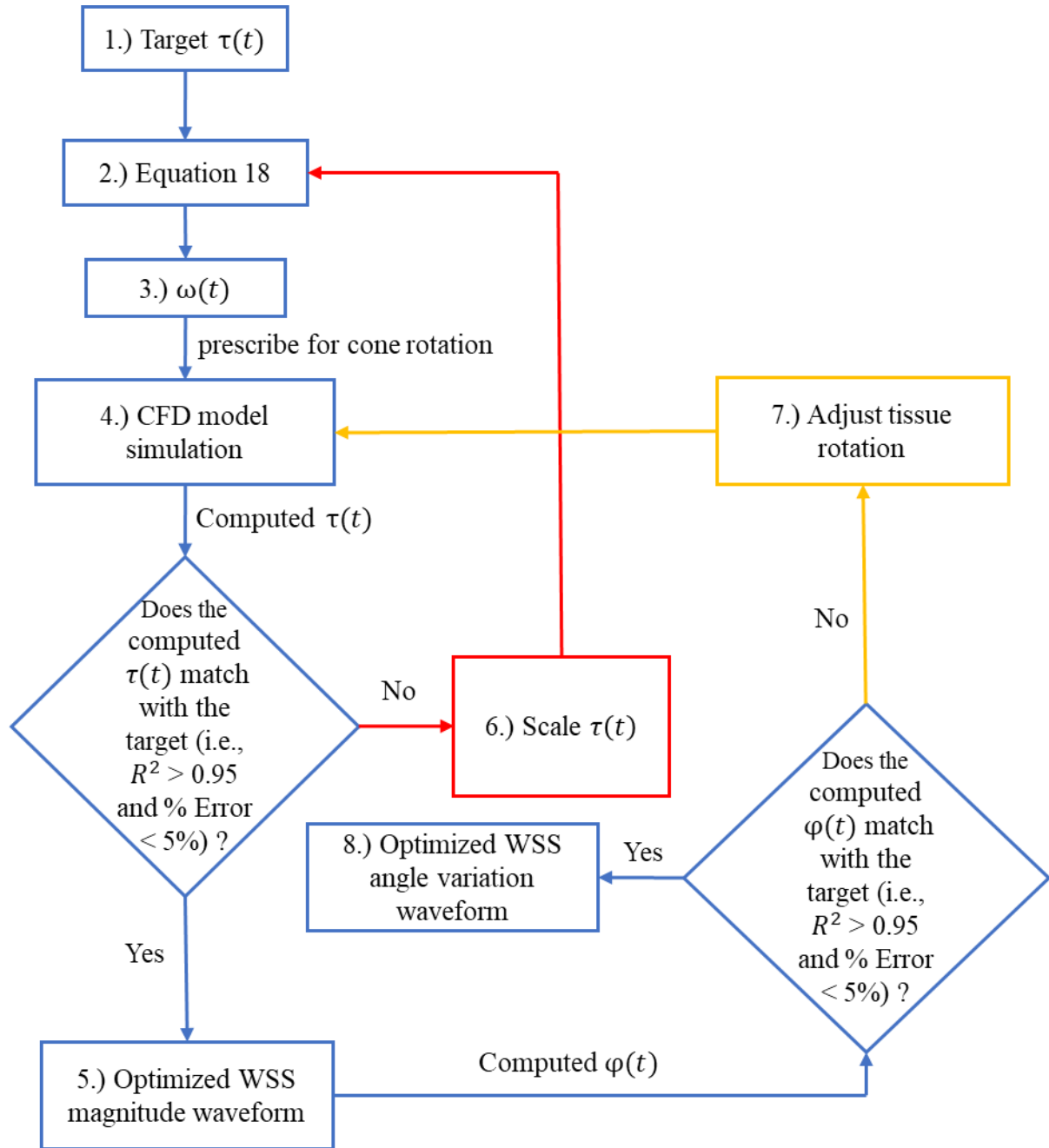


Figure 31. Operating condition strategy flowchart. Blue lines represent the general process, red lines represent the waveform optimization process for WSS magnitude and yellow lines represent WSS angular variation correcting process.

Implementation to LR-BAV AA WSS Generation

In this determination of the operating conditions, the target WSS waveforms were obtained from the proximal convexity AA of the LR-AV aorta FSI model in Specific Aim 1. The target WSS magnitude waveform was converted to the corresponding angular velocity waveform by using Equation 18. Then, this calculated cone angular velocity was prescribed to the cone surface in the CFD model.

Waveform Optimization/ Correcting Process

Three steps were required for optimizing the WSS magnitude waveform. First step was to obtain the scaling factor by taking the ratio of the target and the initial WSS magnitude output at every time point. This scaling factor was then applied back to the initial WSS magnitude input to obtain a scaled input as the second step (Figure 32). Finally, this scaled WSS magnitude input was converted to its corresponding cone angular velocity by using Equation 18, and simulation was performed. These steps were

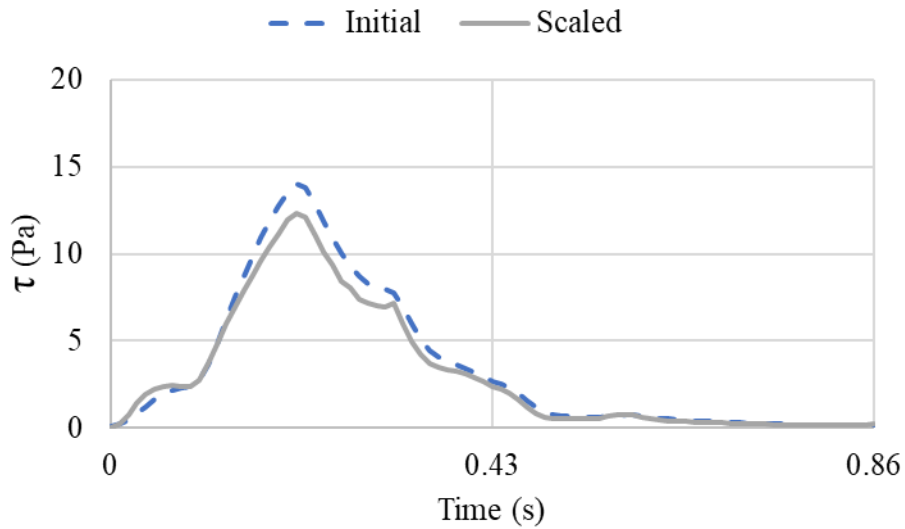


Figure 32. Comparison between the initial WSS magnitude input and the scaled WSS magnitude input

repeated, if necessary, until the % error and R^2 were less than 5.0% and greater than 0.95.

The verification of the WSS angular variation on the tissue was performed after the optimized WSS magnitude input was determined. To calculate the WSS angular deviation, the optimized WSS magnitude output was projected along the tangential axis by performing inner product on the normalized WSS magnitude output and the normalized tangential vector. The definitions of the tangential direction, angular deviation and the WSS vector are as illustrated in Figure 33. Black arrow represents the tangential direction, which is the ideal flow direction generated by the device. Red dash line represents the computed instantaneous WSS vector, which deviates from the ideal direction. The angular deviation, β , was then obtained by taking inverse cosine from the inner product (Figure 34). By adding/ subtracting β from the target, the computed WSS angular variation on the tissue was obtained (Figure 35).

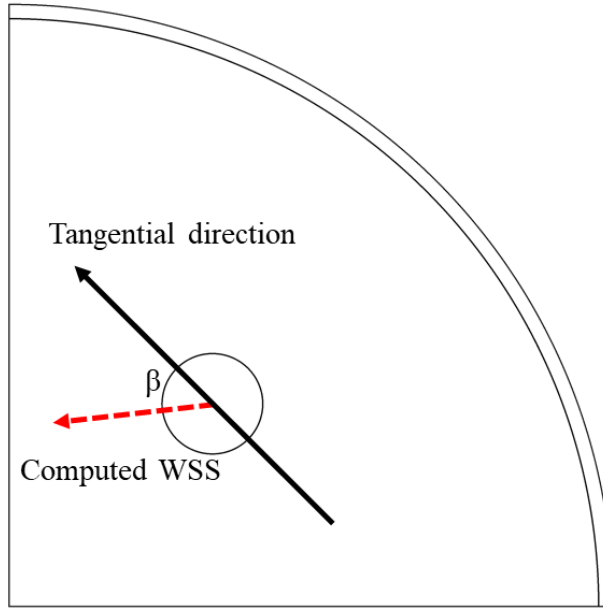


Figure 33. Definition of the tangential direction, angular deviation and computed WSS vector.

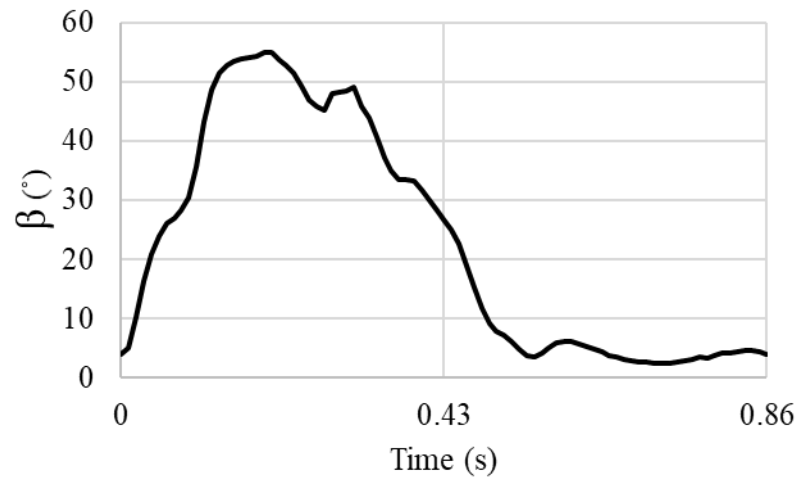


Figure 34. Error in WSS angle at each time point over the entire cardiac cycle.

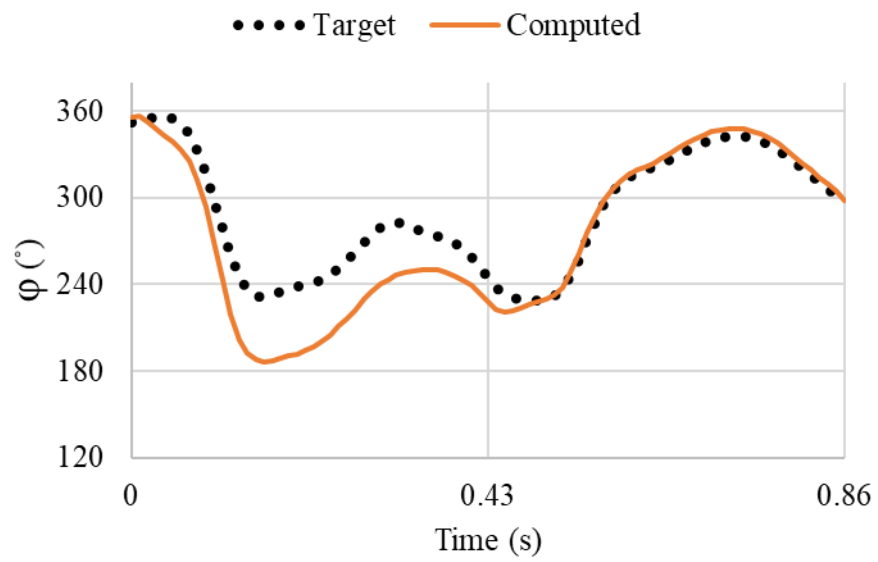


Figure 35. Comparison between the target and computed WSS angular variations.

Before correcting the WSS angular variation waveform, another simulation without prescribing motion to the tissue was performed. The angular deviations observed from both cases were then compared to identify whether it was a result of the tissue rotation. The angular deviations and the computed WSS angular variations were obtained by following the steps described above, and the results are shown in Figure 36 and summarized Table 11.

The results demonstrated that whether tissue is rotating or not, the WSS angular deviations were present, and there are no significant differences between two cases. In other words, the WSS angular deviations was a result of cone rotation. Since that, correction on the WSS angular variation waveform could be made by adjusting the tissue rotation. Once the corrected WSS angular variation waveform was obtained, and the new tissue angular velocity was calculated.

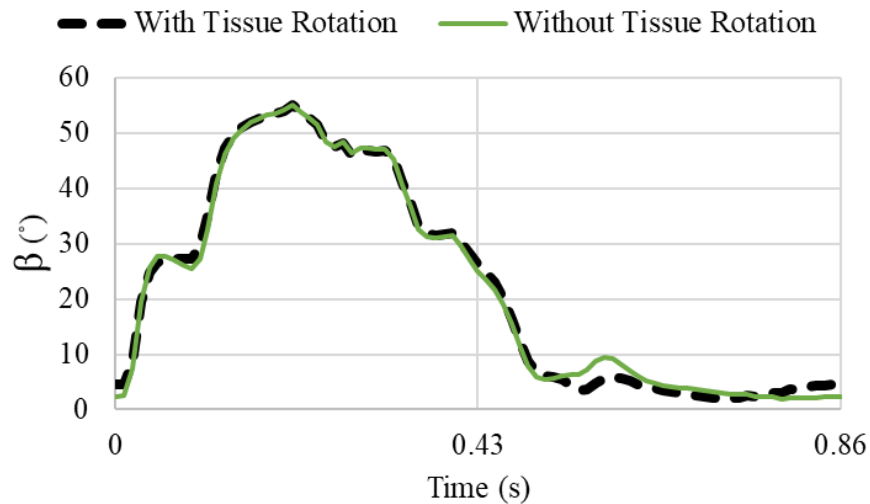


Figure 36. Comparison of WSS angular deviations between two cases: 1.) with tissue rotation and 2.) without tissue rotation.

Table 11. The calculated NRMSD and R^2 values in WSS angular deviations when simulation performed 1.) with tissue rotation and 2.) without tissue rotation

Case Description	NRMSD	R^2
With Tissue Rotation	18.6%	0.921
Without Tissue Rotation	18.5%	0.922

Normalized Root Mean Squared Deviation Calculation

After the simulation with the optimized WSS input was completed, the WSS was extracted from the tissue surface. The resultant WSS was then compared with the target WSS waveform in terms of the NRMSD (Equation 21) and R^2 value.

5.2.3 Torque Calculations for Motor Selections

After the operating condition was determined (i.e., the optimized WSS input waveform), the torque was calculated based on the angular velocity function derived from the optimized waveform. To calculate the torque, the bioreactor was first separated into three sections: the cone side the angled face and the cone itself (Equation 22-24).

$$\text{Torque on the cone side: } T_{\text{cone side}} = \frac{|\nu\omega_c|}{2\pi R_c H_c} \quad (22)$$

$$\text{Torque on the angled side: } T_{\text{angled face}} = \frac{\nu\omega_c \log(R_c)}{\pi} \quad (23)$$

$$\text{Cone acceleration torque: } T_{\text{cone}} = |I\alpha| \quad (24)$$

where ν is the kinematic viscosity ($0.00095 \times 10^{-6} m^2 s^{-1}$), ω_c is the angular velocity, R_c is the radius of the cone, H_c is the height of the cone, I is the total inertia and α is the

cone acceleration. The root mean square of the torque was calculated based on the summation of the torques and the interval at each time step (Equation 25).

Root mean squared total:

$$RMST = \sqrt{\frac{\sum T_{total} \Delta t}{t_{total}}} \quad (25)$$

Similar process was performed for calculating the torque for rotating the tissue mounts. Since there are four tissue mounts rotating simultaneously, the torque was first calculated based on one of them and multiplied by four at the end (Equation 26).

Torque on the tissue mounts:

$$T_{tissue\ mount} = \frac{4v\omega_{tissue} \log(R_{tissue})}{\pi} \quad (26)$$

5.3 Results

5.3.1 Mesh Dependency Test

The WSS and the torque extracted from the tissue were compared in each model as the number of the cell cross the gap increases. A decreasing trend from four to eight cells across the gap was observed in each model for both WSS and torque data (Figure 37 and Figure 38).

In Model 1, the percent difference in WSS on the tissue was 5.81% with four cells across the gap (vs. three cells across the gap) and it immediately reduced to 3.06% in the next mesh setup (i.e., five cells across the gap). On the other hand, the percent difference in torque was 12.4 % at the beginning and did not converge (i.e., less than 5%) until the number of cell across the gap was increased to six. Since both data do not change

dramatically after the cells number reaches six, this setting became the finalized mesh setup for Model 1.

Similarly, the rest of the models show decreasing trend on both data as the number of the cells approaches to six. Therefore, six cells across the gap were applied to all the model, and used as the finalized mesh setup.

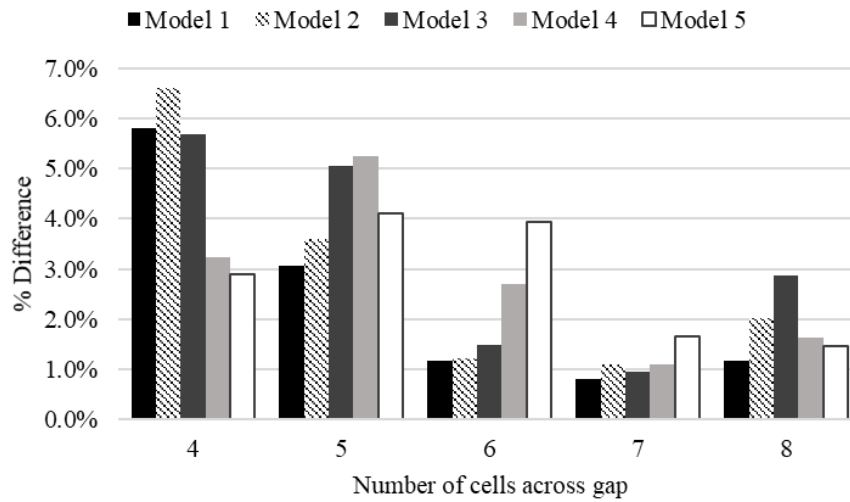


Figure 37. Percent differences between current and successive mesh setup in WSS magnitude on the tissue surface for each model.

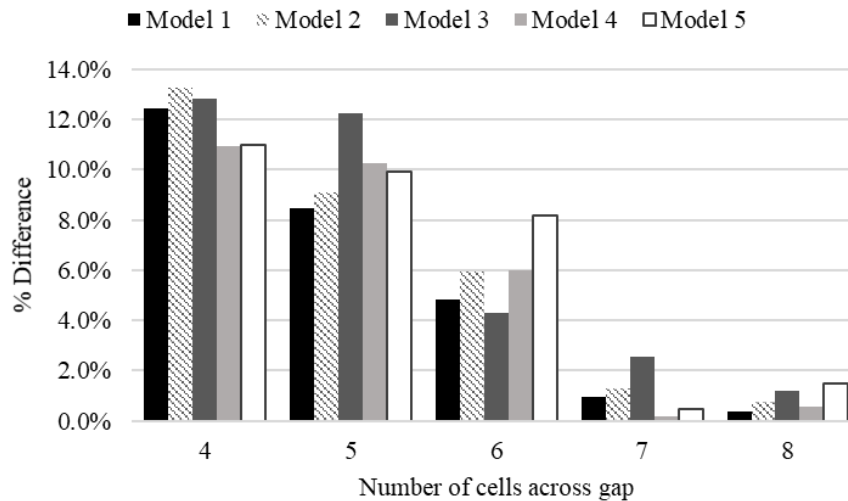


Figure 38. Percent differences between current and successive mesh setup in torque on the tissue for each model

Mesh Properties

Mesh properties for each bioreactor model are reported in Table 12. These values were obtained when the number of cell across the gap is equal to six. The aspect ratio is a measure of the stretching of the cell. Ideal aspect ratio is when the value equals to 1. Skewness is the evaluation of the shape of the cell, and it ranges from 0 to 1. The smaller the value is means the better the cell quality is. The orthogonal quality and the overall element quality were also analyzed, and they both range from 0 to 1 as well. However, the larger the value is means the better the cell quality is.

Table 12. Mesh properties (n=6) for each bioreactor models

	Model 1	Model 2	Model 3	Model 4	Model 5
Aspect Ratio	1.8394	1.8377	1.8367	1.8382	1.8387
Skewness	0.2195	0.2193	0.2194	0.2197	0.2201
Orthogonal Quality	0.7789	0.7791	0.7790	0.7790	0.7783
Element Quality	0.8412	0.8416	0.8417	0.8414	0.8412
Number of Elements	9,371,027	11,025,837	13,646,156	13,564,437	17,414,200

5.3.2 Finalized Dimensions

The calculated results for NRMSD and R^2 in terms of WSS magnitude and angular variation are listed in Table 13 and Table 15, respectively. The lower the NRMSD and the greater the R^2 are obtained mean the closer the computed results are to the target WSS. Based on the WSS magnitude results, increasing the radius of the bioreactor and the tissue location by 20% and 50% did not show significant improvement as compared with the original model. Increasing the radius of the bioreactor by 50% and 100% and keeping the tissue at its original location yielded similar results as compared to

the original model; however, it did not significantly improve the % error.

The angular variation of the computed WSS on tissue surface was also examined for each model. Based on the WSS angular variation results, Model 2 and 3 yielded similar results in NRMSD and R^2 values. The NRMSD calculated from Model 4 and 5 were slightly greater than Model 1; however, the differences were not significant. In other words, none of the models was able to demonstrate an improved WSS angular variation results as compared to Model 1.

Since Model 1 generated the least NRMSD and the greatest R^2 values in WSS magnitude, and no significant differences were found in WSS angular variations, dimensions of the bioreactor were finalized based on Model 1.

Table 13. The calculated NRMSD and R^2 values in WSS magnitude for each model

Model No.	Description	NRMSD	R^2
1	Original	5.66%	0.997
2	20%	6.59%	0.994
3	50%	8.66%	0.983
4	50%, original tissue location	5.77%	0.997
5	100%, original tissue location	6.43%	0.996

Table 14. The calculated NRMSD and R^2 values in WSS angular variations for each model

Model No.	Description	NRMSD	R^2
1	Original	19.1%	0.920
2	20%	19.0%	0.922
3	50%	19.1%	0.923
4	50%, original tissue location	19.6%	0.920
5	100%, original tissue location	19.8%	0.920

5.3.3 Optimized WSS Waveform

The scaled (optimized) WSS magnitude input shown in Figure 32 from section 5.2.2 produced a WSS output as shown in Figure 39. To quantitatively assess the improvement, NRMSD and R^2 were calculated, and the results show significant differences (NRMSD: decreased from 5.66% to 1.16%; R^2 increased from 0.997 to 0.998, respectively.)

The computed WSS angular variations shown in Figure 35 yielded a NRMSD and R^2 value at 19.1% and 0.920, respectively. By adjusting the tissue rotation according to scaled angular variation waveform shown in Figure 40, the results were improved to 1.1% and 0.999 for NRMSD and R^2 , respectively. This demonstrates that the bioreactor is capable of replicating the desired WSS environment in term of the magnitude and directionality.

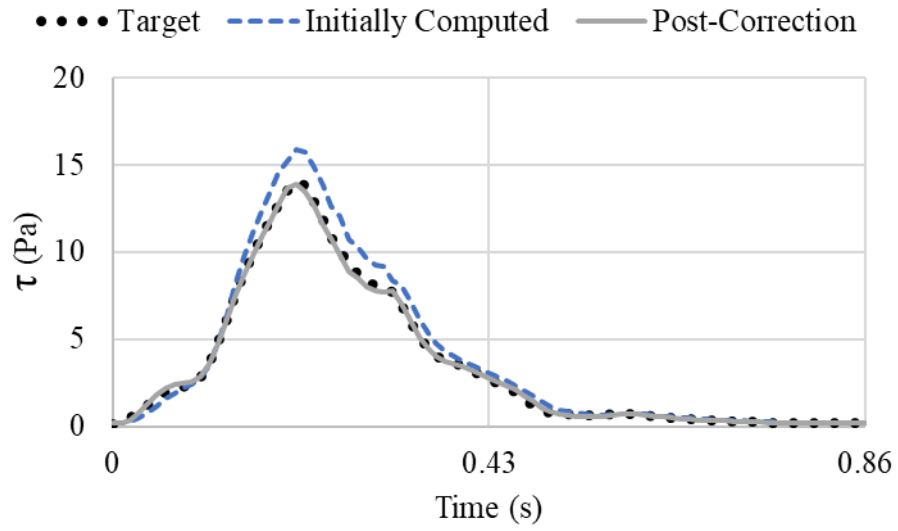


Figure 39. Comparisons between target, the initial and the optimized (post-correction) WSS magnitude

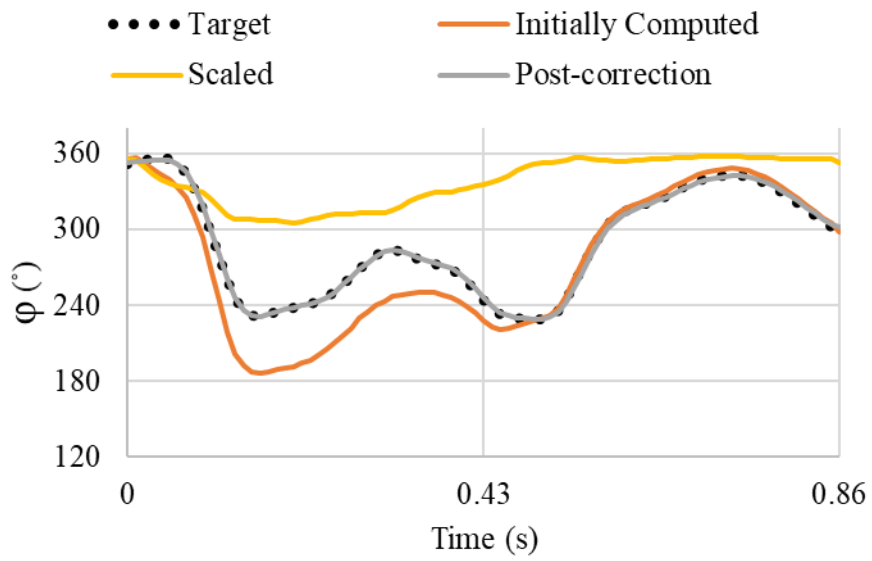


Figure 40. Comparisons between target, initial, scaled and optimized (post-correction) WSS angle waveform

5.3.4 Servo/Motor Selection

After the operating conditions were determined, the torque required to perform the rotation of such waveform and its RMST were calculated. The selection of the motors was then based on the RMST, the average rotating speed, the maximum rotating speed and the peak torque, and the values were summarized in Table 15.

To select motors which are capable of performing this kind of rotation, the stall torque, the rated speed, the maximum speed and the peak torque of the motor need to match/ be greater than the calculated RMST, average rotating speed, maximum rotating speed and peak torque, respectively. By comparing the motor specification from Parker-Hannifin Corp., PM-FALR5AM8 were selected for the cone rotation and tissue mount rotation, respectively.

Table 15. Motor specifications requirement for cone and tissue mount rotations

<u>Cone Motor Specs</u>		
Average Speed	583.3	RPM
Max Speed	2323.6	RPM
Peak Torque	0.000315	Nm
RMST	0.0092	Nm
<u>Tissue Mount Motor Specs</u>		
Average Speed	-1.2	RPM
Max Speed	62.8	RPM
Peak Torque	4.1E-06	Nm
RMST	0.00085	Nm

5.4 Summary

In Specific Aim 3, bioreactor CFD models with five different dimensions were created. The WSS magnitude and directionality waveforms at the proximal convexity of TAV AA obtained from Specific Aim 1 were considered as target, and they were programmed for the cone and tissue rotations, respectively, for the simulation. The predicted WSS from each model was compared with the target by calculating the NRMSD and R^2 . Based on the results, Model 1, the bioreactor with original dimensions, was selected.

The operating conditions for the original bioreactor was determined through the waveform optimization process, and an optimized WSS input was generated. By prescribing corresponding angular velocity of this optimized WSS input to the cone, the WSS output was improved from 5.66% and 0.997 to 1.16% and 0.998 for the NRMSD and R^2 , respectively.

Torque requirements were calculated based on the optimized WSS input and the tissues rotation angular velocity. PM-FALR5AM8 (Parker-Hannifin Corp., Cleveland, OH) was selected for the cone rotation and tissue mount rotation, respectively.

CHAPTER 6:

SUMMARY

The objectives of this thesis were to quantify the multidirectional characteristics of the WSS caused by BAVs in the AA and to design a device capable of subjecting native aortic tissue to native BAV WSS magnitude and directionality. The results from Specific Aim 1 demonstrated that BAVs not only generated elevated WSS magnitude in the convexity of the proximal AA, those elevated WSS also oriented within a wider range of angles as compared with TAV. A novel multidirectional fluid shear stress bioreactor was then designed based on the principle of a cone-and-plate viscometer to subject aortic tissue to TAV/ BAV multidirectional WSS environment. Rotating tissue mounts were adapted into the design to achieve the desired WSS directionality, and the WSS magnitude was achieved by rotating the cone. Bioreactor dimension analyses were performed, and the operating conditions were determined through ANSYS CFX. CAD drawings of the bioreactor were created, and the servo/ motors were selected based on the results from the CFD analysis.

CHAPTER 7:

DISCUSSION

7.1 Novelty of the Study

WSS Characterization

In this thesis, the multidirectional characteristics of the WSS in the AA caused by BAVs were quantified, and the assessment was done computationally through valve-aorta FSI models [43]. The WSS multidirectionality was quantified in terms of TSM, OSI and transWSS. TSM and OSI were evaluated in global, and in both longitudinal and circumferential directions. Although previous PC-MRI research has also studied the WSS characteristics [13], [39], [41], [70], [75], some limitations existed. For instance, the recruited samples sometimes involve aortic stenosis, aortic insufficiency, pre-existed aortic dilation, aortic aneurysm and other factors which might have influences on the flow characteristics [37], [41], [67]. Another limitation is the method which was used to extract and analyze the data. Sometimes, the WSS data were extracted and averaged along the entire lumen of the AA. The WSS at the convexity and the concavity, which could be very different, were not distinguished [39], [75].

The first novelty of the study is the valve-aorta FSI models used in this thesis which include four different aortic valve morphotypes, and they were connected to non-dilated AA with same dimensions. In this way, morphotype-dependent WSS characteristics, if any, would be identified. Other factors (i.e., age, pre-existed aortic

dilation, aortic stenosis, etc.), which might affect the flow and WSS characteristics, thus were excluded. Furthermore, the data were extracted and analyzed separately at the proximal convexity and concavity of the AA in this thesis.

Although previous research has studied the helical flow pattern observed in the BAV AA through quantifying the longitudinal and circumferential components, to the best of authors knowledge, the multidirectionality of WSS was never quantified. The second novelty of the study is the method proposed in Section 3.2.4. By using this method, the angle distribution of the elevated WSS could be identified. WSS multidirectinoality was demonstrated at the proximal convexity of all BAV aortas.

Multidirectional Fluid Shear Stress Bioreactor

The bioreactor designed in this thesis is able to subject time-dependent multidirectional WSS to samples. To the best of author's knowledge, this is the first time a fluid shear stress bioreactor capable of replicating both time-varying WSS magnitude and directionality introduced. As the interests in the effects of WSS directionality on cardiovascular diseases (e.g., atherosclerosis, valvular diseases, aortopathy, etc.) have risen, this design will be beneficial for elucidating the cause-and-effect relationship between the WSS magnitude/ directionality and the relevant cardiovascular diseases.

7.2 WSS Characteristics in TAV/ BAVs Proximal AA

WSS Magnitude

In the proximal AA, all BAVs generated shear stress overload at the convexity, with much of the dominant force occurring in the circumferential direction, and

underload at the concavity as compared with TAV. This matched previous clinical findings [75] and corresponded the asymmetric aortic dilation pattern found in BAV patients [27], [54]. The varying magnitude of WSS are always morphotype-dependent, and were shown to vary widely depending upon location. Among all BAV models, LR-BAV generated the most severe time-averaged WSS overload at the convexity, and the circumferential component was dominant in all BAV models. Previous clinical research found that the aortic dilation in patients with LR-BAV morphotype is asymmetric and prone to occur at the root and convexity of the AA, which were also the regions where the highest WSS overload was observed in LR-BAV aorta model.

WSS Directionality

In the proximal convexity, TAV had the highest LOSI among all the models, and the COSI were almost zero at the convexity for all the models. In the proximal concavity, high LOSI were observed in all the models, as compared to the convexity in which high COSI were also observed except for the TAV morphotype. Since the longitudinal TSM was the dominant component at both convexity and concavity of the TAV AA plus high LOSI and low COSI, this implied that TAV generated unidirectional flow at both regions. In contrast, the circumferential TSM was the dominant component at the convexity of all BAV AAs, and all BAVs exhibited almost zero COSI and non-zero LOSI. This implied that although the flow seemed to be unidirectional along the circumferential direction. Based off of this data, it could be assumed that the right-handed helical structure of the flow is consistently maintained throughout the entire cardiac cycle, with slight flow alterations in the longitudinal direction. Endothelial cells within this region, which

experienced lower quantities of WSS and pulsatile flow with reversal in a normal TAV morphotype, were now subjected to overloads within a relatively large range of angular change. Since the flow was more complicated in BAV AAs as compared to TAV AA, and the direction of the flow cannot be assessed simply by evaluating the OSI values.

To better evaluate the correlation between the WSS multidirectionality and aortic dilation, other data must be considered. Based on the polar plots results, all BAV demonstrate wider angle coverage with elevated WSS. Among all BAVs, RN-BAV has the maximum WSS magnitude value, as well as threshold angular variation. This matches the findings suggested in the previous research, where severe flow abnormalities were observed in the AA of patients with this morphotype. Furthermore, patients presenting a RN-BAV have been associated with a higher risk of obtaining aortic dilation [39].

TransWSS is the other index that was used to quantify the WSS multidirectionality in this thesis. It was quantified based on both the magnitude and angular deviation from the reference axis over a period of time. TransWSS can range from 0 to its total TSM. The closer the value to the total TSM means the flow is more multidirectional. Based on the results at the convexity in Figure 20, it showed that multidirectional WSS was only presented in the TAV AA. This did not match our findings from the polar plots, because this kind of quantification was case-dependent. Instead of quantifying the WSS multidirectionality case by case, assessing it by making the comparison based on one, normal case (i.e., TAV) will better identify the WSS abnormalities in BAV cases.

7.3 WSS Angular Deviation from the Circumferential Direction Computed on Tissue

Ideally, the shear stress on the tissue surface generated by the cone rotation is in the circumferential direction. Based on the results from Specific Aim 3, angular deviation was detected from the WSS exerted on the tissue. The discrepancy was observed during systolic phase where the cone angular velocity reached its maximum value. This suggested that the high rotating speed of the cone caused secondary flow effects in the device. Theoretically, increasing the distance of the bioreactor wall from the center should mitigate the secondary flow effects caused by the wall. However, based on the results from Model 4 and 5 in Specific Aim 3, increasing the distance of the wall by 50% and 100% did not improve the WSS orientation results.

To solve the problem of WSS angular deviation, two solutions were proposed. The first solution is to reduce the cone angular velocity, if possible, to ensure the flow is laminar and in the circumferential (i.e., keep $Re < 1$). The second solution is taken from the advantage of the rotating tissue mount. If the angular velocity prescribed for the cone motion cannot be reduced, adjusting the tissue orientation and ensuring the tissue alignment in the direction of the computed WSS will solve the problem.

7.4 Limitations of the Study

Although the design was verified to be capable of replicating the WSS magnitude and directionality, limitation existed in the maximum allowable angular velocity programmed for the cone rotation. As mentioned earlier, the Reynolds number must be maintained at a very low value (i.e., $Re < 1$) in order to keep the flow laminar in the circumferential direction. The Reynolds number calculation for this device showed that

the value increases as the cone angular velocity increases, and secondary flow effects occurred. Based on the bioreactor dimensions and the fluid used in this study, the maximum cone angular velocity allowed in order to have a laminar flow in the circumferential direction was 89.97 rad/s. In other words, when the operating condition for the cone rotation is below 89.97 rad/s., the fluid environment is considered as ideal. If not, adjustments either on the cone or the tissue rotation will be required.

7.5 Clinical Implication

According to the discussion in the previous subsections, two key findings were reported. First, WSS overload occurs at the convexity in all BAV models, and the most unfavorable overload was found in the LR-BAV aorta model. Second, lower LOSI were presented at the convexity of the BAV aorta models as compared with the TAV aorta model, and low COSI presented at the convexity of the BAV aorta models relative to its concavity. Furthermore, the WSS angle distribution of the elevated WSS at the convexity is significant greater in all BAV AAs than TAV AA. Assessing the flow direction through the values of LOSI and COSI alone did not provide a complete analysis, since OSI does not account for WSS magnitude. Instead, to assess the changes in the flow direction, one should first identify the elevated WSS magnitude and then quantify its corresponding angle distribution.

7.6 Future Work

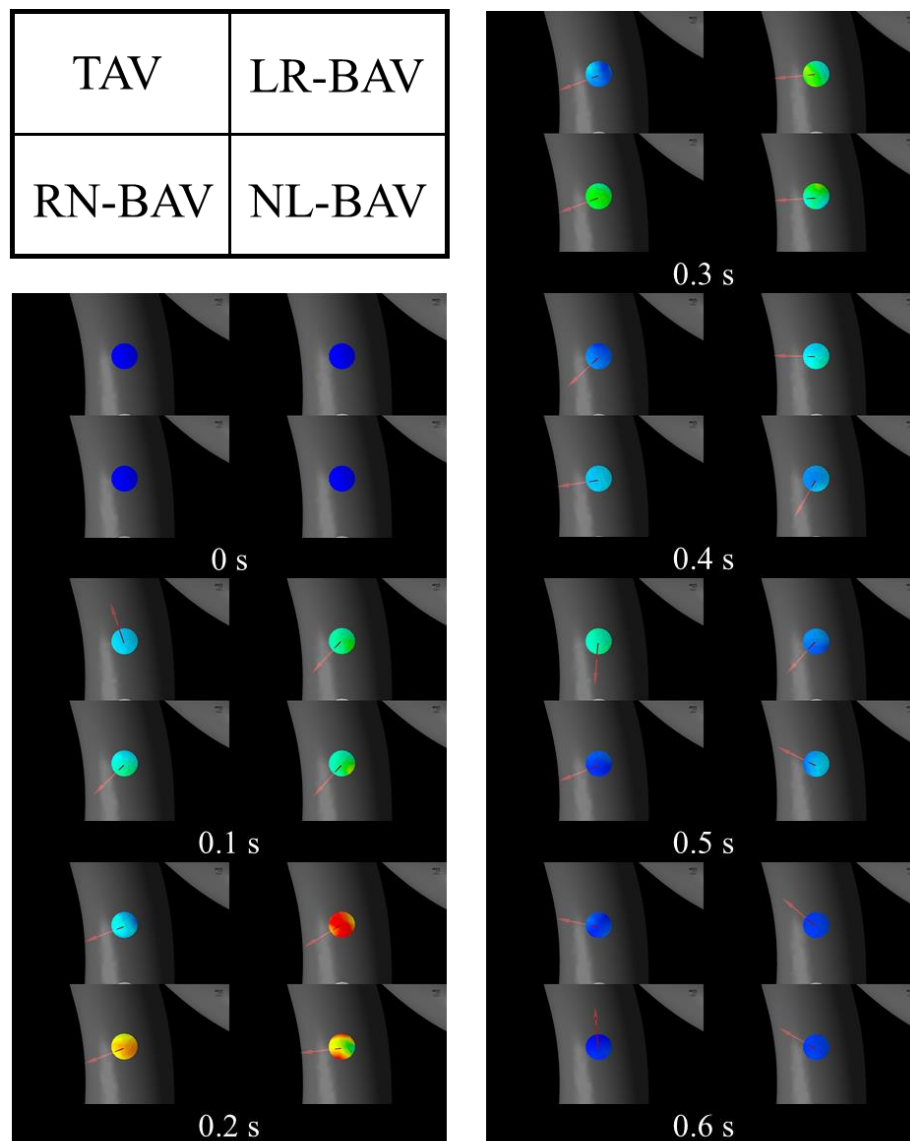
In this thesis, the CAD drawings were created, the operating conditions were

determined, and the design was verified through CFD. The next step is to physically fabricate the bioreactor and perform biological validation. After these are completed, the bioreactor will be utilized in testing the hemodynamic theory of BAV aortopathy *in vitro* and provide new insights into the aortic wall response to native BAV flow abnormalities.

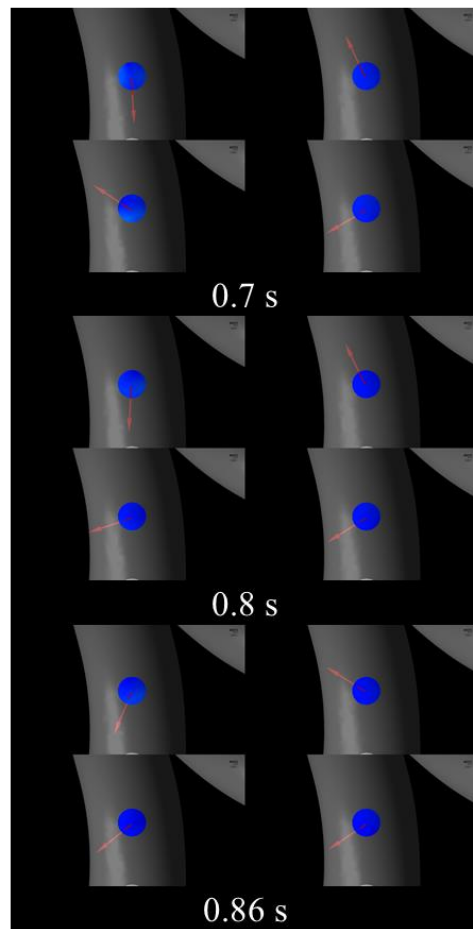
Once the existence of the cause-and-effect relationships between native BAV hemodynamics and aortic medial degeneration is demonstrated, the bioreactor will guide the development of more effective therapeutic strategies for BAV aortopathy based on flow normalization or pharmacological blocking of the flow-mediated biology.

APPENDIX A: Time-varying WSS Vector in the Convexity of Proximal AA for All Valve-aorta Models

Animation of the time-varying WSS vector was also provided as online supplementary material.



TAV	LR-BAV
RN-BAV	NL-BAV

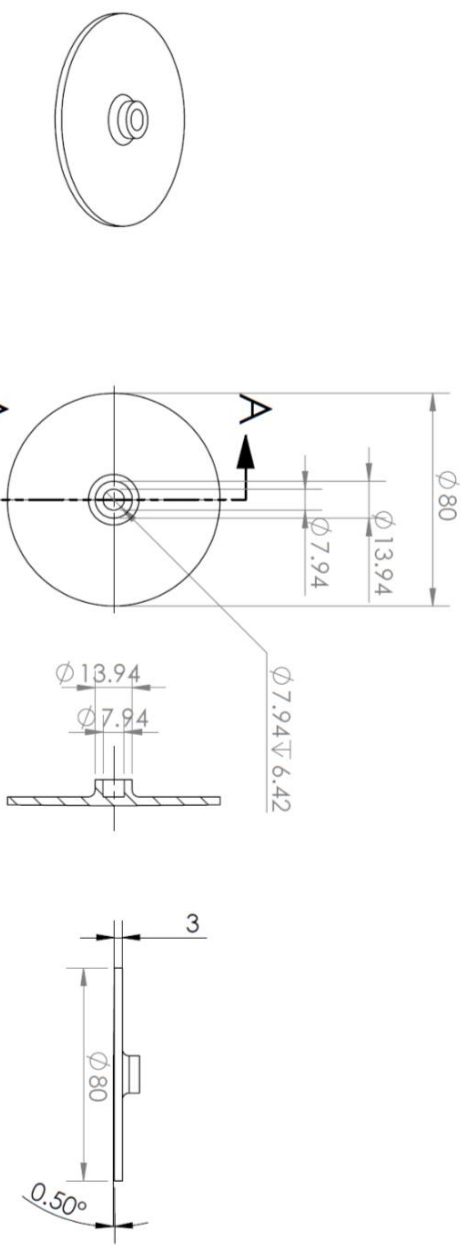


APPENDIX B: CAD Drawings of Each Bioreactor Part

The CAD drawings of each bioreactor part are shown in the following pages.

2

1



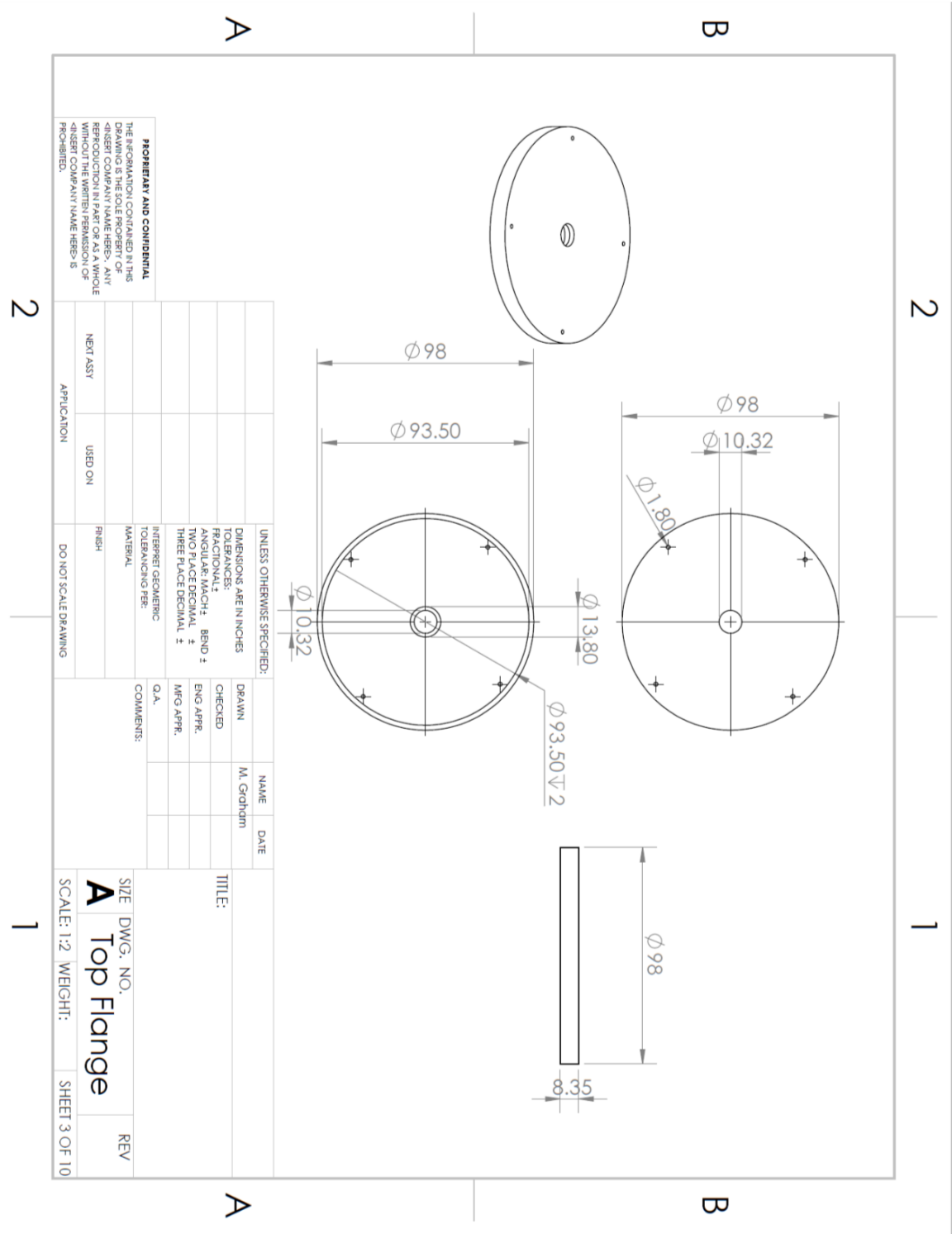
SECTION A-A

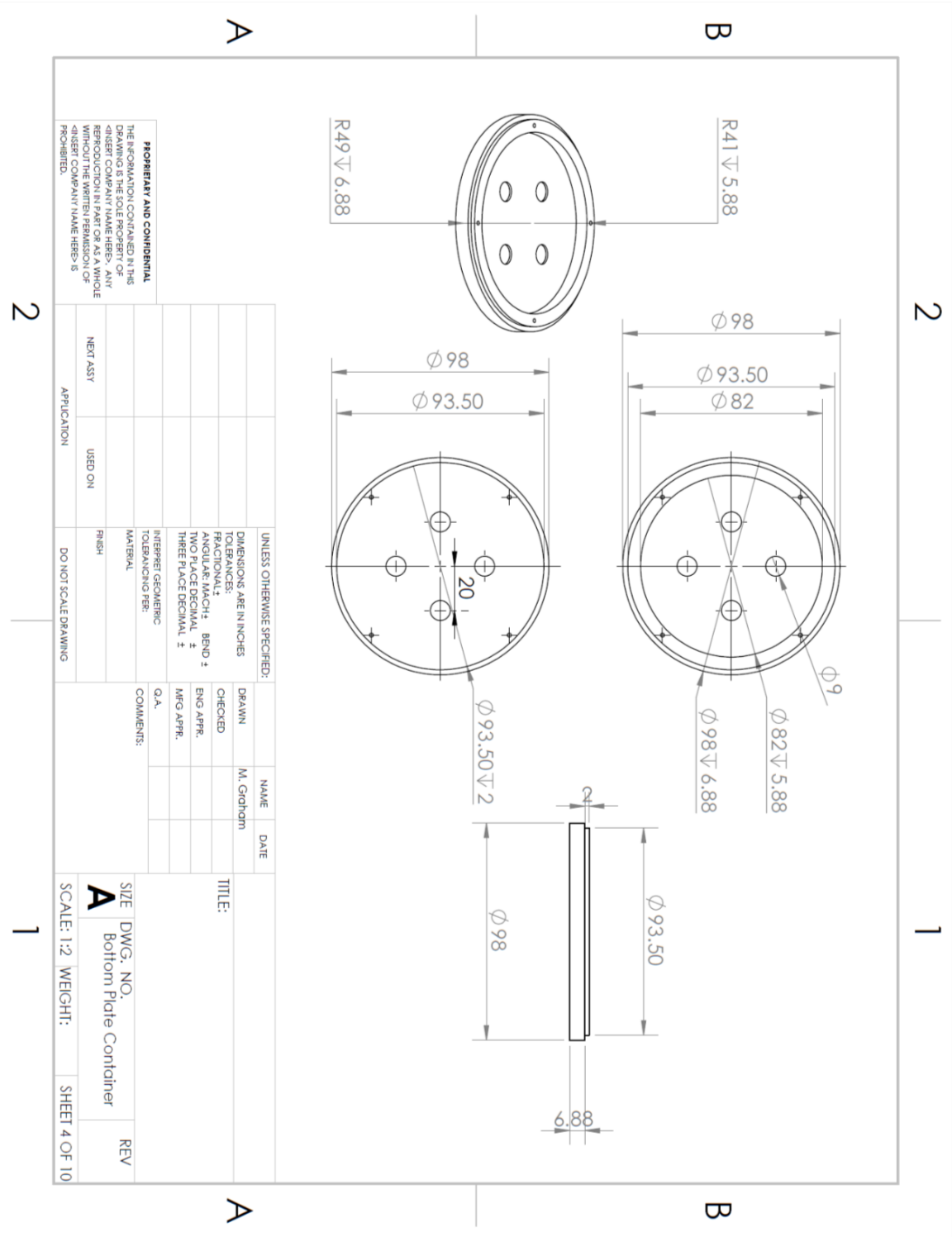
UNLESS OTHERWISE SPECIFIED:				DRAWN		NAME		DATE		TITLE:	
DIMENSIONS ARE IN mm				M. Gohom							
TOLERANCES:				CHECKED							
FRACTIONAL: ±				ENG APPR.							
ANGULAR: MACH ±				MFG APPR.							
TWO PLACE DECIMAL ±											
THREE PLACE DECIMAL ±											
INTERPRET GEOMETRIC TOLERANCING PER:				COMMENTS:							
MATERIAL:											
FINISH:											
NEXT ASSY											
USED ON											
APPLICATION											
DO NOT SCALE DRAWING											

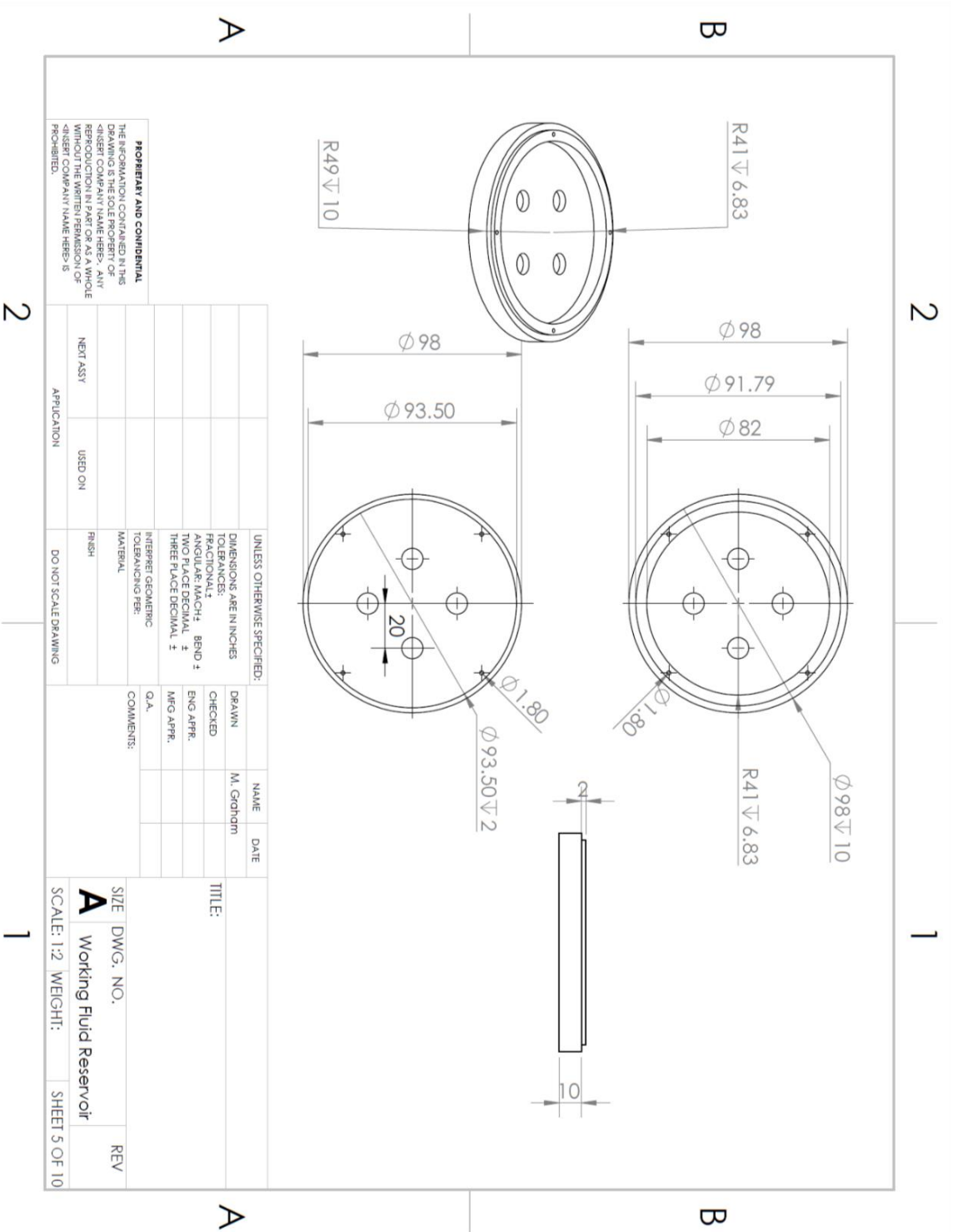
SIZE DWG. NO. REV
A Top Cone

SCALE: 1:2 WEIGHT: SHEET 1 OF 10

PROPRIETARY AND CONFIDENTIAL
THE INFORMATION CONTAINED IN THIS DRAWING IS THE SOLE PROPERTY OF GUSSET COMPANY NAME HERE. ANY REPRODUCTION IN PART OR AS A WHOLE WITHOUT THE WRITTEN PERMISSION OF GUSSET COMPANY NAME HERE IS PROHIBITED.

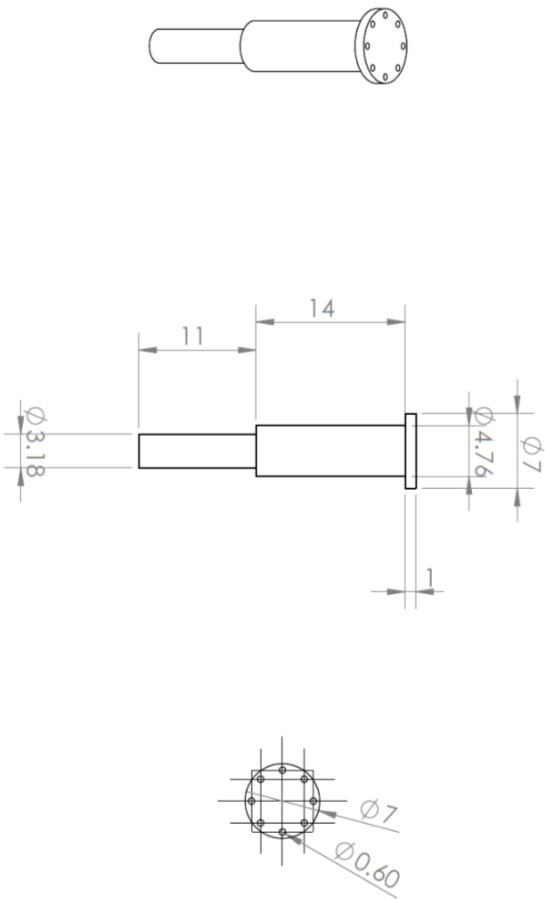






2

1



B

B

A


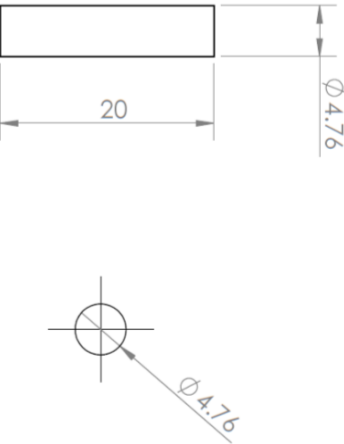

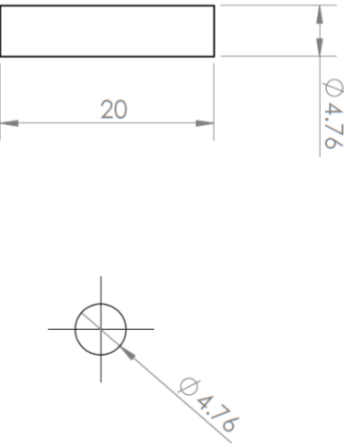
A

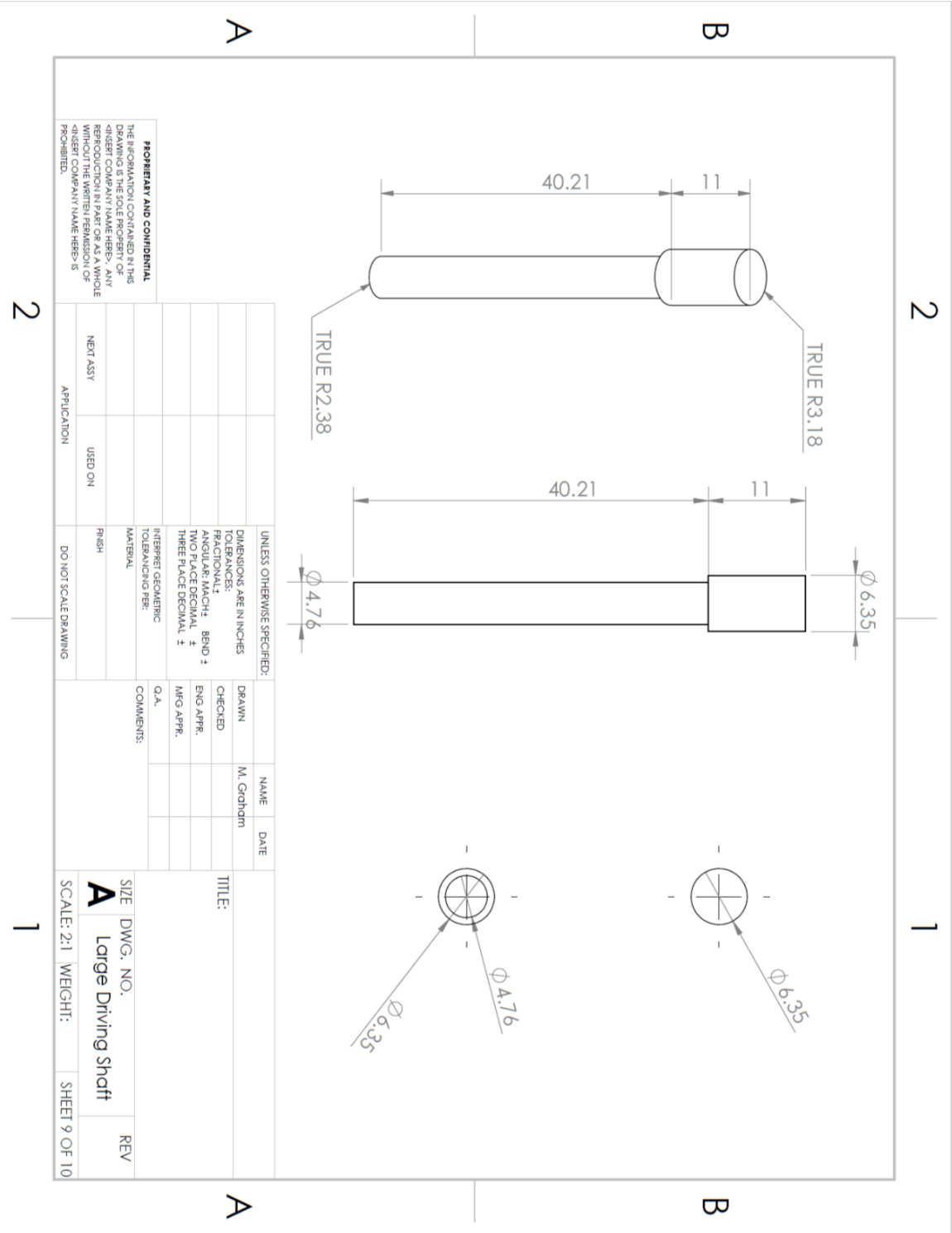
		UNLESS OTHERWISE SPECIFIED:			
		DIMENSIONS ARE IN INCHES		DRAWN	
		TOLERANCES:		M. Gidham	
		FRACTIONAL: \pm		CHECKED	
		ANGULAR: MACH: BEND \pm		ENG APPR.	
		TWO PLACE DECIMAL \pm		MFG APPR.	
		THREE PLACE DECIMAL \pm			
		INTERPRET GEOMETRIC TOLERANCING PER:		Q.A.	
		MATERIAL		COMMENTS:	
		FINISH			
NEXT ASSY		USED ON			
APPLICATION		DO NOT SCALE DRAWING			
		TITLE:		SIZE DWG. NO.	
				Tissue Mount	
				REV	
				SCALE: 2:1 WEIGHT: SHEET 6 OF 10	

PROPERTY AND CONFIDENTIAL
THE INFORMATION CONTAINED IN THIS
DRAWING IS THE SOLE PROPERTY OF
<INSERT COMPANY NAME HERE>. ANY
REPRODUCTION IN PART OR AS A WHOLE
WITHOUT THE WRITTEN PERMISSION OF
<INSERT COMPANY NAME HERE> IS
PROHIBITED.

2

1

2		1																									
B		B																									
A		A																									
																											
<p>PROPRIETARY AND CONFIDENTIAL THE INFORMATION CONTAINED IN THIS DRAWING IS THE SOLE PROPERTY OF <INSERT COMPANY NAME HERE>. ANY REPRODUCTION IN PART OR AS A WHOLE WITHOUT THE WRITTEN PERMISSION OF <INSERT COMPANY NAME HERE> IS PROHIBITED.</p>																											
2		1																									
B		B																									
A		A																									
																											
<p>UNLESS OTHERWISE SPECIFIED:</p> <table><tr><td>DIMENSIONS ARE IN INCHES</td><td>DRAWN</td><td>NAME</td><td>DATE</td></tr><tr><td>TOLERANCES:</td><td>CHECKED</td><td>M. Groom</td><td></td></tr><tr><td>FRACTIONAL: ±</td><td>END APPR.</td><td></td><td></td></tr><tr><td>ANGULAR: MACH ±</td><td>MFG APPR.</td><td></td><td></td></tr><tr><td>TWO PLACE DECIMAL ±</td><td></td><td></td><td></td></tr><tr><td>THREE PLACE DECIMAL ±</td><td></td><td></td><td></td></tr></table> <p>INTERPRET GEOMETRIC TOLERANCING PER: Q.A. COMMENTS:</p> <p>MATERIAL: FINISH: DO NOT SCALE DRAWING</p> <p>NEXT ASSY USED ON APPLICATION</p> <p>SIZE DWG. NO. REV A Small Driving Shaft SCALE: 2:1 WEIGHT: SHEET 8 OF 10</p>				DIMENSIONS ARE IN INCHES	DRAWN	NAME	DATE	TOLERANCES:	CHECKED	M. Groom		FRACTIONAL: ±	END APPR.			ANGULAR: MACH ±	MFG APPR.			TWO PLACE DECIMAL ±				THREE PLACE DECIMAL ±			
DIMENSIONS ARE IN INCHES	DRAWN	NAME	DATE																								
TOLERANCES:	CHECKED	M. Groom																									
FRACTIONAL: ±	END APPR.																										
ANGULAR: MACH ±	MFG APPR.																										
TWO PLACE DECIMAL ±																											
THREE PLACE DECIMAL ±																											



REFERENCES

- [1] “The Aorta — Genetic Aortic Disorders Association Canada.” [Online]. Available: <http://www.gadacanada.ca/the-aorta/>. [Accessed: 24-Jan-2018].
- [2] A.Wolak, H.Gransar, L. E. J.Thomson, J. D.Friedman, R.Hachamovitch, A.Gutstein, L. J.Shaw, D.Polk, N. D.Wong, R.Saouaf, S. W.Hayes, A.Rozanski, P. J.Slomka, G.Germano, andD. S.Berman, “Aortic Size Assessment by Noncontrast Cardiac Computed Tomography: Normal Limits by Age, Gender, and Body Surface Area,” *JACC Cardiovasc. Imaging*, vol. 1, no. 2, pp. 200–209, 2008.
- [3] M.Bäck, T. C.Gasser, J.-B.Michel, andG.Caligiuri, “Biomechanical factors in the biology of aortic wall and aortic valve diseases,” *Cardiovasc. Res.*, vol. 99, no. 2, pp. 232–241, Jul.2013.
- [4] T. M.Tadros, M. D.Klein, andO. M. O. M.Shapira, “Ascending aortic dilatation associated with bicuspid aortic valve. Pathophysiology, molecular biology, and clinical implications,” *Circulation*, vol. 119, no. 6, pp. 880–890, Feb.2009.
- [5] H.-H.Sievers andC.Schmidtke, “A classification system for the bicuspid aortic valve from 304 surgical specimens.,” *J. Thorac. Cardiovasc. Surg.*, vol. 133, no. 5, pp. 1226–33, May2007.
- [6] D. P.Nathan, C.Xu, T.Plappert, B.Desjardins, J. H.Gorman, J. E.Bavaria, R. C.Gorman, K. B.Chandran, B. M.Jackson, andB. M.Jackson, “Increased ascending aortic wall stress in patients with bicuspid aortic valves.,” *Ann. Thorac. Surg.*, vol. 92, no. 4, pp. 1384–9, Oct.2011.

- [7] M. N.Levy, "Circulation Research," *Circ. Res.*, vol. XIII, no. 2, pp. 437–445, 1971.
- [8] C.Seaman, A.George Akingba, andP.Sucosky, "Steady Flow Hemodynamic and Energy Loss Measurements in Normal and Simulated Calcified Tricuspid and Bicuspid Aortic Valves," *J. Biomech. Eng.*, vol. 136, no. 4, p. 41001, Mar.2014.
- [9] N.Saikrishnan, C.-H.Yap, N. C.Milligan, N.V.Vasilyev, andA. P.Yoganathan, "In Vitro Characterization of Bicuspid Aortic Valve Hemodynamics Using Particle Image Velocimetry," *Ann. Biomed. Eng.*, vol. 40, no. 8, pp. 1760–1775, Aug.2012.
- [10] M. D.Hope, A. K.Meadows, T. A.Hope, K. G.Ordoas, G. P.Reddy, M. T.Alley, andC. B.Higgins, "Images in cardiovascular medicine. Evaluation of bicuspid aortic valve and aortic coarctation with 4D flow magnetic resonance imaging.," *Circulation*, vol. 117, no. 21, pp. 2818–9, May2008.
- [11] M. M.Bissell, A. T.Hess, L.Biasioli, S. J.Glaze, M.Loudon, A.Pitcher, A.Davis, B.Prendergast, M.Markl, A. J.Barker, S.Neubauer, andS. G.Myerson, "Aortic dilation in bicuspid aortic valve disease: flow pattern is a major contributor and differs with valve fusion type.," *Circ. Cardiovasc. Imaging*, vol. 6, no. 4, pp. 499–507, Jul.2013.
- [12] M.Bauer, H.Siniawski, M.Pasic, B.Schaumann, andR.Hetzer, "Different hemodynamic stress of the ascending aorta wall in patients with bicuspid and tricuspid aortic valve," *J. Card. Surg.*, vol. 21, no. 3, pp. 218–220, May2006.
- [13] A. J.Barker, C.Lanning, andR.Shandas, "Quantification of hemodynamic wall shear stress in patients with bicuspid aortic valve using phase-contrast MRI," *Ann. Biomed. Eng.*, vol. 38, no. 3, pp. 788–800, Mar.2010.

- [14] E.Faggiano, L.Antiga, G.Puppini, A.Quarteroni, G. B.Luciani, andC.Vergara,
“Helical flows and asymmetry of blood jet in dilated ascending aorta with
normally functioning bicuspid valve,” *Biomech. Model. Mechanobiol.*, vol. 12, no.
4, pp. 801–813, Aug.2013.
- [15] A. C.Braverman, H.Güven, M. A.Beardslee, M.Makan, A. M.Kates, andM.
R.Moon, “The Bicuspid Aortic Valve,” *Curr. Probl. Cardiol.*, vol. 30, no. 9, pp.
470–522, Sep.2005.
- [16] K. L.Losenno, R. L.Goodman, andM. W. A.Chu, “Bicuspid Aortic Valve Disease
and Ascending Aortic Aneurysms: Gaps in Knowledge,” *Cardiol. Res. Pract.*, vol.
2012, pp. 1–16, Oct.2012.
- [17] N.Tzemos, J.Therrien, J.Yip, G.Thanassoulis, S.Tremblay, M. T.Jamorski, G.
D.Webb, andS. C.Siu, “Outcomes in Adults With Bicuspid Aortic Valves,” *JAMA*,
vol. 300, no. 11, p. 1317, Sep.2008.
- [18] B. C. et al.DellaCorte A, Quarto C, “Spatiotemporal Patterns of Smooth Muscle
Cell Changes in Ascending Aortic Dilatation with Bicuspid and Tricuspid Aortic
Valve Stenosis.” 2008.
- [19] R. S.Beroukhim, T. L.Kruzick, A. L.Taylor, D.Gao, andA. T.Yetman,
“Progression of Aortic Dilation in Children With a Functionally Normal Bicuspid
Aortic Valve,” *Am. J. Cardiol.*, vol. 98, no. 6, pp. 828–830, Sep.2006.
- [20] S.Nistri, J.Grande-Allen, M.Noale, C.Basso, P.Siviero, S.Maggi, G.Crepaldi,
andG.Thiene, “Aortic elasticity and size in bicuspid aortic valve syndrome.”
- [21] S. K.Atkins, K.Cao, N. M.Rajamannan, andP.Sucosky, “Bicuspid aortic valve
hemodynamics induces abnormal medial remodeling in the convexity of porcine

- ascending aortas,” *Biomech. Model. Mechanobiol.*, vol. 13, no. 6, pp. 1209–1225, Nov.2014.
- [22] L.Cozijnsen, R. L.Braam, R. A.Waalewijn, M. A. A. M.Schepens, B. L.Loeyls, M. F. M.VanOosterhout, D. Q. C. M.Barge-Schaapveld, andB. J. M.Mulder, “What is new in dilatation of the ascending aorta?: Review of current literature and practical advice for the cardiologist,” *Circulation*, vol. 123, no. 8, pp. 924–928, 2011.
- [23] J. W.Kang, H. G.Song, D. H.Yang, S.Baek, D. H.Kim, J. M.Song, D. H.Kang, T. H.Lim, andJ. K.Song, “Association between bicuspid aortic valve phenotype and patterns of valvular dysfunction and bicuspid aortopathy: Comprehensive evaluation using MDCT and echocardiography,” *JACC Cardiovasc. Imaging*, vol. 6, no. 2, pp. 150–161, 2013.
- [24] A.DellaCorte, C.Bancone, M.Buonocore, G.Dialetto, F. E.Covino, S.Manduca, G.Scognamiglio, V.D ’oria, andM.DeFeo, “Pattern of Ascending Aortic Dimensions Predicts the Growth Rate of the Aorta in Patients With Bicuspid Aortic Valve,” 2013.
- [25] B. A.Merritt, A.Turin, M.Markl, S. C.Malaisrie, P. M.McCarthy, andJ. C.Carr, “Association between leaflet fusion pattern and thoracic aorta morphology in patients with bicuspid aortic valve,” *J. Magn. Reson. Imaging*, vol. 40, no. 2, pp. 294–300, 2014.
- [26] D.Bonderman, E.Gharehbaghi-Schnell, G.Wollenek, G.Maurer, H.Baumgartner, I. M.Lang, T.Watanabe, M.Yamagishi, M.Kitakaze, S.Kitamura, andK.Miyatake, “Mechanisms underlying aortic dilatation in congenital aortic valve malformation,” *Circulation*, vol. 99, no. 16, pp. 2138–2143, Apr.1999.

- [27] M.Cotrufo, A.DellaCorte, L. S.DeSanto, C.Quarto, M.DeFeo, G.Romano, C.Amarelli, M.Scardone, F.DiMeglio, G.Guerra, M.Scarano, S.Vitale, C.Castaldo, andS.Montagnani, “Different patterns of extracellular matrix protein expression in the convexity and the concavity of the dilated aorta with bicuspid aortic valve: Preliminary results,” *J. Thorac. Cardiovasc. Surg.*, vol. 130, no. 2, pp. 504–511, 2005.
- [28] M.Nataatmadja, “Abnormal Extracellular Matrix Protein Transport Associated With Increased Apoptosis of Vascular Smooth Muscle Cells in Marfan Syndrome and Bicuspid Aortic Valve Thoracic Aortic Aneurysm,” *Circulation*, vol. 108, no. 90101, p. 329II--334, Sep.2003.
- [29] F.-X.Schmid, K.Bielenberg, A.Schneider, A.Haussler, A.Keyser, andD.Birnbaum, “Ascending aortic aneurysm associated with bicuspid and tricuspid aortic valve: involvement and clinical relevance of smooth muscle cell apoptosis and expression of cell death-initiating proteins.,” *Eur. J. Cardiothorac. Surg.*, vol. 23, no. 4, pp. 537–43, Apr.2003.
- [30] P. W. M.Fedak, S.Verma, T. E.David, R. L.Leask, R. D.Weisel, andJ.Butany, “Clinical and pathophysiological implications of a bicuspid aortic valve,” *Circulation*, vol. 106, no. 8, pp. 900–904, 2002.
- [31] J. J.Doyle, E. E.Gerber, andH. C.Dietz, “Matrix-dependent perturbation of TGF?? signaling and disease,” *FEBS Lett.*, vol. 586, no. 14, pp. 2003–2015, 2012.
- [32] J. S.Ikonomidis, J. A.Jones, J. R.Barbour, R. E.Stroud, L. L.Clark, B. S.Kaplan, A.Zeeshan, J. E.Bavaria, J. H.Gorman, F. G.Spinal, andR. C.Gorman, “Expression of matrix metalloproteinases and endogenous inhibitors within

- ascending aortic aneurysms of patients with bicuspid or tricuspid aortic valves,” *J. Thorac. Cardiovasc. Surg.*, vol. 133, no. 4, pp. 1028–1036, Apr.2007.
- [33] D.Litmanovich, A. A.Bankier, L.Cantin, V.Raptopoulos, andP. M.Boiselle, “CT and MRI in diseases of the aorta,” *Am. J. Roentgenol.*, vol. 193, no. 4, pp. 928–940, 2009.
- [34] E.Wilton andM.Jahangiri, “Post-stenotic aortic dilatation.”
- [35] S.Perrotta andS.Lentini, “Alternative Surgical Management of Ascending Aorta Aneurysm,” 1997.
- [36] F.Robicsek, J. W.Cook, M. K.Reames, andE. R.Skipper, “Size reduction ascending aortoplasty: Is it dead or alive?”
- [37] A. J.Barker, M.Markl, J.Bürk, R.Lorenz, J.Bock, S.Bauer, J.Schulz-Menger, andF.VonKnobelsdorff-Brenkenhoff, “Bicuspid aortic valve is associated with altered wall shear stress in the ascending aorta,” *Circ. Cardiovasc. Imaging*, vol. 5, no. 4, pp. 457–466, 2012.
- [38] R.Mahadevia, A. J.Barker, S.Schnell, P.Entezari, P.Kansal, P. W. M.Fedak, S. C.Malaisrie, P.McCarthy, J.Collins, J.Carr, andM.Markl, “Bicuspid aortic cusp fusion morphology alters aortic three-dimensional outflow patterns, wall shear stress, and expression of aortopathy,” *Circulation*, vol. 129, no. 6, pp. 673–682, 2014.
- [39] M. M.Bissell, A. T.Hess, L.Biasioli, S. J.Glaze, M.Loudon, A.Pitcher, A.Davis, B.Prendergast, M.Markl, A. J.Barker, S.Neubauer, andG.Saul, “Aortic Dilation in Bicuspid Aortic Valve Disease : Flow Pattern Is a Major Contributor and Differs with Valve Fusion Type World Wide Web at : Aortic Dilation in Bicuspid Aortic

Valve Disease : Flow Pattern Is a Major Contributor and Differs with Valve Fus,” 2013.

- [40] M. D.Hope, T. A.Hope, A. K.Meadows, K. G.Ordovas, T. H.Urbania, M. T.Alley, andC. B.Higgins, “Bicuspid Aortic Valve : Four-dimensional MR Evaluation of Ascending Aortic Systolic Methods : Results :,” *Radiology*, vol. 255, no. 1, pp. 53–61, 2010.
- [41] M. D.Hope, T. A.Hope, S. E. S.Crook, K. G.Ordovas, T. H.Urbania, M. T.Alley, andC. B.Higgins, “4D flow CMR in assessment of valve-related ascending aortic disease,” *JACC Cardiovasc. Imaging*, vol. 4, no. 7, pp. 781–787, 2011.
- [42] A.McNally, A.Madan, andP.Sucosky, “Morphotype-Dependent Flow Characteristics in Bicuspid Aortic Valve Ascending Aortas: A Benchtop Particle Image Velocimetry Study,” *Front. Physiol.*, vol. 8, p. 44, Feb.2017.
- [43] K.Cao, S. K.Atkins, A.Mcnally, J.Liu, andP.Sucosky, “Simulations of morphotype-dependent hemodynamics in non-dilated bicuspid aortic valve aortas,” *J. Biomech.*, vol. 50, pp. 63–70, 2016.
- [44] N.Kimura, M.Nakamura, K.Komiya, S.Nishi, A.Yamaguchi, O.Tanaka, Y.Misawa, H.Adachi, andK.Kawahito, “Patient-specific assessment of hemodynamics by computational fluid dynamics in patients with bicuspid aortopathy,” *J. Thorac. Cardiovasc. Surg.*, vol. 153, no. 4, p. S52–S62.e3, 2017.
- [45] N.Saikrishnan, L.Mirabella, andA. P.Yoganathan, “Bicuspid aortic valves are associated with increased wall and turbulence shear stress levels compared to trileaflet aortic valves,” *Biomech. Model. Mechanobiol.*, vol. 14, no. 3, pp. 577–588, 2015.

- [46] S.Numata, K.Itatani, K.Kanda, K.Doi, S.Yamazaki, K.Morimoto, K.Manabe, K.Ikemoto, and H.Yaku, “Blood flow analysis of the aortic arch using computational fluid dynamics,” *Eur. J. Cardio-thoracic Surg.*, vol. 49, no. 6, pp. 1578–1585, 2016.
- [47] P. D.Morris, A.Narracott, H.VonTengg-Kobligk, D.Alejandro, S.Soto, S.Hsiao, A.Lungu, P.Evans, N. W.Bressloff, P.VLawford, D. R.Hose, and J. P.Gunn, “Computational fluid dynamics modelling in cardiovascular medicine,” 2016.
- [48] T.Yamaguchi, “Computational Visualization of Blood Flow,” in *Computational Biomechanics*, Tokyo: Springer Japan, 1996, pp. 165–184.
- [49] P. M.DenReijer, D.Sallee, P.Van DerVelden, E.Zaaijer, W. J.Parks, S.Ramamurthy, T.Robbie, G.Donati, C.Lamphier, R.Beekman, and M.Brummer, “Hemodynamic predictors of aortic dilatation in bicuspid aortic valve by velocity-encoded cardiovascular magnetic resonance,” *J. Cardiovasc. Magn. Reson.*, vol. 12, no. 1, pp. 1–13, 2010.
- [50] S. K.Atkins and P.Sucosky, “Etiology of bicuspid aortic valve disease: Focus on hemodynamics,” *World J. Cardiol.*, vol. 6, no. 12, p. 1227, 2014.
- [51] D.Bonomi, C.Vergara, E.Faggiano, M.Stevanella, C.Conti, A.Redaeli, G.Puppini, G.Faggian, L.Formaggia, and G. B.Luciani, “Influence of the aortic valve leaflets on the fluid-dynamics in aorta in presence of a normally functioning bicuspid valve,” *Biomech. Model. Mechanobiol.*, vol. 14, no. 6, pp. 1349–1361, 2015.
- [52] P. W. M.Fedak, M. P. L.deSa, S.Verma, N.Nili, P.Kazemian, J.Butany, B. H.Strauss, R. D.Weisel, T. E.David, M. H.Yacoub, T. M.Sundt, F. W.Sellke, and C.Pizarro, “Vascular matrix remodeling in patients with bicuspid aortic valve

- malformations: Implications for aortic dilatation,” *J. Thorac. Cardiovasc. Surg.*, vol. 126, no. 3, pp. 797–806, Sep.2003.
- [53] J.Boyum, E. K.Fellinger, J. D.Schmoker, L.Trombley, K.McPartland, F. P.Ittleman, andA. B.Howard, “Matrix metalloproteinase activity in thoracic aortic aneurysms associated with bicuspid and tricuspid aortic valves,” *J. Thorac. Cardiovasc. Surg.*, vol. 127, no. 3, pp. 686–691, 2004.
- [54] A.DellaCorte, C.Quarto, C.Bancone, C.Castaldo, F.DiMeglio, D.Nurzynska, L. S.DeSanto, M.DeFeo, M.Scardone, S.Montagnani, andM.Cotrufo, “Spatiotemporal patterns of smooth muscle cell changes in ascending aortic dilatation with bicuspid and tricuspid aortic valve stenosis: Focus on cell-matrix signaling,” *J. Thorac. Cardiovasc. Surg.*, vol. 135, no. 1, pp. 1–4, Jan.2008.
- [55] S. K.Atkins, A.Moore, andP.Sucosky, “Bicuspid aortic valve hemodynamics does not promote remodeling in porcine aortic wall concavity,” *World J. Cardiol.*, vol. 8, no. 1, p. 89, 2016.
- [56] M.Bauer, M.Pasic, R.Schaffarzyk, H.Siniawski, F.Knollmann, R.Meyer, andR.Hetzer, “Reduction aortoplasty for dilatation of the ascending aorta in patients with bicuspid aortic valve,” *Ann. Thorac. Surg.*, vol. 73, no. 3, pp. 720–723, 2002.
- [57] P.Sucosky, M.Padala, A.Elhammali, K.Balachandran, H.Jo, andA. P.Yoganathan, “Design of an ex vivo culture system to investigate the effects of shear stress on cardiovascular tissue,” *J Biomech Eng*, vol. 130, no. 3, p. 35001, 2008.
- [58] M. J.Levesque andR. M.Nerem, “The Elongation and Orientation of Cultured Endothelial Cells in Response to Shear Stress,” *J. Biomech. Eng.*, vol. 107, no. 4,

p. 341, Nov.1985.

- [59] L.Sun, N. M.Rajamannan, andP.Sucosky, “Design and validation of a novel bioreactor to subject aortic valve leaflets to side-specific shear stress.,” *Ann. Biomed. Eng.*, vol. 39, no. 8, pp. 2174–85, Aug.2011.
- [60] P.Sucosky, M.Padala, A.Elhammali, K.Balachandran, H.Jo, andA. P.Yoganathan, “Design of an Ex Vivo Culture System to Investigate the Effects of Shear Stress on Cardiovascular Tissue,” *J. Biomech. Eng.*, vol. 130, no. 3, p. 35001, Jun.2008.
- [61] X.Zhang, D. J.Huk, Q.Wang, J.Lincoln, andY.Zhao, “A microfluidic shear device that accommodates parallel high and low stress zones within the same culturing chamber.”
- [62] W. O.Lane, A. E.Jantzen, T. A.Carlon, R. M.Jamiolkowski, J. E.Grenet, M. M.Ley, J. M.Haseltine, L. J.Galinat, F.-H.Lin, J. D.Allen, G. A.Truskey, andH. E.Achneck, “Parallel-plate Flow Chamber and Continuous Flow Circuit to Evaluate Endothelial Progenitor Cells under Laminar Flow Shear Stress,” *J. Vis. Exp*, vol. 3349379133, no. 10, 2012.
- [63] K.Cao andP.Sucosky, “Effect of Bicuspid Aortic Valve Cusp Fusion on Aorta Wall Shear Stress: Preliminary Computational Assessment and Implication for Aortic Dilation,” *World J. Cardiovasc. Dis.*, vol. 5, no. 6, pp. 129–140, 2015.
- [64] H. H.-H. H.Sievers andC.Schmidtke, “A classification system for the bicuspid aortic valve from 304 surgical specimens,” *J. Thorac. Cardiovasc. Surg.*, vol. 133, no. 5, pp. 1226–1233, May2007.
- [65] K.Cao, M.BukaČ, andP.Sucosky, “Three-dimensional macro-scale assessment of regional and temporal wall shear stress characteristics on aortic valve leaflets,”

Comput. Methods Biomech. Biomed. Engin., vol. 19, no. 6, 2016.

- [66] L.Mirabella, A. J.Barker, N.Saikrishnan, E. R.Coco, D. J.Mangiameli, M.Markl, andA. P.Yoganathan, “MRI-based Protocol to Characterize the Relationship Between Bicuspid Aortic Valve Morphology and Hemodynamics.,” *Ann. Biomed. Eng.*, vol. 43, no. 8, pp. 1815–27, Aug.2015.
- [67] A. J.Barker, C.Lanning, andR.Shandas, “Quantification of hemodynamic wall shear stress in patients with bicuspid aortic valve using phase-contrast MRI,” *Ann. Biomed. Eng.*, vol. 38, no. 3, pp. 788–800, Mar.2010.
- [68] X.He andD. N.Ku, “Pulsatile Flow in the Human Left Coronary Artery Bifurcation : Average Conditions,” *J. Biomech. Eng.*, vol. 118, no. February 1996, pp. 74–82, 1996.
- [69] K.Cornelius, M.Graham, T.Leonard, andA.Yorde, “Wright State University-Capstone: Design of a Novel Fluid Shear Stress Bioreactor for Cardiovascular Tissue.”
- [70] A. J.Barker, M.Markl, J.Bürk, R.Lorenz, J.Bock, S.Bauer, J.Schulz-menger, andF.VonKnobelsdorff-brenkenhoff, “Bicuspid Aortic Valve Is Associated With Altered Wall Shear Stress in the Ascending Aorta,” 2012.
- [71] M. M.Bissell, A. T.Hess, L.Biasioli, S. J.Glaze, M.Loudon, A.Pitcher, A.Davis, B.Prendergast, M.Markl, andH.Way, “Aortic Dilation in Bicuspid Aortic Valve Disease : Flow Pattern Is a Major Contributor and Differs with Valve Fusion Type,” 2013.
- [72] I.Pelech andA. H.Shapiro, “Flexible Disk Rotating on a Gas Film Next to a Wall,” *J. Appl. Mech.*, vol. 31, no. 4, p. 577, Dec.1964.

- [73] H. P.Sdougos, S. R.Bussolari, andC. F.Dewey, “Secondary flow and turbulence in a cone-and-plate device,” *J. Fluid Mech*, vol. 7102, no. 138, pp. 37–404, 1984.
- [74] V.Peiffer, S. J.Sherwin, andP. D.Weinberg, “Computation in the rabbit aorta of a new metric - the transverse wall shear stress - to quantify the multidirectional character of disturbed blood flow,” *J. Biomech.*, vol. 46, no. 15, pp. 2651–2658, 2013.
- [75] C.Meierhofer, E. P.Schneider, C.Lyko, A.Hutter, S.Martinoff, M.Markl, A.Hager, J.Hess, H.Stern, andS.Fratz, “Wall shear stress and flow patterns in the ascending aorta in patients with bicuspid aortic valves differ significantly from tricuspid aortic valves: a prospective study.,” *Eur. Heart J. Cardiovasc. Imaging*, vol. 14, no. 8, pp. 797–804, 2013.